

UCSF

UC San Francisco Electronic Theses and Dissertations

Title

Human Endplate Permeability and Microstructure and Their Relationship to Disc Degeneration

Permalink

<https://escholarship.org/uc/item/7tt8x6dr>

Author

Rodriguez, Azucena Guadalupe

Publication Date

2010

Peer reviewed|Thesis/dissertation

Human Endplate Permeability and Microstructure, and Their
Relationship to Disc Degeneration

by

Azucena Guadalupe Rodriguez

DISSERTATION



Copyright 2010

by

Azucena Guadalupe Rodriguez

Dedicated to my parents,
Miguel and Amparo Rodriguez
and
In memory of Mr. Kevin Pendergast.

Acknowledgements

“It takes a village” is a classic idiom, but in my case also a very true statement, it literally “took the village” of Berkeley, UCSF faculty, family and friends to help me finish my dissertation and make this finished product possible. I want to take this opportunity to thank all of the people in my life who helped me to push through and finish.

I want to give a special thanks to my research advisor, Jeffrey Lotz for his guidance, support and encouragement in completing this project. I would also like to thank my qualifying exam committee David Rempel, David Saloner, Harriet Hopf and Karen King, for their time, insight and guidance. To my academic advisor Sarah Nelson for her time and great help preparing me for my qualifying exam. To my dissertation committee members, Sharmila Majumdar and Sig Berven for providing expertise and valuable feedback during the final phase of this dissertation.

I want to thank all past and present members of the Lotz lab for their technical support, particularly to Kirk Pedersen, Tamer Hadi, Jane Liu, Zheng Xu, Chloe Slichter, Johnny Eguizabal and Frank Acosta. To Kevin Cheng, Anne Kim, Sean Degmetich, Paige Ryan, Dezba Coughlin, David Moody, Cory Laws, David Lari, for providing a great work environment. To Betty Cheung, Mary Ellen Kirkchaney, Dulce Paradero and Eunice Chang, for helping with lab orders and sharing recipes. A special thanks to David Schultz for his continuous technical advice and friendship. To Ellen Liebenberg, for her endless guidance during our communal lunches. To Jill Ulrich McCoy, for providing advice and company during our after-work dinners and help during my qualifying exam preparation. To Jeannie Bailey, for her enthusiasm, her lively spirit and helping me

through the final push of this process. To Zori Buser, for being a great post-doc role model and always being ready to lend a hand. To Melodie Metzger, for her support and help during the manuscript preparation. To Carolyn Sparrey for sharing her technical knowledge, for her help and encouragement.

In addition, to the members of the Majumdar lab, Andrew Burghardt, Ana Rodriguez-Soto, Julio Carballido-Gamio, Galateia Kazakia, Bryan Hermansson, Miki Sode, Roland Krug, Gabby Blumenkratz Joseph, Jin Zuo, who provided me with technical support, advice and friendship.

I would like to thank my peer mentor Jenni Buckley for her valuable time and help during my qualifying exam preparation and early dissertation preparation, for sharing her enthusiasm for mentoring and helping others.

I want to give a special thanks to my mentor, friend and guide Elisa Bass, for her patience, continuous support, and guidance, her valuable time reading and editing multiple drafts and believing that I could write this dissertation. This would not have been possible without you Elisa!

I am very lucky to have great supportive friends. Thanks to Marisela Avalos Morales, Lucina Rodriguez, Teresa Hernandez and Carlos Zavala-Jurado, who have shown me their love and support throughout these years with valuable conversations and nourishing food. Thanks to Jessica Preciado, Lola Odusanya, Arel Cordero and Jason Bowen for providing practical information about this arduous process. Thanks to Fernando Rayas Frutos for providing healthy distractions by joining me through many runs in the park.

Thanks to the members of the supporting student groups, BEASTs, Latino Association of Graduate Students in Engineering (LAGSES) at Berkeley and the Minority Graduate Student Association (MGSO) at UCSF. To Carla Trujillo for her great advice that carried me through to the end of my graduate studies. To my roommates at 1462, especially Bryan Alkemeyer, Grant Johnson, Nina Menconi and Margaret Clark, for providing a supportive atmosphere and making our living space feel like a home. To Jacqueline Kazarian, for sharing her valuable wisdom obtained after 8 decades of life.

Finally, I want to thank my parents, Miguel and Amparo and my brother Luis. I could not have completed this without your love, patience and encouragement. ¡Muchas gracias, los quiero mucho!

Abstract

Human Endplate Permeability and Microstructure and Their Relationship to Disc Degeneration

By

Azucena Guadalupe Rodriguez

Doctor of Philosophy in Bioengineering

University of California, San Francisco and Berkeley

Professor Jeffrey C. Lotz, Chair

Low back pain may be caused by disc degeneration and is a prevalent problem in the United States affecting thirty-one million Americans at any given time. While the etiology is unknown, it has been hypothesized that poor disc nutrition triggered by sclerosis in the vertebral endplate and/or calcification of the cartilaginous endplate is a leading factor in disc degeneration. The objective of this study was to better understand these phenomena by measuring endplate permeability and vertebral endplate bone microstructure and correlating these parameters with disc degeneration parameters.

Intervertebral cores including the subchondral bone, cartilage endplate and adjacent nucleus were harvested from human cadaveric lumbar spines and used for permeability and morphology assessments. The endplate permeability was measured using a custom made, validated permeameter device and the morphology of the vertebra was analyzed using a MicroCT device. The individual relationships between endplate permeability, vertebral endplate morphological changes and disc degeneration parameters were analyzed.

Contrary to previous findings, bone permeability was observed to increase with disc degeneration. Vertebral endplate porosity increased and trabecular thickness decreased as the bony endplate became more homogeneous with disc degeneration. Cartilage permeability was not correlated with disc degeneration, but cell density increased, GAGs decreased and GAGs/cell decreased with degeneration.

The correlation between bone permeability, porosity and degeneration suggest that sclerosis at the vertebral endplate was not present. These results in combination with those found for cartilage permeability, cell density and GAGs in the disc imply that cell dysfunction and a decrease of nutrient availability through the capillaries, rather than physical barriers to transport, accelerate disc disease.

Table of Contents

List of Figures.....	xiii
List of Tables.....	xx
Chapter 1 Introduction.....	1
1.1 Motivation.....	1
1.1 Structure and function of the IVD	1
1.2 Structure and function of the vertebrae	4
1.3 Nutrition of the lumbar IVD.....	6
1.4 Physical changes in the CEP and VEP.....	9
1.5 Aging of the disc and disc degeneration.....	10
1.6 Disc degeneration classification	11
1.7 Permeability studies.....	11
1.8 Imaging of vertebral endplate.....	13
1.9 Objectives.....	14
Chapter 2 Permeameter Design and Validation	16
2.1 Introduction.....	16
2.2 Permeameter Design.....	17
Requirements for the Permeameter Design	17
Permeameter-Generation 1 Components and Function	18
Additional Requirements for Permeameter	21

Permeameter-Generation 2 Components and Function	22
Permeability Calculations	26
Validation Guidelines	26
2.3 Validation Methods.....	27
Leakage Test	27
Selection of Standard Specimen	27
Repeatability Study.....	28
Upper and Lower Limits of Permeability Range.....	29
Statistical Analysis.....	29
2.4 Results	30
2.5 Discussion.....	32
Chapter 3 Human Disc Nucleus Properties and Vertebral Endplate Permeability .	36
3.1 Introduction.....	36
3.2 Materials and Methods.....	37
Dissection.....	37
Imaging	39
Permeability testing	40
Biochemistry	44
Data Analysis	45
Permeability, Porosity and Cartilage Thickness.....	46
Cell Density, GAGs and GAGs/cell	46
Degeneration.....	46

3.3 Results	46
Endplate Permeability, Porosity & Cartilage Thickness.....	47
Cell density	51
GAGs	53
GAGs/cell	56
Degeneration.....	58
3.4 Discussion.....	59
Chapter 4 Morphology of the vertebral endplate	67
4.1 Introduction.....	67
4.2 Materials and Methods.....	69
Imaging	70
4.3 Results	75
Porosity variation with degeneration (Figure 4.6A, Figure 4.7).....	76
Trabecular thickness variation with degeneration (Figure 4.6B, Figure 4.8).....	76
Pore diameter variation with degeneration (Figure 4.6C, Figure 4.9).....	77
Pore number variation with degeneration (Figure 4.6D, Figure 4.10).....	77
Structural bone indices variation with age, GAGs and cell density (Table 4.2).....	81
Permeability	82
Additional Observations	83
4.4 Discussion.....	85
Chapter 5 Conclusions and Future Directions.....	91
5.1 Research Summary	91

5.2 Future Directions	93
References.....	97

List of Figures

Figure 1.1 (Left) Diagram of the spine. (Middle bottom) Diagram magnification of the intervertebral disc and the adjacent vertebrae at the lumbar region. Each intervertebral disc is positioned between two vertebrae. (Middle top) Diagram of extracellular matrix including chondrocytes, GAGs, link proteins and collagen components. Image adapted from Aigner et al 2007[15]. (Right) A schematic representation of the normal histology of annulus, nucleus, disc, CEP, VEP and Blood Vessels (BV). Image adapted from Roberts et al 1989[13]	3
Figure 1.2 (Top) Top view of lumbar vertebra (Bottom) Sagittal section of lumbar vertebra. The vertebral foramen contains the spinal cord. (Image adapted from DeLisa et. al. 1981)[23].	5
Figure 1.3 Illustration of the vascular supply to the disc space from the cartilaginous endplate (1) lumbar arteries enter through the vertebral foramen, (2) vertebral artery, (3) capillary bed and (4) annulus. (Image adapted from Martin et .al. 2002) [31]	7
Figure 1.4 Pfirrmann classification of disc degeneration [55].....	11
Figure 1.5 A one-dimensional flow of liquid through a porous material. Q is volumetric flow (m^3/s), A is the cross sectional area (m^2), ΔP is the change in pressure and L is the length of the specimen.	13
Figure 2.1 Schematic of device for endplate permeability measurement generation 1 [56].	20
Figure 2.2 Permeameter connected to MTS machine	21
Figure 2.3 Illustration of the second-generation permeameter	23
Figure 2.4 Second-generation permeameter used for studies.	24

Figure 2.5 Fluid collection system for permeameter (top). Specimen holder close up (bottom).....	25
Figure 2.6 Permeability range for cartilage and bone and the validation range for the device.....	29
Figure 2.7 Comparison of the measured permeability with the manufacturer permeability. A linear fit was applied. The correlation has an $R^2 = 0.95$	30
Figure 2.8 Repeatability of the permeameter for each of the 5 different pore size discs. Each disc type was tested 6 times and the variability is shown in the graph.....	31
Figure 3.1 Schematic of endplate specimen harvest. Specimen was cored from the frozen motion segment (8.25 mm diameter). The cartilage endplate attached to the vertebral cores was separated from the nucleus pulposus tissue for MicroCT (μ CT) and permeability measurements. The nuclear tissue was separated in three parts, which were labeled in reference to the adjacent vertebra: inferior (1), center (2), superior (3) for biochemical measurements.....	39
Figure 3.2 A MicroCT transverse view of a subchondral endplate is shown on the left (A). The open pores are filled using a method that highlights the size of the pores by using a color scale right (B).....	40
Figure 3.3 Illustration of the permeameter. The custom-made permeameter is composed of stainless steel pipes connected to a water reservoir. These pipes are also connected to a pressure transducer, a safety pressure release valve, fluid outlets, a filter and a specimen connector. The fluid is pressurized to 1 MPa and pressed through the cartilage-bone specimen. A schematic of the test specimen is shown on the top left corner where P_u is the upstream pressure, P_{d1} is the pressure	

downstream of the cartilage endplate, and Pd2 is the pressure downstream of the subchondral bone.	41
Figure 3.4 Total hydraulic permeability (THP) had a positive correlation with age (THP (x 10 ⁻¹⁰) = 0.11*age - 3.80; R ² =0.16, p<0.01).	48
Figure 3.5 Total hydraulic permeability (THP) had a positive correlation with bone porosity (THP (x 10 ⁻¹⁰) = 16.13*bone porosity - 5.33; R ² =0.09, p=0.05).....	48
Figure 3.6 Bone permeability also had positive correlation with age (Bone Permeability (x 10 ⁻¹⁰) = 0.27*age + 4.89; R ² =0.10, p=0.03).	49
Figure 3.7 Bone permeability also had positive correlation with bone porosity (Bone Permeability (x 10 ⁻¹⁰) = 75.15*bone porosity -18.19; R ² =0.23, p<0.001).....	49
Figure 3.8 The variation of Bone permeability with GAG content. Data fitted with a power equation, (Bone Permeability = 44.18*GAG content ^{-0.6} ; R ² =0.14, p=0.02)..	50
Figure 3.9 The variation of subchondral bone porosity with age (R ² =0.13, p=0.004).	50
Figure 3.10 The variation of subchondral bone porosity with degeneration (R ² =0.19, p=0.04). (Significance using post-hoc Tukey test, *p<0.05).....	51
Figure 3.11 The variation of cell density (cells/mm ³) with Pfirrmann degeneration grade is presented. Results are shown for mean and standard deviations. (Significance using post-hoc Tukey test, *p<0.05).....	53
Figure 3.12 The variation of GAG content with age. Data fitted with a power fit equation GAG =296257*age ^{-2.58} (R ² = 0.57, p<0.0001).	54
Figure 3.13 The distribution of GAG content with degeneration is shown (R ² =0.52, p<0.0001). (Significance using post-hoc Tukey test, *p<0.05).....	54

Figure 3.14 Endplate porosity decreased as GAG content increased ($R^2=0.20$, $p<0.002$).
..... 55

Figure 3.15 The variation of GAG content with disc height. Data fitted with power fit equation $GAG = 0.12 * \text{disc height}^{1.81}$ ($R^2 = 0.20$, $p<0.001$)..... 55

Figure 3.16 The variation of cell function (GAGs/cell) was compared to Pfirrmann degeneration grading ($R^2=0.24$; $p<0.001$). Results are shown for mean and standard deviations. (Significance using post-hoc Tukey test, $*p<0.05$)..... 56

Figure 3.17 GAGs/cell were compared to disc height where $GAGs/cell=1 \times 10^{-5} * \text{disc height}^{2.70}$ ($R^2=0.29$, $p<0.01$) 57

Figure 3.18 The GAGs/cell had a power fit variation with age. $GAGs/cell = 25.87 * \text{age}^{-2.01}$ ($R^2=0.23$, $p<0.01$). 57

Figure 3.19 Pfirrmann grade increased with age ($R^2=0.31$, $p=0.002$), with grades 1, 3 & 4 being statistically different (Significance using post-hoc Tukey test, $*p<0.05$) 58

Figure 3.20 The distribution of disc height with degeneration is shown ($R^2=0.57$, $p<0.0001$) 59

Figure 3.21 The variation of cell density (cells/mm^3) with disc height (mm). Data fitted with a non-linear fit equation of the relationship between the two parameters cell density (CD) and disc height (h); $CD = 16324 \times h^{-1.02}$ ($R^2 = 0.15$, $p = 0.005$). 62

Figure 4.1 Diagram of a motion segment, comprised of an inferior vertebra, an adjacent disc and a superior vertebra. The endplate structure is composed of the vertebral endplate and the cartilaginous endplate. Capillaries are located in the center of the vertebra and on the periphery. Nutrients travel from the capillaries through the endplate structure to the nucleus pulposus..... 68

Figure 4.2 Diagram of a motion segment dissection. Each motion segment core was composed of the inferior vertebral endplate cranial to the disc, the intervertebral nuclear tissue and the superior vertebral endplate caudal to the disc. 69

Figure 4.3 (A) MicroCT sagittal view of VEP thickness region on one slice. 2D view from top for (B) Porosity – The gray color highlights the bone and blue background highlights the open pores (C) Trabecular thickness – The red areas highlight the thickest trabeculae. (D) Pore Diameter – The red areas highlight the largest pores. 72

Figure 4.4 A. (From left to right). The diagram shows the cylindrical core obtained from the vertebral motion segment. It is followed by a 3D MicroCT image of the two individual vertebral cores highlighting the location of the 2 mm regions. From the surface, a 2 mm thick region was selected. B. A sagittal binarized image of a subchondral bone section with a 2 mm ROI was selected (bottom left). A plot of the bone volume fraction (BV/TV) variation through the 2 mm depth is shown on the right. The location of the four ROIs analyzed was matched visually with the sagittal image on the left (bottom right). 73

Figure 4.5 MicroCT binarized sagittal sections from two specimens. The left column shows ROIs for a vertebral core next to a healthy disc and the right shows a vertebral core next to degenerated disc. A & E highlight the ‘surface’ region; B & F highlight the ‘most dense’ region. C & G highlight the ‘VEP thickness’ region and D & H highlight the ‘2 mm’ region. 74

Figure 4.6 ANOVAs comparing changes in each bone index with the four regions within each degeneration grade. Porosity (A), trabecular thickness (B), Pore diameter (C) and Pore number (D). * = statistically significant difference ($p < 0.05$) 78

Figure 4.7 Porosity variations with degeneration over the four regions. * = statistically significant difference (p<0.05).....	79
Figure 4.8 Trabecular thickness variations with degeneration over the 4 regions. * = statistically significant difference (p<0.05).	79
Figure 4.9 Pore diameter variations with degeneration over the 4 regions. * = statistically significant difference (p<0.05).....	80
Figure 4.10 Pore number variations with degeneration over the 4 regions. * = statistically significant difference (p<0.05).....	80
Figure 4.11 The results for the VEP thickness with degeneration for the complete dataset including the double layer samples are shown. No statistical significance was observed in vertebral thickness with degeneration grades.....	84
Figure 4.12 Sagittal slices of two samples that showed a double layer vertebral endplate (left). The matching bone fraction distribution per depth is presented (right). On the top left, level L4 superior vertebral endplate is shown and on the bottom left, level L2 superior vertebral endplate is shown. Each sample's distribution of bone fraction vs. depth plot is shown on the right. The double layer endplate can be seen in the plots on the right as showing two separate peaks.	84
Figure 4.13 Degeneration changes from two representative vertebral cores: (A) adjacent to a healthy disc and (B) adjacent to a degenerative disc, are illustrated showing a bone fraction variation in 2 mm depth. As the disc adjacent to a vertebral endplate became more degenerated (sample B). The most dense peak moved closer to the surface and the bone fraction decreased with degeneration. The quantity of	

trabeculae below the transitional zone (most dense peak) also decreased as the disc became more degenerated..... 88

List of Tables

Table 2.1 Permeability values obtained for repeatability and accuracy. Permeability (k/μ) presented for manufacturer's and measured values	31
Table 3.1 Means and standard deviations for outcome variables	52
Table 3.2 Correlation coefficients between variables.....	66
Table 4.1 The mean and standard deviations for each structural index in all four regions.	76
Table 4.2 Correlations of structural bone indices with age, GAGs and cell density for each of the four regions. * = statistically significant difference ($p < 0.05$). (↑) increasing trend, (↓) decreasing trend and (→) no relationship. The arrows indicate the trend that age, GAGs or cell density (dependent variables) follow with bone index (independent variable).....	81
Table 4.3 Correlations of structural bone indices with total permeability, bone permeability and cartilage permeability for each of the four regions. * = statistically significant difference ($p < 0.05$). (↑) increasing trend, (↓) decreasing trend and (→) no relationship. The arrows indicate the trend that total, bone or cartilage permeability (dependent variables) follows with bone index (independent variable).	82
Table 4.4 Double layer specimens-correlations of structural bone indices with age, cell density, GAG content, total permeability, bone permeability and cartilage permeability for each of the four regions. * = statistically significant difference ($p < 0.05$). (↑) increasing trend, (↓) decreasing trend and (→) no relationship. The arrow indicate the trend that age, GAGs, cell density total, bone or cartilage	

permeability (dependent variables) follow with bone index (independent variable).

..... 85

Chapter 1 Introduction

1.1 Motivation

Lower back pain is one of the most prominent diseases in industrialized countries [1] and cost the U.S. over \$85.9 billion for doctor visits in 2005 [2]. U.S. Statistics indicate that 80% of the population experience low back pain in their lives with 40% explained by disc degeneration [3]. Intervertebral disc (IVD) degeneration is a normal phenomenon in humans that is strongly associated with aging [4], but also can have pathologic origins identified by a premature loss of architectural, biological or biomechanical properties of the intervertebral disc [5] that can lead to chronic low back pain. Risk factors for premature degeneration are not fully understood, but include genetic and familial predisposition, mechanical exposures (i.e. occupational lifting or vibration)[6] and poor disc cell nutrition[7]. Since the disc is largely avascular, its cells rely primarily on diffusion for nutrient and waste transport [8]. Early research determined that the main location of diffusion is through the central endplate [7]. However, the relativity between IVD and endplate permeability is incompletely defined with disc degeneration. The motivation of this dissertation is to define important relationships between the cartilage endplate, vertebral endplate, and intervertebral disc health. We anticipate these relationships will shed light on principal disc degeneration mechanisms, and lead insight into approaches to disc regeneration.

1.1 Structure and function of the IVD

The intervertebral disc is the largest avascular tissue in the body making up one third of the spine length. It provides mobility to the spine framework by absorbing loads

and allowing bending and twisting motions between the vertebrae [9], while providing stability for protection of the neural elements.. The disc is composed of three structures, the nucleus pulposus, the annulus fibrosus and the cartilaginous endplate (Figure 1.1). The nucleus pulposus is a gelatinous mass comprised of proteoglycans (hydrophilic molecules), chondrocyte-like cells and type II collagen. In a healthy disc, the nucleus is 80% water and the annulus 65% water [10]. The annulus fibrosus is a highly organized structure containing up to 25 collagen layers oriented in alternating directions [11]. This organization allows the disc to withstand tensile and compressive forces when the body experiences twisting or bending. The collagen layers of the annulus are anchored to the vertebral body [12]. The cartilaginous endplates (CEP), composed of hyaline cartilage, are located at the superior and inferior ends of each vertebra where they also attach the disc to the vertebrae (Figure 1.1). The central region of the CEP covering the nucleus is thinner than that of the periphery, with a thickness ranging from 0.1 mm to 1.6 mm [13]. The CEP and the vertebral endplate (VEP) form the endplate structure (Figure 1.1). The endplate structure prevents the highly hydrated nucleus from bulging into the adjacent vertebrae when heavy loads are placed on the spine [14]. Together the VEP and the CEP form a boundary between the vertebra and the disc and regulate the nutrients diffusing into the disc to maintain the nuclear cells.

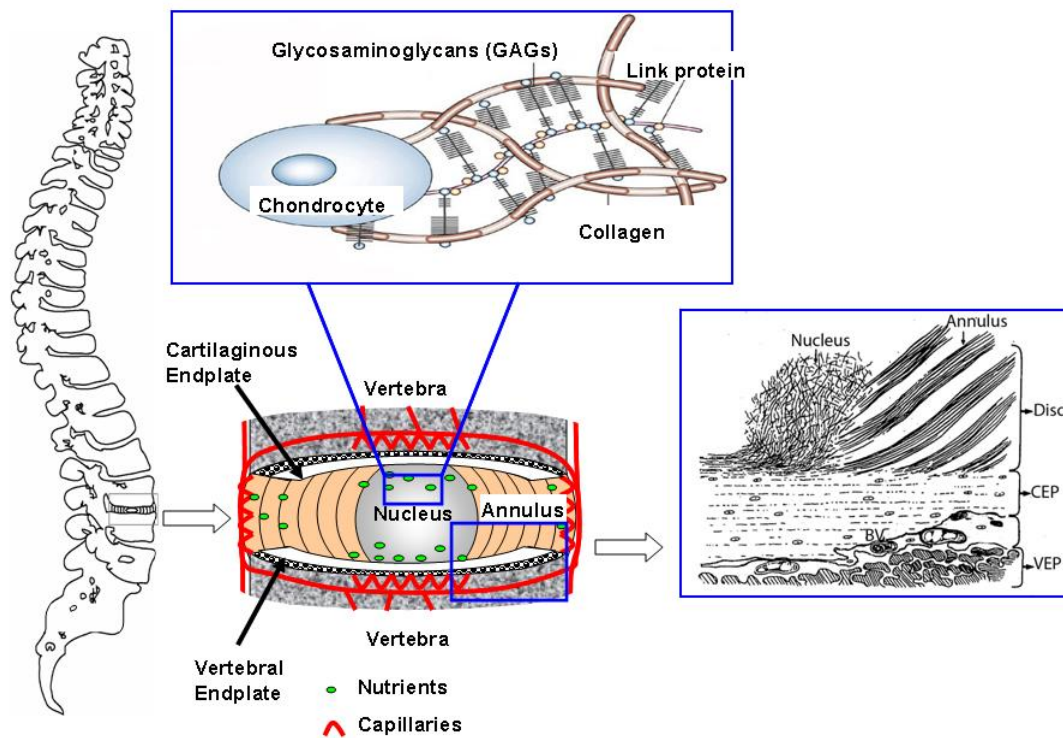


Figure 1.1 (Left) Diagram of the spine. (Middle bottom) Diagram magnification of the intervertebral disc and the adjacent vertebrae at the lumbar region. Each intervertebral disc is positioned between two vertebrae. (Middle top) Diagram of extracellular matrix including chondrocytes, GAGs, link proteins and collagen components. Image adapted from Aigner et al 2007[15]. (Right) A schematic representation of the normal histology of annulus, nucleus, disc, CEP, VEP and Blood Vessels (BV). Image adapted from Roberts et al 1989[13]

In the intervertebral disc, the nuclear cells maintain the extracellular matrix (ECM). A normal ECM imbibes water to allow for structured and functional integrity. Cells in the nucleus are mainly notochordal cells at a young age (<10 years old)[12]. With age, they are replaced with chondrocyte-like cells[16]. These nuclear cells synthesize and break down their own matrix[16]. They must thrive in this relatively avascular environment while responding to outside loads and synthesizing molecules for the ECM[9].

Proteoglycans, collagen and water make up 90-95% of the disc ECM (Figure 1.2). The extracellular matrix consists of the most abundant proteoglycan in the disc, aggrecan, which contains glycosaminoglycans (GAGs), which in turn are composed of keratan sulfate, chondroitin sulfate and repeating chains of disaccharides, attached to a core protein [9]. The composition of the GAGs changes with age and degeneration changes. These molecules are attached to a hyaluronan chain. The side chains of glycosaminoglycans attract water molecules to the negatively charged sulfated ends, creating swelling pressure in the disc [9], which is resisted by compressive forces [12]. This swelling pressure is resisted radially by the surrounding collagen of the annulus and axially by the vertebral endplates [9].

Collagen is the main structural protein in the disc [17]. The disc is composed of many types of collagen. Annulus is composed of the type I collagen and resistant to tension forces. The nucleus and the cartilage are mainly composed of type II collagen. Inter and intra fibril cross-links provide support to resist mechanical stresses and enzymatic degradation[9].

1.2 Structure and function of the vertebrae

The function of the vertebrae is to protect the spinal cord and neural elements, which are enclosed by the spinal canal, and to support the transmitted loads from the IVD [18] (Figure 1.2). Loads are shared between the trabecular and cortical bone[19]. Each vertebra is composed of the relatively dense cortical bone externally and the porous trabecular bone internally[20]. Cortical bone forms the vertebral outer shell and is composed of subchondral bone at the superior and inferior vertebral endplates[19] and the vertebral cortex on the remaining vertebra. In contrast to cortical bone, trabecular

bone is more porous and it forms the internal volume of the vertebra. Trabecular bone is described as "a porous honeycomb like network of trabecular plates and rods interspersed in the bone marrow compartment"[21]. These small interconnecting plates and rods, known as trabeculae, average 50 to 400 μm in thickness[21]. The minute structures evolve with age and disease from plates to rods, such that the ratio of plates to rods decreases, leading to an overall decrease in bone density with age [22].

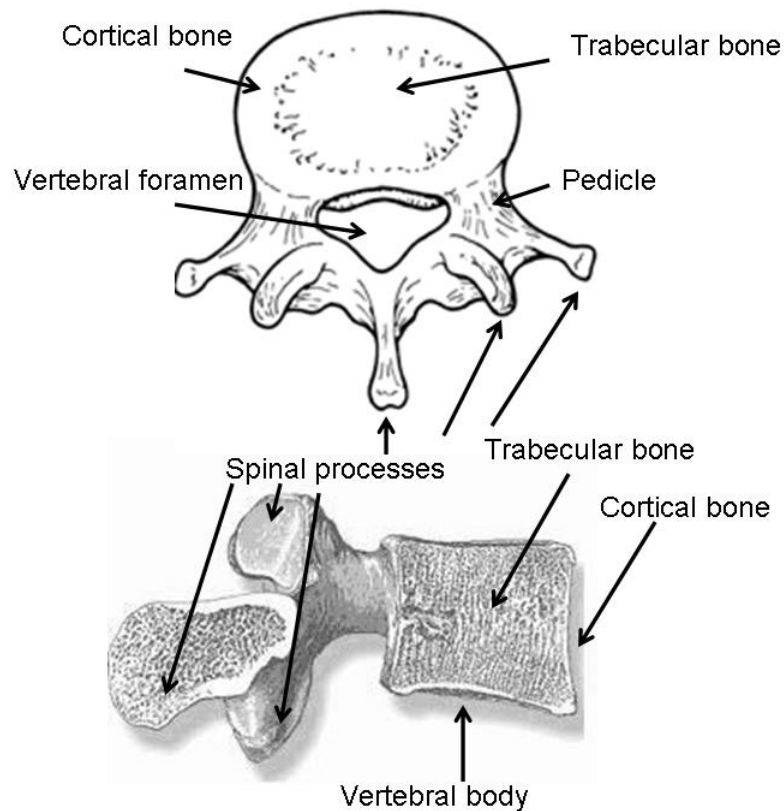


Figure 1.2 (Top) Top view of lumbar vertebra (Bottom) Sagittal section of lumbar vertebra. The vertebral foramen contains the spinal cord. (Image adapted from DeLisa et. al. 1981)[23].

The bone cells of cortical and trabecular bone are called osteocytes[21]. Osteons are the functional unit of compact bone, composed by a cylindrical layering of concentric

lamellar around a central Haversian canal, which provides the blood supply for the unit. Cortical bone is formed by osteons called Haversian systems. These systems are cylindrical in shape and are approximately 400 µm long and 200 µm wide at their base and are distributed evenly within the bone[21]. The porosity of cortical bone is an average of less than 5%, but this percentage can increase as cortical bone mass decreases[21]. Healthy adults normally experience thinning of the vertebral cortex and increasing cortical porosity as age increases [21].

The trabecular and cortical bone matrix structure is composed of the following materials, within these ranges: 50-70% mineral content (hydroxyapatite); 20-40% organic matrix; 5-10% water; and less than 3% lipids[21]. Mineral content is quantified by measuring , bone mineral density (BMD) , which provides information about the mechanical rigidity and load bearing strength of bone[21] . In addition, the organic matrix content provides information about bone elasticity and flexibility [21]. The mineral content known as bone mass accounts for 50-70% of bone strength.[21]

Bone remodeling is the process by which bone renews itself to maintain its strength and mineral homeostasis. Remodeling involves resorption and replacement of bone produced by the osteons[24]. A balance in the remodeling process indicates good bone health. An imbalance may lead to osteoporosis. According to Wolff's law, bone transforms itself in response to external stresses. Therefore the structure of the bone mass adapts to its functional requirements [25].

1.3 Nutrition of the lumbar IVD

The intervertebral disc receives its nutrition through both the annular disc periphery and the central one third cartilaginous endplate [26] [7]. In a healthy adult disc,

the outer annular disc cells obtain nutrients from blood vessels in the soft tissues around the annulus periphery [27]. Similarly, the blood supply for the central endplate location originates from the lumbar arteries and terminates at the capillaries which provide nutrients essential for cellular activity, viability and removal of metabolic waste[18]. The lumbar arteries enter the vertebral foramen, then, coil in the center and extend to the periphery [28, 29]. These arteries transform into capillaries and terminate just above the cartilaginous endplate within the vertebra and provide a continuous capillary bed across the bone disc interface [28](Figure 1.3). The capillaries are thus surrounded by vertebral trabeculae. The nutrients originating in the capillaries in the vertebra go through the endplate structure, enter the intervertebral disc and arrive at the nucleus pulposus where the nutrients are used by the disc cells, and metabolic products are removed from the disc [7, 30].

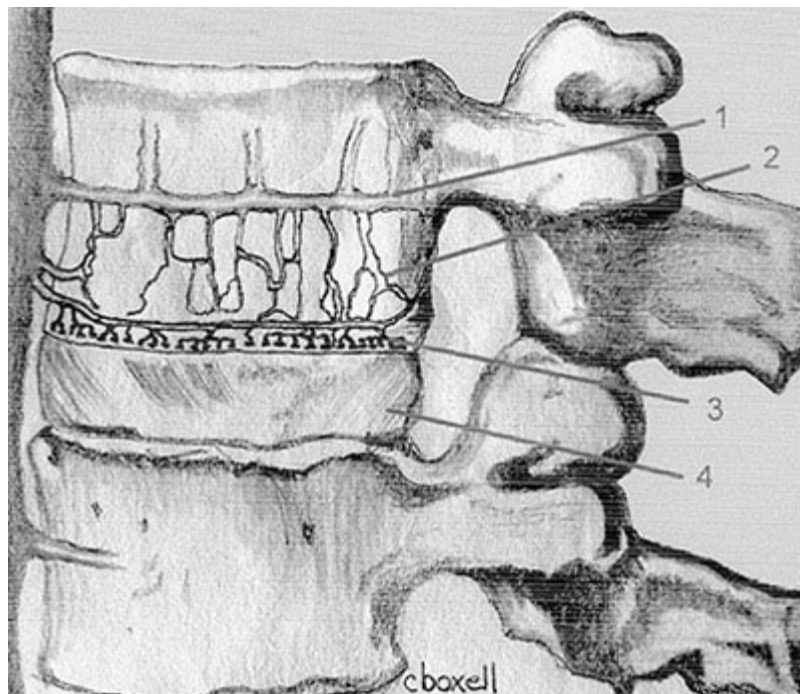


Figure 1.3 Illustration of the vascular supply to the disc space from the cartilaginous endplate (1) lumbar arteries enter through the vertebral foramen, (2) vertebral artery, (3) capillary bed and (4) annulus. (Image adapted from Martin et .al. 2002) [31]

Diffusion has been found to be the main mechanism for transport of nutrients into the intervertebral disc [30]. A landmark diffusion study was performed by Nachemson, in which a radiopaque dye was injected through cadaveric endplates, providing a visual description of the endplate diffusion pathway[7]. This study illustrated the nuclear central region as the main location of nutrient diffusion in the vertebral endplate and the cartilaginous endplate[7]. In order for the cells to maintain the ECM, they must obtain nutrients (glucose, lactate, amino acids and oxygen) via diffusion from the capillaries located in the adjacent vertebral structures [32]. Diffusion into the disc is driven by the concentration gradient between the blood plasma and the tissue matrix. It represents the balance between supply (capillary density) and demand (cell density and metabolic rate). The cartilage endplate acts as a selectivity membrane which is charge specific, freely allowing uncharged small solutes like oxygen, amino acids and water to diffuse across the endplate [33]. Larger solutes such as the blood plasma components, serum albumin and transferrin, may cross the endplate barrier by convective flow created by mechanical disc compression[34]. A cycle of load and recovery ranging from approximately 2.3 MPa to 0.1 MPa respectively provokes diffusive and convective transport, driving the nutrients in and metabolites out of the disc[7, 35]. This mechanical cycle is a characteristic of the diurnal cycle, which is provoked by physical activity creating compressive forces, driving water away from the disc and during rest, imbibing water back to the disc [36].

At an early age, capillaries perforate the hyaline cartilage endplate. After approximately two decades, with age the capillary bed recedes back to the center of the vertebra[37]. Therefore, the quantity of nutrient pathways decreases with age [38] as a

result some cells in the intervertebral disc may be as far as 8 mm from the closest nutrient source [27]. The average cell density in the nucleus pulposus (15 -56 age range) is 4×10^6 cells/cm³ and 9×10^6 cells/cm³ in the annulus [39]. For comparison, this density is considerably less than the cell density found in blood, which is 4.8×10^9 cells/cm³[40]. A decrease in nutrient supply with age may lead to apoptosis and may limit the ability of the nuclear cells to synthesize new extracellular matrix[9], leading to disc degeneration[41]. It may also limit cell division, may cause apoptosis and account for age – related decline in cell density [42].

1.4 Physical changes in the CEP and VEP

Poor disc nutrition may accelerate disc degeneration. When blockage occurs in the endplate, the disc may suffer nutrient deficiency affecting the health of the disc. Three physical changes that may affect the flow of nutrients into the disc are calcification in the cartilage endplate, sclerosis in the vertebral endplate and osteoporosis in the vertebra.

Calcification of the CEP stiffens tissues, restricting the movement and flexibility of collagen molecules [43]. The etiology of calcification remains unclear [44]. Additional long-term changes related to calcification may include loss of vertebral body height, osteophyte formation and disc space narrowing. [41]. A significant amount of calcification is reported in the cartilage endplates of patients with scoliosis [41], a disease identified by a sideways bend of the spine where both the IVD and the VB are wedged.

Another physical change that may block disc nutrition is sclerosis in the VEP. Sclerosis is the thickening of the bone at the vertebral endplates. Vertebral endplate sclerosis may originate from an abnormal motion between vertebrae and is sometimes seen in rheumatoid arthritis. This bone thickening has been associated with disc

degeneration [45]. A recent study investigated the pore size of the subchondral bone in VEP. Pore size openings from 20-50 μ m, in the capillary size range, were directly correlated to degeneration. It was observed that the number of pores in the bony endplate decreased with degeneration, indicating that the pores became larger with degeneration[46].

Disc degeneration has been linked to osteoporosis, a disorder affecting the bone density of adjacent vertebral bodies [47, 48]. Osteoporosis is prevalent in the elderly population. It is identified as a structural deterioration of bone illustrated by a thinning of the bone, increase in porosity and a bone mineral density (BMD) of more than 2.5 standard deviations below the mean of the young healthy reference population of the same gender, indicating a decrease in bone quality[49]. These changes in osteoporosis may increase the propensity to fractures, disrupt the biomechanics of the disc and promote disc degeneration[50, 51] [52].

1.5 Aging of the disc and disc degeneration

Physiologic aging and pathologic degeneration can be seen as similar processes; the only factor that may differentiate them is presence of symptoms including pain and the mechanical profile of the functional spine unit [9]. The disc is naturally prone to degeneration with age due to its hostile environment of heavy loads, low cellularity and avascularity[53]. The rate at which aging occurs could be dependent on many factors including, severe mechanical loading and/or a genetically inferior matrix [9]. These factors may decrease the synthetic capabilities of the disc cells, resulting in an accumulation of degradation products[9]. Consequently, GAGs degrade and breakdown by enzymatic degradation and this decreases water content[9], which in turn affects disc

height[54]. This degradation may cause the disc to collapse when exposed to heavy loads, which may trigger additional disc degeneration. The histological appearance of degeneration with aging and disc degeneration disease, such as loss of GAGs, loss of water and loss of disc height, have a tendency to overlap.

1.6 Disc degeneration classification

A non-invasive clinical MRI system is currently used to assist in disc degeneration classification. This systematic methodology was developed by Pfirrmann et al. focusing on five different characteristics of disc degeneration (Figure 1.4). The figure below presents the guidelines used to grade degeneration in discs on a scale of 1 to 5, with grade 1 being the healthiest and grade 5 being the most degenerated. This method shows a good correlation between radiographic markers with disc degeneration and histology.

Grade	Structure	Distinction of Nucleus and Anulus	Signal Intensity	Height of Intervertebral Disc
I	Homogeneous, bright white	Clear	Hyperintense, isointense to cerebrospinal fluid	Normal
II	Inhomogeneous with or without horizontal bands	Clear	Hyperintense, isointense to cerebrospinal fluid	Normal
III	Inhomogeneous, gray	Unclear	Intermediate	Normal to slightly decreased
IV	Inhomogeneous, gray to black	Lost	Intermediate to hypointense	Normal to moderately decreased
V	Inhomogeneous, black	Lost	Hypointense	Collapsed disc space

* Modified from Pearce (cited by Eyre et al⁹).

Figure 1.4 Pfirrmann classification of disc degeneration [55].

1.7 Permeability studies

Since a reduction of nutrition has been associated with disc degeneration, measuring the permeability of the endplate structure to nutrient flow can provide quantitative data about the correlation between the nutrient availability and disc

degeneration[41]. Permeability is defined as a measure of the ability of a porous material to transmit fluid [56]. Some animal studies have measured permeability[36, 57]and others have compared their permeability to disc degeneration [58, 59], however the permeability of human cartilage has not being reported before. Some qualitative information regarding human permeability was reported by Nachemson[7]. Animal studies have indicated that the range of permeability values between bone and cartilage might be as much as eight orders of magnitude [56, 57]. In order to make comparisons between the two components, the same measuring device is preferred. However, this wide range creates a challenge when measuring the permeabilities of the two-endplate components with one device. To date, permeameter devices have been constructed to measure the permeability of either bone or cartilage[56], but not both. Nauman's device quantified human trabecular permeabilities of bones in different locations in the body and found an average permeability of approximately $7.2 \times 10^{-7}(\text{m}^2/\text{Pa}\cdot\text{s})$ [56]. Setton's device measured baboon endplate cartilage at an average of $14.3 \times 10^{-14}(\text{m}^2/\text{Pa}\cdot\text{s})$ [57]. Overall, no studies have reported the permeability of the human endplate composite natural of structure,

Permeability is calculated using Darcy's law[56, 57]. In the endplate structure (porous material), the nutrient flow (fluid) is driven by a change in pressure from one direction to the other. Darcy's law is therefore expressed as $Q=AK\Delta P/L$. This equation states that volumetric flow, $Q(\text{m}^3/\text{s})$ of a liquid through a porous material is proportional to the flow area $A(\text{m}^2)$, the length of the specimen $L(\text{m})$, the pressure difference across the specimen $\Delta P(\text{Pascals})$ and a proportional constant $K(\text{m}^2/\text{Pa}\cdot\text{s})$. This constant K is

the permeability of the material. The following figure illustrates a one dimensional flow model (Figure 1.5).

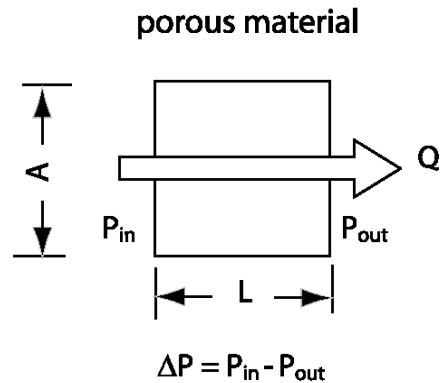


Figure 1.5 A one-dimensional flow of liquid through a porous material. Q is volumetric flow (m^3/s), A is the cross sectional area (m^2), ΔP is the change in pressure and L is the length of the specimen.

1.8 Imaging of vertebral endplate

In addition to permeability, bone morphology can also elucidate information about the vertebra's relationship to disc degeneration. VEP morphology can provide additional information to support the correlation between permeability and disc degeneration. The current methods available in clinical settings to quantify bone structure and bone mineral density (BMD) are Dual X-ray Absorptiometry (DXA) and quantitative computed tomography (QCT). These methods are practical but their resolution is insufficient to detect microscopic bone structural changes with age [60]. High-resolution micro computed tomography (MicroCT) is the current research standard tool used to quantify bone morphology and measure calcium density in bone[61]. MicroCT is used as a quantitative approach to measure high-resolution microstructural changes by acquiring and reconstructing virtual cross-sections[62]. It allows visualization

of the internal structures without destroying the samples. This tool consists of an X-ray source and a detector. The highest resolution currently available is a voxel size of 8 μm , which is able to measure trabeculae thickness (generally from 50-400 μm in thickness [21]). Three dimensional datasets are reconstructed and the grayscale values are converted to hydroxyapatite content (bone density indicator) using a linear calibration phantom [62]. The hydroxyapatite content is used to separate the bone and the pore pixels.

The morphology data obtained from the MicroCT device can be interpreted by calculating the sample's structural bone indices. Structural bone indices provide information about the architecture of bone in the vertebra. The most common bone indices selected to study bone properties and their relationship to osteoporosis are bone volume (BV/TV), trabecular thickness (Tb.Th), trabecular space (Tb.Sp) trabecular number (Tb.N) and bone mineral density (BMD)[19, 60, 63-65]. The indices reported in these studies are based on bone structure, but few studies have reported indices related to porosity such as pore number (Po.N) and pore diameter (Po.D) [66, 67]. These indices describing porosity would be useful to elucidate more information about the flow of nutrients through the vertebral endplate and its changes with disc degeneration.

1.9 Objectives

Previous studies of endplate diffusion have reported qualitative information regarding human endplate permeability [7, 68]. However, quantifying the endplate permeability is needed in order to understand the role that nutrients play in disc degeneration. The objective of this dissertation is to determine the role of endplate permeability and endplate microstructure on disc degeneration, by measuring changes in

endplate permeability potentially caused by disc calcification and/or sclerosis. The microscopic morphology of the adjacent vertebral endplate and IVD degeneration characteristics such as GAG content, cell density and disc height will be demonstrated.

The following work is presented in the next chapters:

- a. In chapter 2, the design, construction and validation of a custom-made permeameter are presented.
- b. In chapter 3, the permeability measurements of human endplate structure with and without cartilaginous endplate are presented. They are compared to disc degeneration parameters such as cell density and GAG content.
- c. In chapter 4, the morphology of the VEP is analyzed by quantifying the structural bone indices and then comparing them to permeability values and disc degeneration parameters.

We anticipate that the results of these studies will be helpful in determining the role of nutrients play in disc degeneration by focusing on the endplate structure of the disc and vertebrae.

Chapter 2 Permeameter Design and Validation

2.1 Introduction

Back pain is caused by many factors including disc degeneration. Disc degeneration may cause physical changes in the vertebral endplate and the disc, such as calcification and/or sclerosis in the endplate structure. The function of the endplate structure - to maintain disc hydration and allow nutrients in and out of the disc – may be altered by these changes. Since the disc cells get their nutrients via diffusion through the cartilaginous endplate (CEP) and vertebral endplate (VEP) [27] any nutrient blockage in one of the two endplate structures may play a role in disc nutrition and metabolite excretion changes. In order to estimate the relative ability of nutrients to diffuse through the endplate, the permeability - a material property that can be obtained by measuring the flow of fluid through a specific material over time using a permeameter - is measured. In the following chapters, we will determine the relationship of the endplate structure composite, the CEP and the VEP to disc degeneration and related parameters including cell density and proteoglycan content. We will quantify this contribution by measuring the nutrient permeability using a permeameter. The design and validation of our permeameter are presented in this chapter.

Currently there are no commercially available testing systems capable of measuring permeability over a range of values wide enough to encompass both the CEP and VEP at physiologic settings. Although the CEP and the VEP tissues can be measured independently in different devices, making measurements for the endplate structure, the CEP and VEP in the same permeameter system allows for comparison between the different tissues and it reduces artifacts caused by using different systems. Previous

authors have measured the permeability of non-composite tissues *in vitro* using custom-made devices. Setton designed a permeameter to measure baboon cartilage permeability, while Nauman designed a permeameter to measure trabecular bone permeability for different locations in the body including the vertebra [56, 57]. These devices performed well measuring the permeability of their respective tissues. However, they were not made to measure composite tissues over a wide range of permeabilities, such as the endplate structure, which may have a range of 8 orders of magnitude in permeability when the cartilage and bone are separated [56, 57].

In order to characterize the contribution of cartilage and bone endplate permeability, we designed, constructed and validated a permeameter device. In this chapter, we present the evolution of the design (generation 1 and 2), the selected system components and the methodology and results from the validation of the permeameter device.

2.2 Permeameter Design

Requirements for the Permeameter Design

A list of requirements was generated for our permeameter design based on our needs and on previous permeameter designs obtained from literature [36, 56, 58]. Generally, the permeameter must measure the permeability of the nutrients (fluid) diffusing through a sample at a physiological pressure.

The design characteristics of the permeameter are:

(a) The device must measure permeability at physiologic pressures (0.2 MPa – 2.3 MPa)[7, 35]. For this study 0.7 MPa was selected to represent an average nominal *in vivo* disc pressure.

(b) The permeameter must quantify the interstitial fluid permeability of the endplate at physiologic pressures for a wide range of permeability values ranging over 8 orders of magnitude (10^{-15} - 10^{-7} m⁴/N-s, cartilage and bone respectively [56, 57]).

(c) Cartilage and bone have irregular surfaces, which create small openings that allow fluid to leak around the specimens. Leakage around specimens has been a common problem in previous permeability studies [56, 58]. Therefore, in designing the permeameter, particular attention should be paid to leakage, which should be minimized around the specimen.

(d) In order to obtain physiologic values, a fluid similar to interstitial fluid must be used. We selected deionized water which was used previously in Nauman's study [56].

(e) The specimen holder must fit an 8.25 mm diameter sample. The selected sample diameter represents the minimum surface area contained in the nucleus pulposus. This diameter also meets the minimum standard diameter required to successfully measure the permeability of the bone tissue [69].

Permeameter-Generation 1 Components and Function

The first generation permeameter device design consisted of an aluminum syringe-like permeameter adapted from Nauman's study (Figure 2.1)[56]. It could be possible to adapt this device to increase its measurement range, but several modifications would be needed in order to accomplish this. We believed that this device could provide suitable data for our study because it was previously used to study the permeability of bone tissue. We anticipated that minor modifications to the specimen holder could be made to accommodate the added cartilage endplate tissue in our samples. In this design,

cylindrical endplate specimens are mounted within the cap of the permeameter and their flat surfaces are sealed with two rubber-o-rings (Figure 2.2). Fluid is forced through the specimen by an aluminum plunger driven by a servohydraulic materials test system (MTS Bionix 858, Eden Prairie, MN) operating under load control. The upstream fluid pressure is measured by an integrated pressure sensor (the fluid pressure differential ($P_u - P_d$) was maintained at 0.7 MPa). The downstream pressure is calculated based on the geometry of the device and assuming the outlet pressure is atmospheric. The fluid flow rate is calculated from the measured plunger displacement rate and the device geometry. Unfortunately, this device was not acceptable for several reasons. First, the specimen set up was laborious. Tightening the 12 screws that sealed the top plate to the external cylinder such that there was no gap that would cause leaks was challenging and time consuming. This required multiple iterations for each sample in order to achieve the necessary seal. In addition, the permeameter leaked at the junction between the top and the external cylinder. After multiple attempts with a variety of different gaskets, a temporary gasket was found. However, the solution required replacing the gasket frequently, (after about six tests showed an overall deterioration of the gasket) a 24 hour process. No permanent retrofit was possible. The aluminum plunger was also problematic; it wore overtime requiring disassembly between tests using a vise, causing additional artifacts to the test, such as an increase in friction between the cylinders. Fixing leakage after a failed test also led to the destruction of the specimen when the specimen was removed from the specimen holder. It was not possible to confirm if the specimen was seated correctly in the specimen holder. A missing feature for this device was real time data calculation, which could have expedited data analysis. Finally,

permeability decreased with time during the experiment, as opposed to the expected trend to be constant with time. It was suspected that this trend was due to debris present in the device. After multiple unsuccessful attempts to make steady measurements, the first generation permeameter was abandoned and a new design for a second-generation permeameter was designed and constructed.

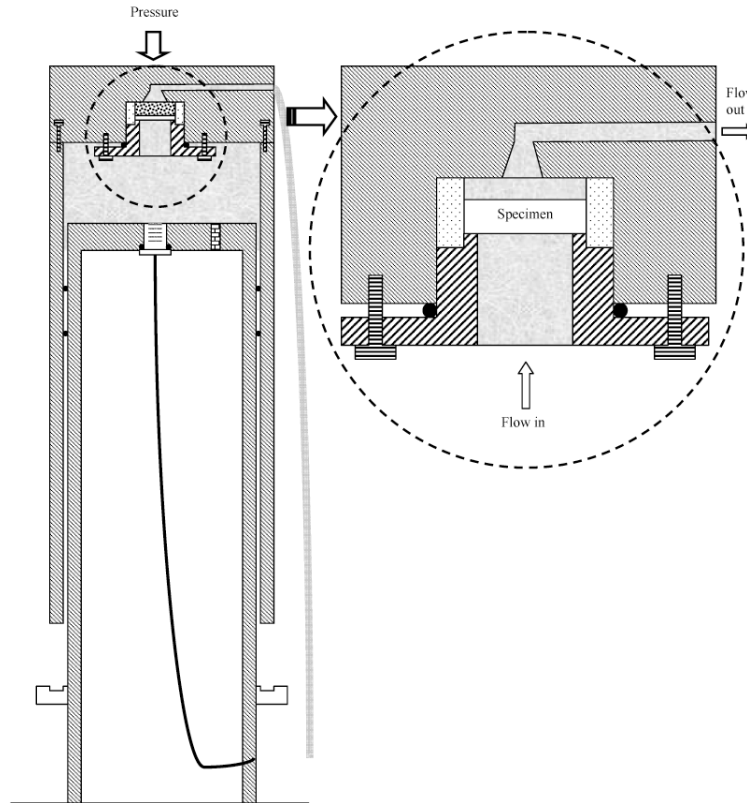


Figure 2.1 Schematic of device for endplate permeability measurement generation 1 [56].



Figure 2.2 Permeameter connected to MTS machine

Additional Requirements for Permeameter

Before the second-generation permeameter was designed, additional requirements were added to the list shown above to optimize the new permeameter based on the lessons learned during assessment of the previous design. The following requirements were added:

(f) The permeameter must contain a removable specimen holder to keep the sample from being damaged.

(g) The permeameter must measure permeability in real time to help monitor the fluid flow to the disc and detect whether the specimen has any defects as the test runs.

(h) A filter in the system to remove any debris in the fluid path must be included to reduce artifacts created by debris in the permeameter system.

Permeameter-Generation 2 Components and Function

Using the guidelines listed above, a second-generation permeameter was designed and constructed. A schematic of the second-generation permeameter is shown in Figure 2.3. The device is composed of stainless steel pipes connected to a water reservoir and a 0.05 micron filter (Absolute-Rated Membrane Filter Cartridges, PTFE 10” cartridge, McMaster Carr 6648T11), three valves to control the pressure, a safety valve, a water inlet and a water outlet. The permeameter is pressurized by a nitrogen tank. An external pump delivers water to the reservoir via the water inlet (maximum volume capacity of 1 liter). Before the fluid outlet, the device contains a removable specimen holder made up of a cryogenic vial cap with an outer o-ring that tightly fits an 8.25 mm diameter specimen (Cryogenic Vial, Corning Cat. No.2018 – 8.25mm in diameter and 11 mm deep).

The sample is placed in the specimen holder. First, cyanoacrylate is added to the periphery of the disc to prevent leakage. Then, high vacuum grease is applied around the cap’s o-ring (Dow Corning High Vacuum Grease DC 976) and the specimen holder is inserted in the permeameter (Figure 2.3). Deionized water is delivered to the reservoir using the external pump and the air trapped in the system is released using the vents (Figure 2.4). The upstream fluid pressure (P_u) of 0.7 MPa (100 psi) is generated in the nitrogen tank and measured by an integrated pressure sensor: the downstream pressure (P_d) is atmospheric (0.1MPa). The flow of water is calculated by weighing the amount of water collected by a beaker placed on a balance, (Ohaus, Cat No. AV2102CU-US, 2100g capacity, 0.01 g resolution, 3s stabilization time) converting it to m^3 units and dividing it by time (Figure 2.5). The time to run the experiment is selected based on the expected

permeability, where lower permeabilities require longer times. For the validation, the test runs for 10 minutes. The initial data (approximately the first 2 minutes) is used to stabilize the measurements by allowing the specimen to soak and any remaining bubbles in the system to evacuate. The permeability is then calculated as the average value over the remaining time (approximately 8 minutes). The pressure is recorded from the pressure transducer (Honeywell Sensotec, Model A205, 500 psi, infinite resolution). Finally, a LabView program (National Instruments Corporation, Austin, TX) is used to synchronize and collect data from the pressure transducer and the balance.

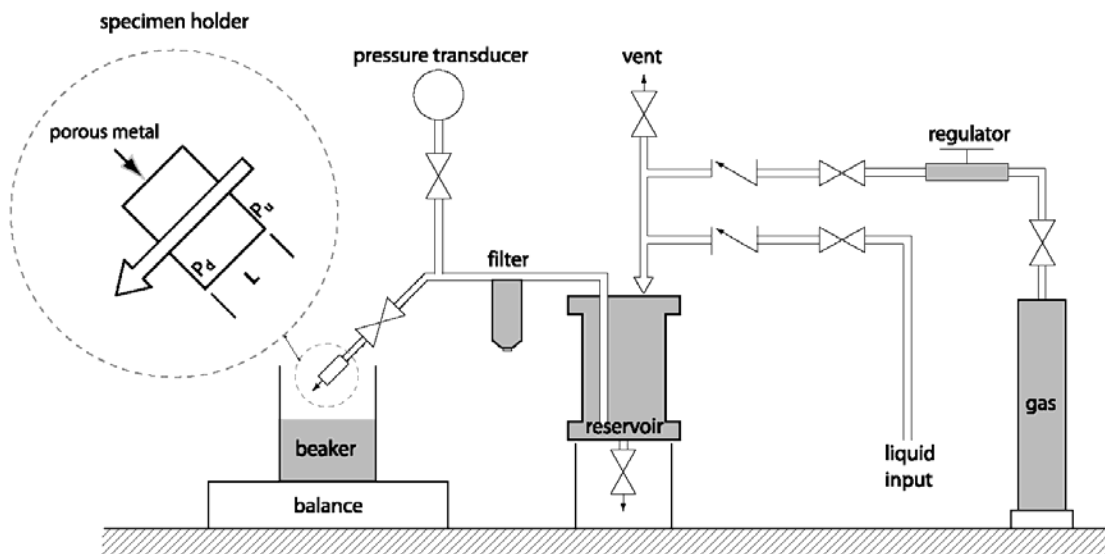


Figure 2.3 Illustration of the second-generation permeameter



Figure 2.4 Second-generation permeameter used for studies.

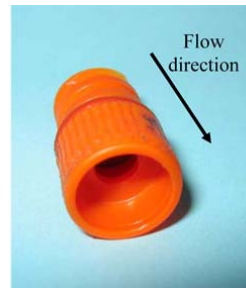


Figure 2.5 Fluid collection system for permeameter (top). Specimen holder close up (bottom)

The data collection system was designed to collect and synchronize time dependent data from the pressure transducer and the balance. The system is composed of a data acquisition board (PCI-6221, National Instruments, Austin, TX) with 4 different channels sampling at 5 MS/s, a shielded I/O connector box (SCB-68, National Instruments) and a PC computer running Windows XP. A program was developed using LabView software v7.1 (National Instruments, Austin, TX) for data acquisition. The acquired data was then analyzed with a custom-made MATLAB program, which used the

pressure transducer data, the weight of the water from the balance and the time of the test to quantify permeability as described in the next section.

Permeability Calculations

The fluid flow Q was calculated by dividing the weight of the fluid (m) passing through the specimen by the density of water (ρ) at three-second intervals (t), $Q = m/\rho t$. The sample's permeability (k) was calculated using Darcy's Law to relate the velocity (v) to the pressure drop across the specimen ($P_u - P_d$) per length of the sample:

$$v = \frac{V}{At} = \left(\frac{Q}{A} \right) = \left(\frac{k}{\mu} \right) \left(\frac{P_u - P_d}{L_s} \right) \quad \text{Equation 2.1}$$

Where V is the volume water (m^3), t is time (s), Q is the flow rate (m^3/s), A is the cross-sectional area for fluid flow (m^2), μ is the fluid viscosity ($0.001 \text{ N/m}^2\text{-s}$ for water), k is the permeability constant (m^2) and L_s is the specimen length (m). The final results were reported as intrinsic permeability in units of fluid mobility ($m^4/N\text{-s}$) and defined as the sample permeability normalized by the viscosity of the fluid (k/μ) [70-72]

Validation Guidelines

An acceptability criterion will be applied to this system to determine if the device is acceptable to measure permeability for bone and cartilage endplate tissue. The criteria for precision indicates that a variation under 10% is acceptable, 10-30% may be acceptable and over 30% is not acceptable [73]. Although, the absolute accuracy is not crucial to approve this device, since the contribution of bone and cartilage permeability to disc degeneration parameters will be sufficient to determine a relationship, the accuracy will be characterized for completeness. The precision will be reported as the standard

deviation of the repeatability tests. Finally, upper and lower permeabilities should encompass the bone and cartilage permeability range mentioned above.

2.3 Validation Methods

The methodology used to validate the second-generation custom-made permeameter is presented below. First, a leakage test was performed on the system. Second, a testing material with physical properties comparable to bone and cartilage was selected. Then, repeatability measurements were performed with the material selected to quantify the accuracy and precision of the system. The upper and lower limits were quantified and the data was analyzed and compared to the manufacturer values solving for accuracy.

Leakage Test

Since leakage is a known issue with these devices, a leakage test was performed. A solid specimen was placed in the specimen holder and pressurized at physiological pressure. The pressure was held for 15 minutes. Any drops of fluid which accumulated at the end of the specimen holder were recorded.

Selection of Standard Specimen

The requirements defined to select the best standard were the following: The material should be a porous material available in different porosities providing permeabilities between the testing range mentioned above (10^{-15} - 10^{-7} m⁴/N-s), be large enough to fit in our specimen holder (8.25 mm in diameter), be affordable and be able to sustain high pressures (>1.5 MPa). The materials explored included ceramic, polyurethane and stainless steel porous discs. After comparing each of the materials with

the requirements list, the stainless steel discs were selected as the best material to use for the permeameter validation based on their wide range of available permeabilities and affordability. In contrast, ceramic was rejected due to high cost. Polyurethane specimens did not provide an open continuous porosity to allow the fluid to get through.

The permeability of five porous stainless steel discs (0.2, 0.5, 1.0, 2.0 and 5.0 microns, Small Parts Inc PXX-K2-A) was obtained from the manufacturer in units of Darcy. Then, the manufacturer value was converted from Darcy units to m^2 units using the conversion factor of $1 \text{ Darcy} = 9.87 \times 10^{-13} \text{ m}^2$. Then this was divided by viscosity $0.001 \text{ N/m}^2\text{-s}$. The permeabilities of the 5 discs were therefore 2.47×10^{-11} , 1.02×10^{-10} , 2.23×10^{-10} , 6.57×10^{-10} , $1.25 \times 10^{-9} \text{ m}^4/\text{N-s}$. Although the complete range of permeabilities listed in the requirements is not covered by the selected validation samples, the samples fall in the middle of the range and the upper and lower range of the device can be computed using the resolution of the data acquisition devices.

Repeatability Study

The repeatability study was performed using 30 standard samples. Six samples at each of the 5 pore size discs were tested. The stainless steel discs are commonly used as filters to trap debris in water systems. In order to keep the discs from potentially accumulating debris from the system, we decided to test each disc only once to reduce the amount of confounding errors. The accuracy was quantified by comparing the measured with the manufacturer's stated permeabilities.

The following parameters were held constant: the length of the specimen ($L_s = 1.55 \text{ mm}$), the cross-sectional area of the specimen ($A = 5.34 \times 10^{-5} \text{ m}^2$) and the pressure

applied on the specimen ($P_u - P_d = \Delta P = 0.7 \text{ MPa}$). The flow rate was quantified using Equation 2.1.

Upper and Lower Limits of Permeability Range

The factors that affect the upper and lower ranges of the permeameter were examined (Figure 2.6).

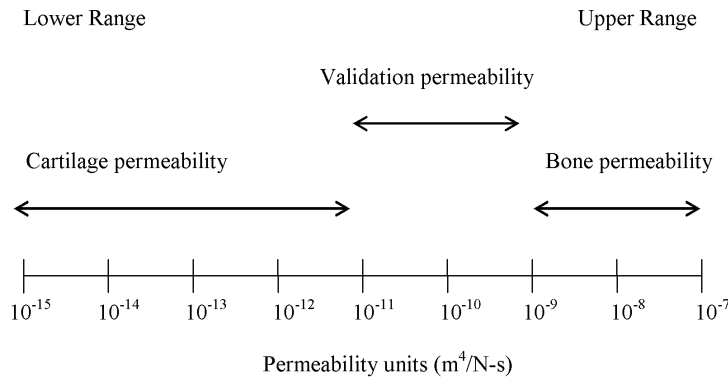


Figure 2.6 Permeability range for cartilage and bone and the validation range for the device.

Statistical Analysis

The precision range was quantified using the standard variation of each of the 5 porous discs for the repeatability results (Equation 2.2), where sd is the standard deviation, x is the value in each sample, \bar{x} is the mean of the values and n is the number of samples. The accuracy (% error) was quantified by calculating the percent error using Equation 2.3, which compares the manufacturer permeability with the measured permeability, where $k_{\text{manufacturer}}$ is the manufacturer's permeability obtained from the disc manufacturer and k_{measured} is the measured permeability obtained from Darcy's law (Equation 2.1). The manufacturer's stated permeability was correlated to the measured permeability. The least squares linear fit and the R^2 are reported.

$$sd = \sqrt{\frac{\sum (x - \bar{x})^2}{n - 1}} \quad \text{Equation 2.2}$$

$$\%error = \frac{|K_{manufacturer} - K_{measured}|}{K_{manufacturer}} \times 100 \quad \text{Equation 2.3}$$

2.4 Results

The permeameter was found to be acceptable for use in the proposed studies. A negligible amount of leakage was observed. The measured values were approximately 2-4 times the manufacturer values (Table 1). A linear equation fit provided the following relationship: Measured Permeability = 2.01(Manufacturer Permeability) + 2 x 10⁻¹⁰ with an R² = 0.95 (Figure 2.7).

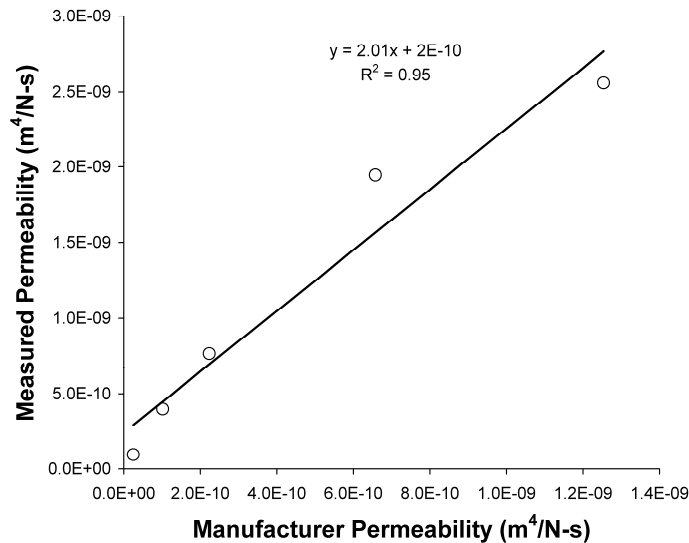


Figure 2.7 Comparison of the measured permeability with the manufacturer permeability. A linear fit was applied. The correlation has an R² = 0.95.

The measured permeability readings from the 0.2 to 5.0 micron porous discs were 9.5×10^{-11} ($\text{m}^4/\text{N}\cdot\text{s}$) to 2.6×10^{-09} ($\text{m}^4/\text{N}\cdot\text{s}$) discs respectively (Table 2.1). The standard deviation for the pore size samples ranged from 9% to 29% (Table 2.1, Figure 2.8)

Specimen (pore size μm)	0.2	0.5	1.0	2.0	5.0
$k/\mu(10^{-10} \text{ m}^4/\text{N}\cdot\text{s})$ – manufacturer	0.25	1.02	2.23	6.57	12.5
$k/\mu(10^{-10} \text{ m}^4/\text{N}\cdot\text{s} \pm \text{SD}\%)$ – measured	0.951 $\pm 20\%$	4.00 $\pm 9\%$	7.64 $\pm 29\%$	19.48 $\pm 18\%$	25.60 $\pm 13\%$
Percent error per porous disc type (accuracy)	286% (3.8x)	293% (3.9x)	242% (3.4x)	196% (3.0x)	104% (2.0x)

Table 2.1 Permeability values obtained for repeatability and accuracy. Permeability (k/μ) presented for manufacturer's and measured values

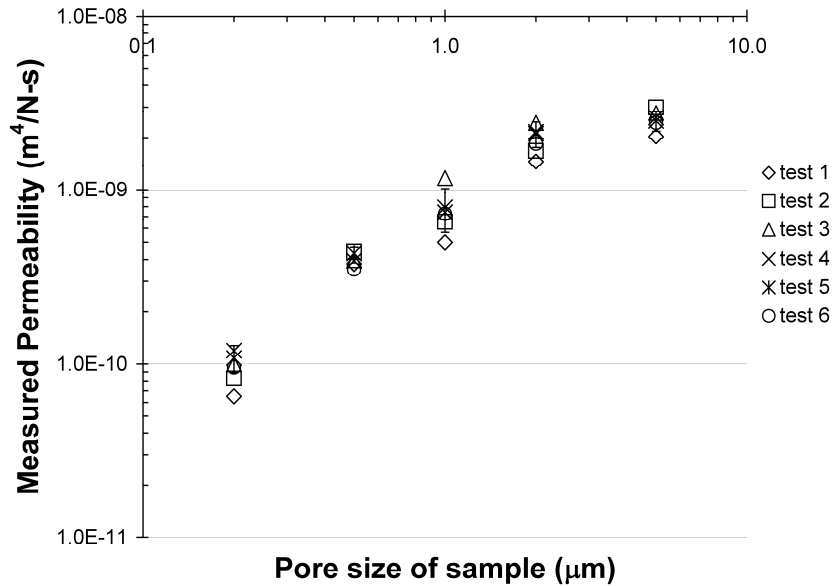


Figure 2.8 Repeatability of the permeameter for each of the 5 different pore size discs. Each disc type was tested 6 times and the variability is shown in the graph.

The upper and lower ranges of the permeameter were computed. In the upper range, the measurement is limited by the volume of fluid in the reservoir ($V=1$ Liter) and the highest data collection frequency (1 point every 3s). The flow rate (Q) at the upper range was calculated by converting 1 Liter to m^3 units and dividing by $t = 3$ s such that $Q=V/t$. This results in a flow rate of $3.33 \times 10^{-2} m^3/s$. Using this flow rate, the largest permeability measurable by the system is $K=4.45 \times 10^{-6} m^4/N\cdot s$. This is obtained by solving Equation 2.1 for the intrinsic permeability $K=k/\mu$ (Equation 2.4) and using the specimen inputs $L_s= 5.00$ mm, $A = 5.34 \times 10^{-5} m^2$ and $\Delta P=0.7$ MPa. L_s was chosen as a comfortable fit in the specimen holder, ΔP is the physiologic pressure and A is the cross sectional area of the specimen holder.

$$K = \frac{k}{\mu} = \frac{QL_s}{AP} \quad \text{Equation 2.4}$$

In contrast to the upper range, the resolution of the lower range is a function of the testing time. For example, a specimen in the $10^{-15} m^4/N\cdot s$ permeability range will have a flow rate of $7.48 \times 10^{-12} m^3/s$ (calculated using Equation 2.1). In this case, a weight of 0.01 g of water (the minimum change detectable by the balance) would be delivered every 1336 seconds (22 min). At this rate, it would take 7 hrs to collect 0.2 g of fluid and 21 hrs to collect 0.6 g of fluid.

2.5 Discussion

The permeameter device was successfully designed, constructed and validated. The results showed that the accuracy and the precision are acceptable for this device based on the acceptability criteria listed above.

The measured values were 2-4 times different from the manufacturer reported values. These ranges of values could be explained by different factors. For example, the manufacturer values were obtained under different testing conditions compared to this study. Some unknown variability with the samples was present and potentially other factors such as tortuosity, could explain these differences. The measurements obtained are acceptable for our permeability studies. The main goal of the permeability studies in the next chapters is to determine the relationship between permeability (in both the bone and cartilage) and degeneration parameters. For that reason, only relative comparisons are necessary. The expected difference in permeability variation within bone is two orders of magnitude and within cartilage is five orders of magnitude. When this difference is compared to the accuracy of the permeameter, then it can be seen that the accuracy difference is trivial when comparing a wide range of permeabilities expanded over a few orders of magnitude. Therefore, this difference does not affect the final results. At the other extreme, if the permeability considered for either bone or cartilage falls within the same magnitude, then the difference in accuracy will not affect our conclusions because all the values will be off by the same order of magnitude. The only time when relative differences in accuracy could be a problem would be if the permeability values fall in the range of 10^{-8} or higher. This last scenario is not relevant because the permeameter is not designed to function in this range. In summary, the accuracy obtained from the validation study shows that the permeameter is acceptable to use for our studies in the next two chapters.

The precision range of the machine was 9-29%. Although the values obtained fall in the middle-acceptance range of the acceptability criteria, the precision obtained is

satisfactory for our permeability study. When the inherent variability within the tissues is considered, this can affect the results in different ways. If the precision value for the specimens is less than the difference between the specimens, then the precision value is acceptable. If the difference in precision is higher than the difference between each of the tissues than the difference between the tissues cannot be distinguished. For that reason, a power calculation should be used to determine the number of samples needed to discern differences in the upcoming tissue studies. One of the limitations of this machine was that the pressure control system was not constant for all of the samples. This could explain the mixed standard deviation values obtained for each of the porosities measured. For example, the permeability for the smallest porosity (0.2 micron) had a standard deviation of 20% or $\pm 9.5 \times 10^{-11}$ and the largest porous disc (5.0 micron) had a standard deviation of 13% or $\pm 2.56 \times 10^{-9}$. When the permeability was high, the nitrogen tank pressure system had difficulties delivering enough nitrogen gas to keep the system at a constant pressure. This problem with pressure was not present at low permeabilities. Another limitation of the validation, which could explain the disparity in precision values in the system, involves the potential debris left in the porous metal discs from machining dust. The discs were cut to fit in the specimen holder (8.25mm) from their original diameter of (12.7 mm). This could provide additional explanations for the variation in the validation samples. However, we believe that the debris in the system is negligible and will not have an effect on the real tissue samples. Based on this rationale, the precision of the second-generation design is acceptable for the studies that will be performed in the following chapters.

The upper and lower limits specified in the acceptability criteria will be reached successfully by the permeameter system. An upper limit of permeability of 4.45×10^{-6} $\text{m}^4/\text{N}\cdot\text{s}$ is obtainable. In order to successfully measure the permeability at the lower limit, the testing time must be increased in order to obtain a sufficient amount of fluid. We recommend a minimum of seven hours of testing time, which corresponds to least 0.2 g of fluid collected to allow for both system stabilization and a sufficient number of data points to perform the calculations. In addition, we recommend a maximum time of 21 hrs, which corresponds to 0.6 g of fluid, to minimize specimen degradation. Note that when these long times are used the beaker should be covered to avoid water evaporation. These results show that this device can effectively measure permeabilities in the expected range shown in Figure 2.6.

In summary, we validated the device within 3 orders of magnitude - 10^{-9} to 10^{-11} $\text{m}^4/\text{N}\cdot\text{s}$ - in the cartilage and bone permeability range. The upper and lower limits calculations showed that the device has a wide range of permeability detection. This device is able to make sufficiently precise measurements of permeability for a variety of tissues, in this case cartilage and bone. It meets the accuracy requirements for the studies planned in the next chapter. This permeameter will aid in elucidating information about the nutrient diffusion of the intervertebral disc and how it leads to degeneration.

Chapter 3 Human Disc Nucleus Properties and Vertebral Endplate Permeability

3.1 Introduction

The central intervertebral disc (IVD) loses its blood supply in the first decade of life [8] [74]. This avascularity causes disc cells to rely on diffusion and convection for nutrient and metabolite exchange, principally with capillaries in the adjacent vertebral bodies [30, 58, 75]. Early work by Nachemson [7], demonstrated that endplate capillaries are more numerous at the disc center, where the disc is tallest and cellular competition for nutrients is greatest [27, 76]. The vertebral endplate has subsequently been shown to be the principal route for nucleus cell nutrition [77, 78].

Clearly, sustaining adequate transport is critical to disc health, as cells maintain the extracellular matrix (ECM) and regulate the biochemical environment [79, 80]. Over thirty years ago, Nachemson hypothesized that endplate calcification may impede disc cell nutrition and lead to degeneration [7]. Since then, this has been analyzed theoretically [81], and experimentally in vitro where a restriction in nutrient supply has been shown to reduce the number of viable or functional cells [27]. This notion is supported by several studies that report differences in diffusion pathways between healthy and degenerate discs [82-84].

Transport linking endplate capillaries to disc cells is controlled by direction-dependent interactions between cartilage endplate and subchondral bone [36, 85, 86]. Hence, one mechanism for adversely affecting cell function is reduced cartilage permeability via calcification [38, 41]. Alternatively, subchondral bone sclerosis may result in fewer and smaller pores through which transport can occur [46]. While

qualitative evidence suggests one or more of these mechanisms underlie disc degeneration, quantifiable relationships between disc cellularity, endplate permeability, subchondral bone porosity, and matrix content are unavailable.

Establishing such associations would help clarify disc degeneration pathomechanisms. Further, if degeneration is causally linked to transport inadequacy, then patient-specific risk factors that initially lead to degeneration may be detrimental for subsequent efforts at stimulating disc repair. That is, therapeutic increases in disc cell number and/or metabolic activity may not be achievable and sustainable within this transport constrained environment. The goal for this study was to investigate univariate relationships between human endplate morphology, permeability, disc cell density, matrix content, and radiographic evidence of degeneration in attempts to establish quantitative relationships that would be useful for disc degeneration/regeneration research.

3.2 Materials and Methods

Dissection

Thirteen freshly frozen cadaveric human lumbar spines from levels L1-L5 and L1-L4 (age range 32-85 years; average age 63 ± 16 years; 4 females and 9 males) were obtained from donor banks. Overall, 51 motion segments were harvested. No attempt was made to preselect samples with osteoarthritis or osteoporosis; therefore, they only represent a random sample of the population. The specimens were kept at -20°C until they were thawed for MRI assessment. The intervertebral disc (IVD) specimens were scanned in a 3T MRI Scanner (GE Healthcare, Milwaukee, WI) and graded by three trained radiologists using the Pfirrmann degeneration scale [55]. In order to obtain the

average IVD height, three locations were selected and measured from mid-sagittal MRI images using NIH Image software: one from each lateral side and one at the center. The posterior processes were removed using a bone saw (Exakt Model 300, Band Saw, Norderstedt, Germany). Subsequently, the surrounding muscle and other soft tissue were dissected away from the spine. The motion segments were then cut transversely in each vertebra using a bone saw to obtain specimens consisting of half-vertebra/disc/half-vertebra (Figure 3.1). Next, they were refrozen for the following two steps, to preserve nuclear tissue. The motion segments were cored at the center of the nucleus pulposus using an 8.25 mm (inner diameter) diamond coring tool (Starlite Industries, Rosemont, PA) and a drill press. In the transverse plane, the center of the nucleus pulposus was approximated by marking a point one-third of the anterior-posterior length along the sagittal midline. Next, the adjacent vertebra/endplate core was separated from the nuclear tissue. In order to keep the cartilage endplate intact, the nucleus tissue was cut approximately 1 mm away from the cranial and caudal ends of the adjacent vertebra. Then, the nucleus was carefully divided in three roughly equal parts along the axial length of the nuclear core and labeled in reference to the adjacent vertebrae: superior, center and inferior (Figure 3.1). The 102 vertebral/endplate cores were stored at -20°C for later use in MicroCT imaging.

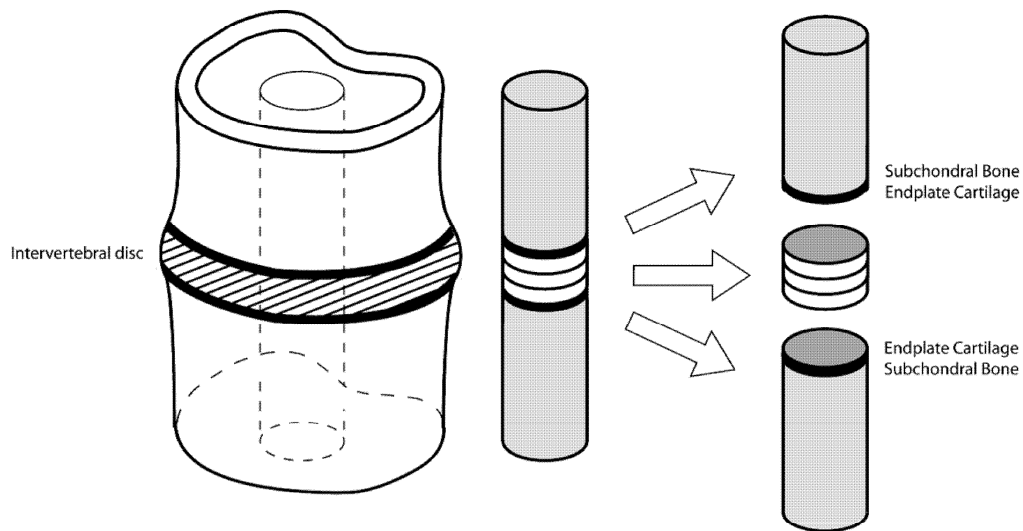


Figure 3.1 Schematic of endplate specimen harvest. Specimen was cored from the frozen motion segment (8.25 mm diameter). The cartilage endplate attached to the vertebral cores was separated from the nucleus pulposus tissue for MicroCT (μ CT) and permeability measurements. The nuclear tissue was separated in three parts, which were labeled in reference to the adjacent vertebra: inferior (1), center (2), superior (3) for biochemical measurements.

Imaging

The vertebral bone cores were thawed and imaged in a commercial micro-computed tomography system (μ CT 40, Scanco Medical, Brüttisellen, Switzerland) with an X-ray tube voltage of 70 kV and 180° acquisition. Fifteen cores were excluded due to technical issues. Each core was placed in a cylindrical sample holder in a bath of protease inhibitors diluted 1:10 with distilled water (P2714 Protease inhibitor cocktail, Sigma-Aldrich, St Louis MO) to keep the cartilage in the specimens from degrading [57]. A spatial resolution with an isotropic voxel size of 8 μ m (matrix 2048 x 2048, 1000 projections/180°, FOV 16.4 mm) was chosen. Specimens were scanned along the length of each core, encompassing the vertebral endplate surface and 3 mm of bone underneath

it. Next, image cross sections were reconstructed to create a 3D structure using the manufacturers' cone beam reconstruction algorithm [60]. Then each 3D structure was transformed into 1000-1100 serial-8 μ m thick-sliced images in a sagittal orientation. Next, a light Gaussian filter (to remove high frequency noise) followed by a fixed threshold was applied (to segment the images into a bone and pore phase) [64]. The irregular vertebral endplate surface was then identified using a custom-made algorithm developed using MATLAB software. The semiautomatic technique is fully described elsewhere [87]. For each sagittal μ CT image, this algorithm identified a single region of interest (ROI) that included an 8 μ m (one pixel) thick endplate surface contour. For each contour, the bone volume fraction (BV/TV) was calculated, where BV is bone volume and TV is tissue volume (equivalent to the ROI volume). The porosity was calculated as the average of $1-BV/TV$ for the series of sagittal images for each specimen (Figure 3.2).

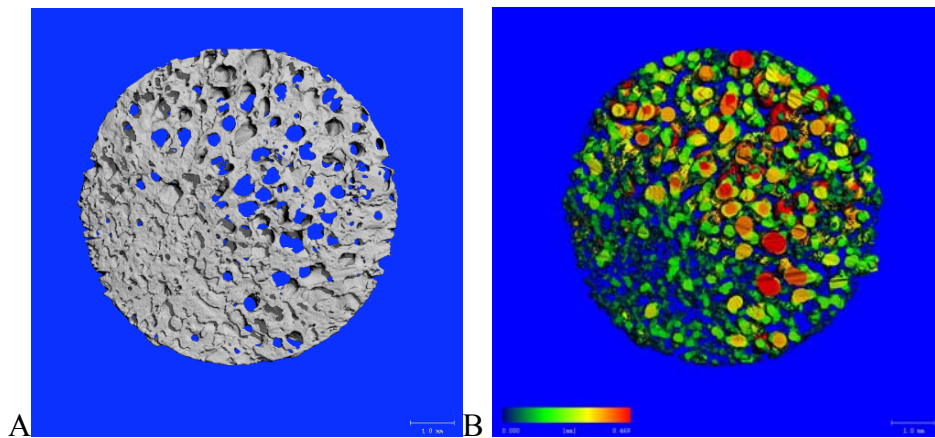


Figure 3.2 A MicroCT transverse view of a subchondral endplate is shown on the left (A). The open pores are filled using a method that highlights the size of the pores by using a color scale right (B)

Permeability testing

After the vertebral bone specimens were scanned, the specimens were trimmed to approximately 5 mm from the vertebral endplate surface using a low concentration

diamond wafering blade on a Buehler Isomet Circular Low Speed Saw. The marrow was then removed from the trabecular bone using a water pik (Waterpik, CO) and the cores were stored at -20°C . A custom-built permeameter was used to measure the hydraulic permeability of the endplate cores. The permeameter consists of a series of pipes connected to a pressurized fluid reservoir (Figure 3.3) and was validated using porous stainless steel discs of known permeability (Mott Corp, Farmington, CT) [88].

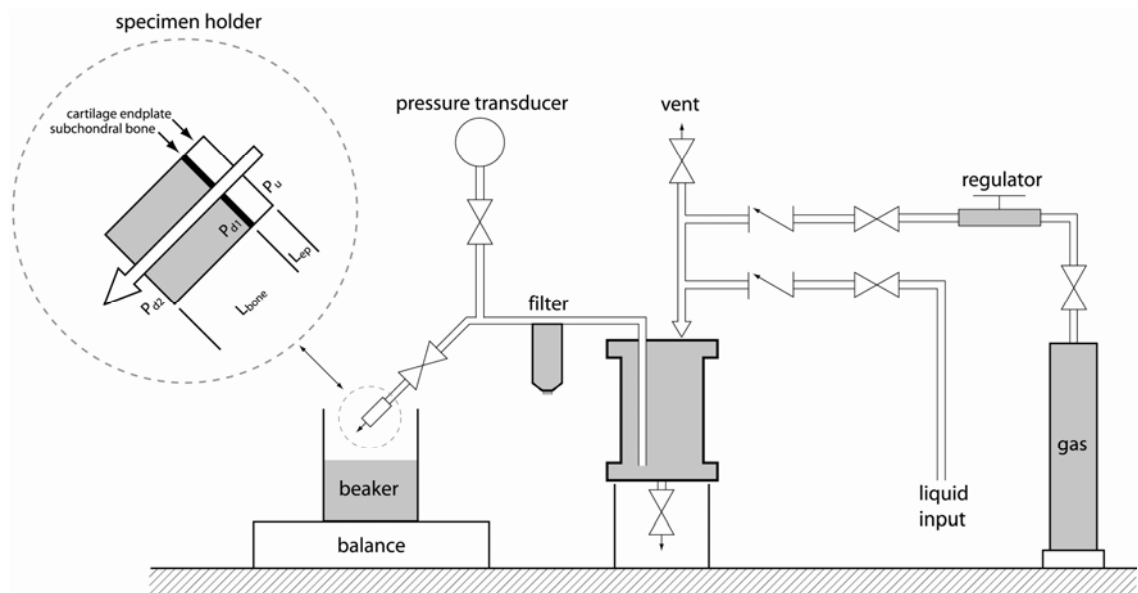


Figure 3.3 Illustration of the permeameter. The custom-made permeameter is composed of stainless steel pipes connected to a water reservoir. These pipes are also connected to a pressure transducer, a safety pressure release valve, fluid outlets, a filter and a specimen connector. The fluid is pressurized to 1 MPa and pressed through the cartilage-bone specimen. A schematic of the test specimen is shown on the top left corner where P_u is the upstream pressure, P_{d1} is the pressure downstream of the cartilage endplate, and P_{d2} is the pressure downstream of the subchondral bone.

Permeability measurements were performed on 51 vertebral/endplate cores, one from each motion segment. The locations (inferior or superior) were randomized and the matching core was saved for a future study. To assess the permeability of the cylindrical core samples, they were first thawed and then placed in perforated cryogenic vial caps

(Cryogenic Vial, Corning Cat. No.2018). Then, cyanoacrylate glue was carefully added to seal the cartilage endplate periphery to prevent leaks around the specimen. The samples were oriented so that the driving hydraulic pressure was against the cartilage endplate so that fluid passed in the flow-out, disc to bone direction [36]. We chose the flow-out direction for two reasons. First, several groups have demonstrated that nucleus pressure compacts cartilage endplate leading to decreased matrix pore size and lower permeability [36, 89]. Because of this, we adjusted the apparatus flow to correspond with physiologic disc pressures so cartilage endplate compaction in our experiment would match that present *in vivo*. In that way, we expect our data to be more representative of *in situ* conditions. A similar choice was made by other groups [90, 91], and consequently this also allowed a representative comparison to historical data. Second, the cartilage endplate is only loosely adherent to the subchondral bone, and our preliminary attempts at measuring permeability in the flow-in direction damaged the specimens by separating tissues. The cartilaginous portion of the sample in the cryogenic vial was equilibrated in protease inhibitors diluted 1:10 in distilled water for at least half an hour to reduce cartilage degradation. The sample in the vial was then inserted in the sample mount and ready for testing. The permeameter was filled with deionized water and pressurized to 1 MPa – the average physiological pressure of the disc [92]. The fluid flow rate was calculated by measuring the weight of the fluid passing through the specimen at two-second intervals using a precision electronic balance (Ohaus, Cat No. AV2102CU-US, 2100g capacity, 0.01g resolution). The upstream fluid pressure (P_u) was generated using a nitrogen tank and was measured by a pressure sensor (Honeywell Sensotec, Columbus, Ohio, Model A-205). The downstream pressure (P_d) was atmospheric.

Specimen's permeability (k/μ) was calculated using Darcy's Law to relate the Darcy velocity (v) to the pressure drop across the specimen (P_u-P_d): where Q is the flow rate (m^3/s), A is the cross-sectional area for fluid flow, μ is the fluid viscosity (Pa-s), the Darcy permeability constant k , is the intrinsic property of the tissue (m^2), and L_s is the specimen length (m).

$$v = \frac{V}{At} = \left(\frac{Q}{A} \right) = \left(\frac{k}{\mu} \right) \left(\frac{P_u - P_d}{L_s} \right) \quad \text{Equation 3.1}$$

Each specimen's permeability was measured twice, once intact, and a second time; after careful removal of the cartilage endplate using blunt dissection and Toluidine blue tissue marker to differentiate the cartilage from the bone. The cartilaginous endplate thickness (L_{cep}) was then measured using a resistance micrometer [93]. The cartilage endplate permeability was calculated assuming 'permeabilities in series'; that is, for the intact specimen, the flow is equal through both the cartilage endplate (cep) and subchondral bone (bone) (see also Figure 3.3).

$$\frac{Q}{A} = \frac{Q_{cep}}{A} = \frac{k_{cep}}{\mu L_{cep}} (P_u - P_{d1}) = \frac{Q_{bone}}{A} = \frac{k_{bone}}{\mu L_{bone}} (P_{d1} - P_{d2}) = \frac{k_{total}}{\mu L_{total}} (P_u - P_{d2}) \quad \text{Equation 3.2}$$

$$Flow = \frac{Q_{cep}}{A} = \frac{Q_{bone}}{A} = \frac{Q_{total}}{A}$$

From the intact specimen flow experiments, total permeability (k_{total}) in Equation 3.2 was determined. From the bone-only flow experiments, bone permeability (k_{bone}) was determined. Using these quantities, and the pressure-drop/flow-rate relationships from the intact specimen test, cartilage endplate permeability (k_{cep}) was determined from Equation

3.2 by first solving for P_{dl} and then for K_{cep} . The final results were reported in fluid mobility units ($m^4/N\cdot s$) and defined as the tissue permeability normalized by the viscosity of the fluid (k/μ).[70-72].

Biochemistry

Cell density was quantified by measuring DNA fluorescence using the PicoGreen assay method (Molecular Probes Invitrogen Detection Technologies, Eugene, OR) following the manufacturer's protocol. First, the stored nuclear tissue was thawed out for 3 minutes. Each nuclear section (inferior, center and superior) was finely minced, weighed to obtain wet weight, and then lyophilized in order to obtain dry weight. The water content was quantified by measuring the difference between these two weights. Samples were digested using papain (Sigma-Aldrich) prepared at a dilution of 1:100 in PBS for 24-36 hours at 60° C and then centrifuged at 3000 rpm for 10 minutes to separate the sample into a pellet containing cells and supernatant containing GAGs. The pellet was then resuspended in 300 mL of TE buffer (Sigma-Aldrich) and used to estimate nucleus cell density, while the supernatant was used to determine nucleus glycosaminoglycan (GAG) content. In a validation study (Appendix A), it was determined that the amount of DNA in the supernatant was negligible compared to the amount of DNA found in the pellet; for that reason the DNA was only obtained from the pellet. The amount of DNA was quantified by using the results from a standard curve produced using a calf thymus DNA concentration. Finally, the cell density was calculated by dividing the amount of DNA by 6 picograms of DNA which are contained per cell [94].

Nucleus GAG content was quantified using the dimethylmethylene blue assay (DMMB) method with the supernatant from the nucleus digestion [95]. The supernatant

was diluted to 1:200 and then 40 μL of the solution was added to 250 μL of the DMMB dye solution. A wavelength reading was measured using a spectrophotometer (SpectraMax M3, Sunnyvale, CA). The GAG content was calculated based on a standard curve using an aqueous solution of chondroitin sulfate C from shark cartilage (chondroitin 6-sulfate, Sigma Aldrich, St. Louis, MO). The results were normalized by volume (mm^3) from the water content previously obtained.

Data Analysis

All statistical analyses were performed using the JMP (Version 7.0, SAS Institute Inc.). Interobserver variability for degeneration scores was determined by a kappa score. Means and standard deviations for the variables were obtained. Pairwise linear and power fit regressions were performed to analyze relationships between relevant variables [permeabilities (total, cartilage and bone), porosity, endplate cartilage thickness, age, disc height, cell density, GAGs, GAGs/cell]. The linear fit was applied first, if a nonlinear relationship was encountered a power fit was then applied. The best fit was determined to be that which resulted in the largest R^2 value. The statistically significant variables were further investigated using stepwise multiple regression models. The stepwise multiple regression models were assessed by using hydraulic permeability, cell density, GAG content, GAGs/cell individually as the dependent variables and were assessed as a function of (degeneration grade entered as an ordinal predictor, porosity, age, endplate cartilage thickness, and disc height entered as continuous predictors) and the remaining variables not use as the independent variable.

Permeability, Porosity and Cartilage Thickness.

A one way ANOVA was used to compare porosity to degeneration. Then, a one-way repeated measures ANOVA to compare degeneration grade to vertebral level by donor was completed. A one way ANOVA was used to compare the differences between inferior and superior permeability.

Cell Density, GAGs and GAGs/cell

A one way repeated measures ANOVA was used to compare the variation between the inferior, center and superior locations of each disc for cell density and GAG content. A one way ANOVA was used to compare degeneration to cell density, GAG content and GAGs/cell. When appropriate, Tukey post-hoc tests were used to identify group differences.

Degeneration

Analysis of variance was used to compare the effect of degeneration on age and disc height. Also a one way repeated measures ANOVA comparing degeneration with vertebral levels was performed. When appropriate, Tukey post-hoc tests were used to identify group differences.

3.3 Results

Of the 51 discs, 2 were scored Pfirrmann grade 1, 18 discs were grade 2, 21 were grade 3, 6 were grade 4, and 4 were grade 5. The disc tissue for one segment was subtracted because it was absent due to extreme degeneration. The calculated kappa value rating interobserver agreement on grading degenerative changes of the disc had a fair agreement (calculated k value was 0.41).

Endplate Permeability, Porosity & Cartilage Thickness

The mean total hydraulic permeability was $3.26 \times 10^{-10} \pm 4.43 \times 10^{-10} \text{ m}^4/\text{N}\cdot\text{s}$. For the cartilage endplate alone, the permeability was $1.19 \times 10^{-10} \pm 1.64 \times 10^{-10} \text{ m}^4/\text{N}\cdot\text{s}$ while that for the subchondral bone alone was $22.1 \times 10^{-10} \pm 13.7 \times 10^{-10} \text{ m}^4/\text{N}\cdot\text{s}$. Total hydraulic permeability (THP) had a positive correlation with age and bone porosity ($R^2=0.16$, $p<0.01$, $\text{THP} (x 10^{-10}) = 0.11*\text{age} - 3.80$ and $R^2=0.09$, $p=0.05$, $\text{THP} (x 10^{-10}) = 16.13*\text{bone porosity} - 5.33$, respectively; Figure 3.4 and Figure 3.5). Bone permeability also had a positive correlation with age and bone porosity ($R^2=0.10$, $p=0.03$, $\text{Bone Permeability} (x 10^{-10}) = 0.27*\text{age} + 4.89$ and $R^2=0.23$, $p<0.001$, $\text{Bone Permeability} (x 10^{-10}) = 75.15*\text{bone porosity} - 18.69$, respectively; Figure 3.6 and Figure 3.7). In addition, bone permeability was compared to GAG content, a power equation was fitted as follows; $\text{Bone Permeability} = 44.18*\text{GAG content}^{-0.6}$ ($R^2=0.14$, $p=0.02$; Figure 3.8). Out of 102 vertebral cores, fifteen cores were excluded due to inhomogeneities. The mean endplate porosity was $54.6 \pm 7.5\%$ and was positively correlated with age ($R^2=0.13$, $p<0.01$; Figure 3.9) and degeneration ($R^2=0.19$, $p=0.04$; Figure 3.10). It was observed that cartilage thickness increased with age ($R^2=0.08$, $p=0.03$). The results of the one way repeated measures ANOVA showed that no relationship was found in degeneration grade with different vertebral levels, $p=0.94$. Total and cartilage permeability was observed to increase with vertebral levels from L1 to L5, but the relationship was not statistically significant. The results of the one way ANOVA showed that inferior and superior permeability (total, cartilage and bone) were not statistically different either.

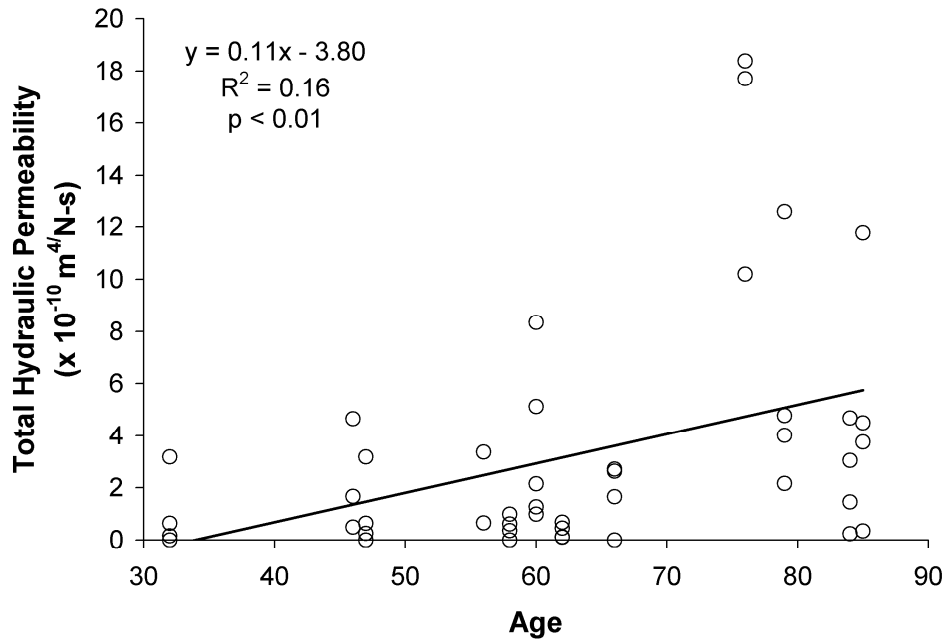


Figure 3.4 Total hydraulic permeability (THP) had a positive correlation with age (THP ($\times 10^{-10}$) = $0.11 \times \text{age} - 3.80$; $R^2=0.16$, $p<0.01$).

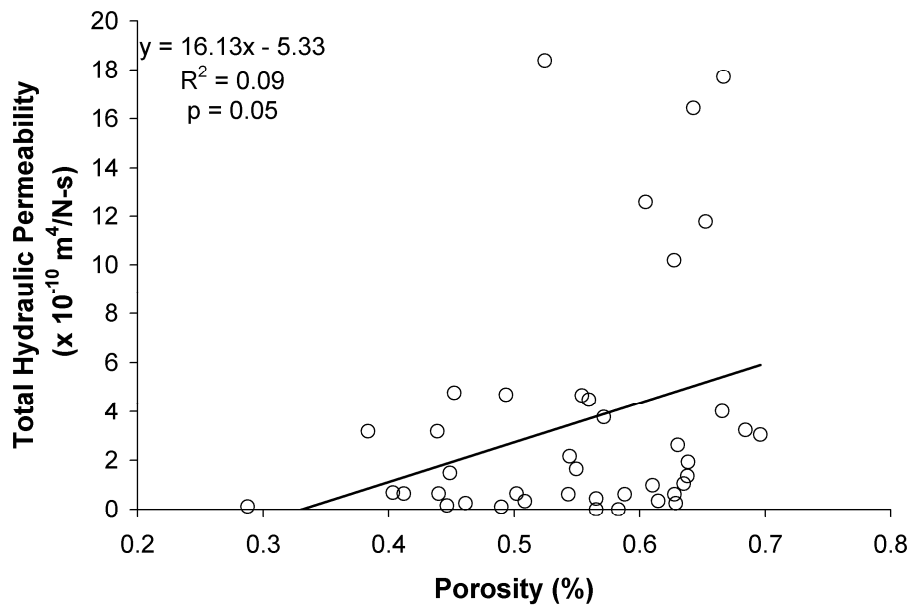


Figure 3.5 Total hydraulic permeability (THP) had a positive correlation with bone porosity (THP ($\times 10^{-10}$) = $16.13 \times \text{bone porosity} - 5.33$; $R^2=0.09$, $p=0.05$).

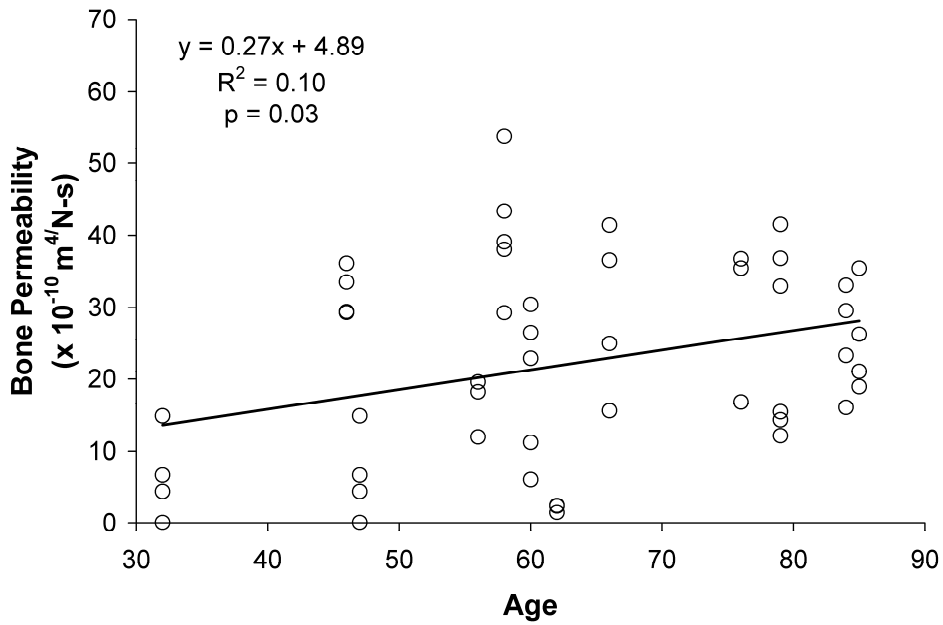


Figure 3.6 Bone permeability also had positive correlation with age (Bone Permeability $(x 10^{-10}) = 0.27 * \text{age} + 4.89$; $R^2=0.10$, $p=0.03$).

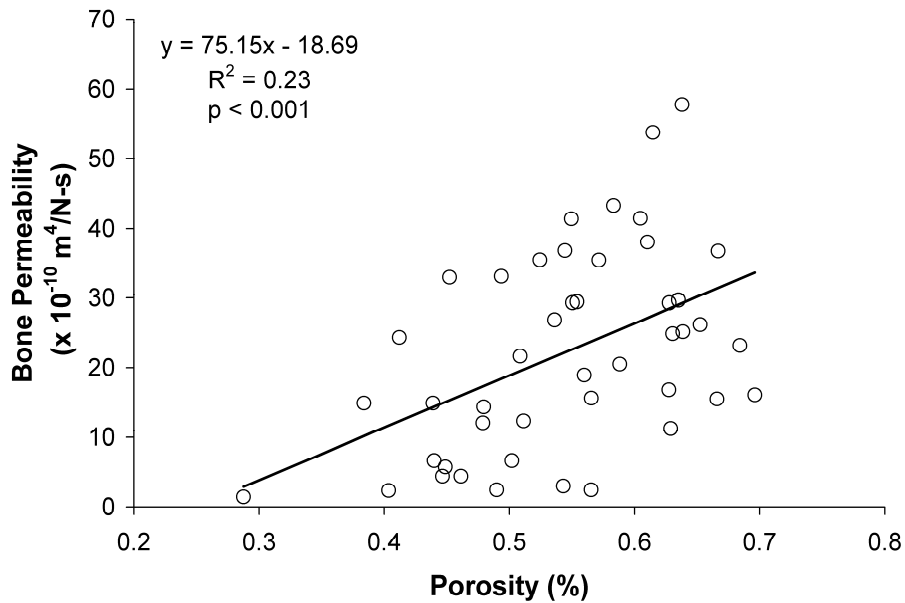


Figure 3.7 Bone permeability also had positive correlation with bone porosity (Bone Permeability $(x 10^{-10}) = 75.15 * \text{bone porosity} - 18.19$; $R^2=0.23$, $p<0.001$).

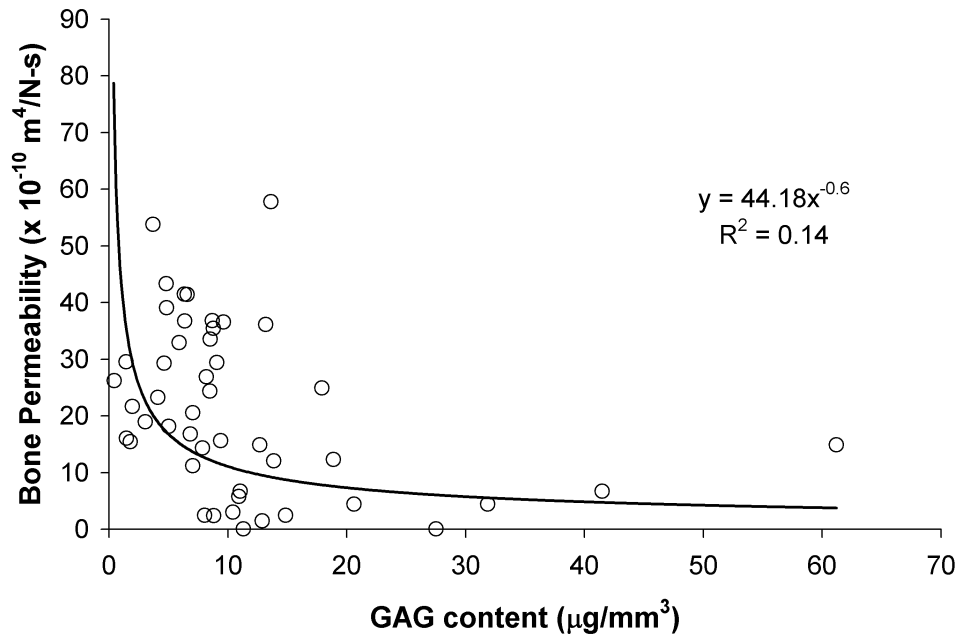


Figure 3.8 The variation of Bone permeability with GAG content. Data fitted with a power equation, (Bone Permeability = 44.18*GAG content^{-0.6}; R²=0.14, p=0.02)

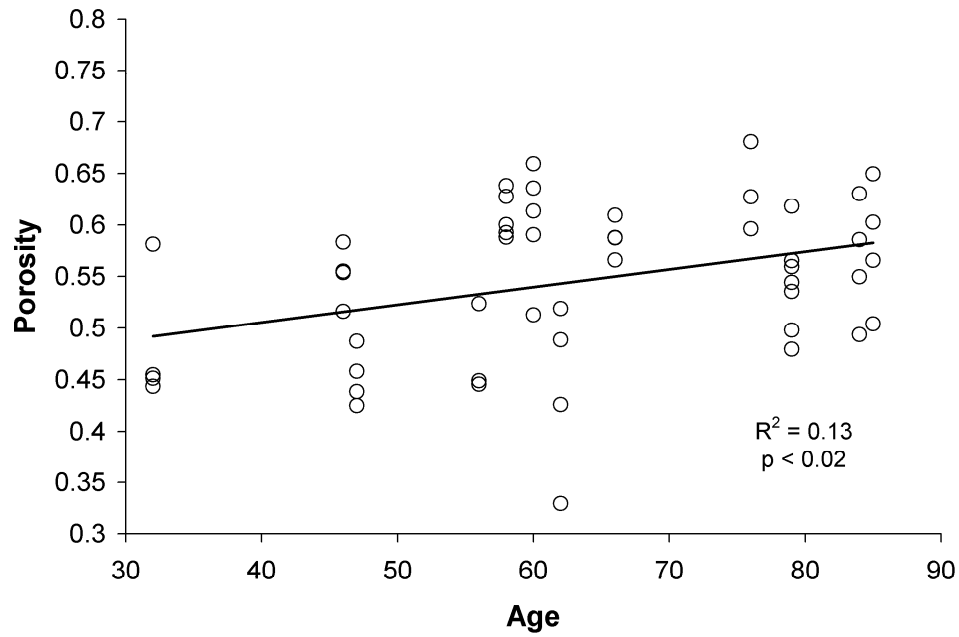


Figure 3.9 The variation of subchondral bone porosity with age (R²=0.13, p=0.004).

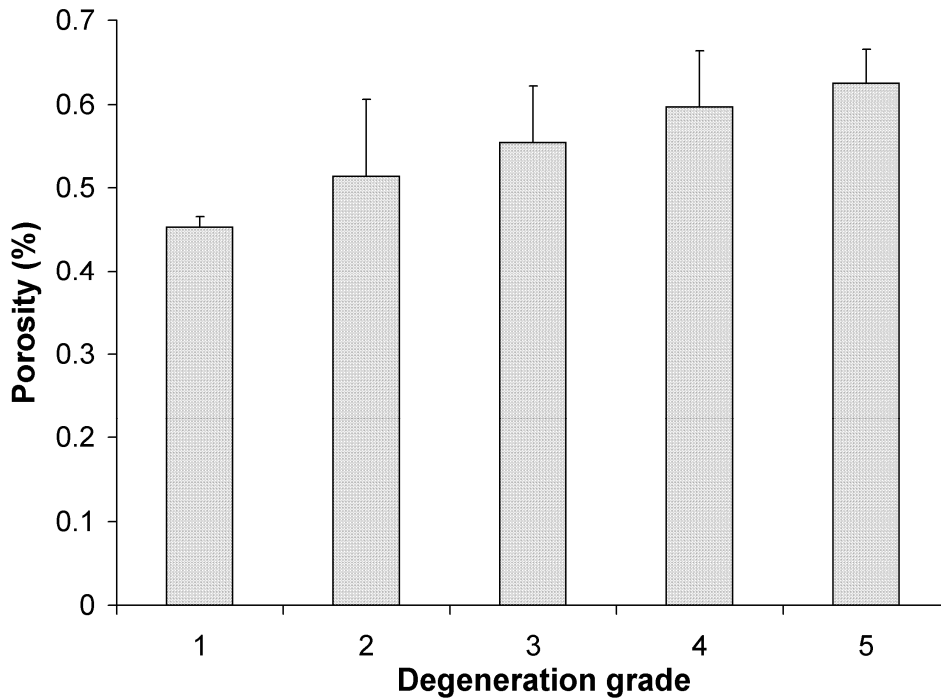


Figure 3.10 The variation of subchondral bone porosity with degeneration ($R^2=0.19$, $p=0.04$). (Significance using post-hoc Tukey test, $*p<0.05$).

Cell density

The mean cell density was 1651 ± 1015 cells/mm³ (Table 3.1). The results of the one way repeated measures ANOVA demonstrated that the three cell density regions were not statistically different. Therefore, the average cell density was used. There was a significant decrement in cell density between grade 1 and 2 discs, then a progressive increase with degeneration grades 2 through 5 (Figure 3.11). When specimen factors were analyzed individually, cell density decreased as disc height increased ($R^2=0.13$ $p<0.02$), but was not directly related to subchondral bone porosity ($p>0.5$), total hydraulic permeability ($p>0.4$), or age ($p>0.2$). A multiple regression model indicated that cell density was inversely correlated to age and disc height ($R^2=0.26$, $p<0.003$).

Table 3.1 Means and standard deviations for outcome variables

Parameter (units)	Sample size	Mean \pm SD
Average cell density (cells/mm ³)	50	1650 \pm 1015
Inferior cell density (cells/mm ³)	50	1529 \pm 1099
Center cell density (cells/mm ³)	50	1731 \pm 1399
Superior cell density (cells/mm ³)	50	1588 \pm 911
GAG content (μ g/mm ³)	50	10.9 \pm 10.6
GAGs/cell (μ g/cell)	50	0.0104 \pm 0.008
Disc height (mm)	51	10.00 \pm 2.31
Total Hydraulic Permeability (m ⁴ /N-s)	50	3.26 \pm 4.43 x 10 ⁻¹⁰
Cartilage Permeability (m ⁴ /N-s)	50	1.19 \pm 1.64 x 10 ⁻¹⁰
Bone permeability (m ⁴ /N-s)	50	22.1 \pm 13.7 x 10 ⁻¹⁰
Subchondral bone porosity	87	0.54 \pm 0.07
Cartilage thickness (mm)	50	1.68 \pm 0.59

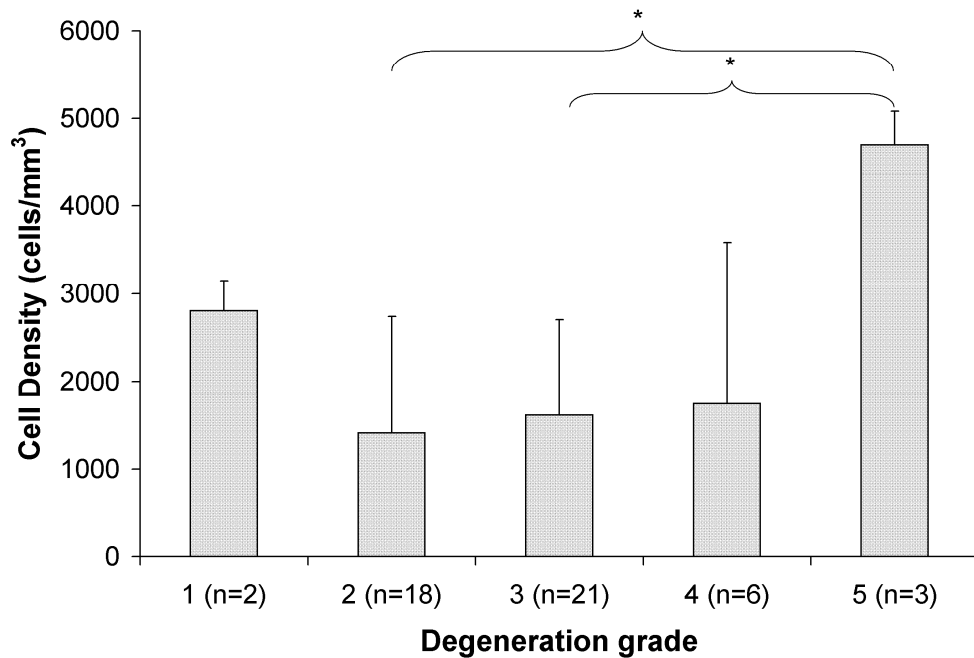


Figure 3.11 The variation of cell density (cells/mm³) with Pfirrmann degeneration grade is presented. Results are shown for mean and standard deviations. (Significance using post-hoc Tukey test, *p<0.05).

GAGs

The results of the one way repeated measures ANOVA demonstrated that the three GAG content regions were not statistically different. Therefore, the average GAG content was used. Average GAG content non-linearly decreased with age ($R^2 = 0.57$, $p < 0.0001$, average $GAG = 296257 * age^{-2.58}$, Figure 3.12) Then average GAG content and Pfirrmann degeneration grade ($R^2 = 0.52$, $p < 0.0001$), with grade 1 significantly higher than grades 2-5, and grade 4 being significantly lower than grades 1 and 2 (Figure 3.13). Endplate porosity decreased as GAG content increased ($R^2 = 0.20$, $p < 0.002$, Figure 3.14). Disc height was non-linearly correlated with average GAG content ($R^2 = 0.20$; $p < 0.001$, Figure 3.15). The multiple regression model for GAG content with age and

cartilage endplate permeability showed that GAG content did not depend on endplate permeability ($p > 0.05$).

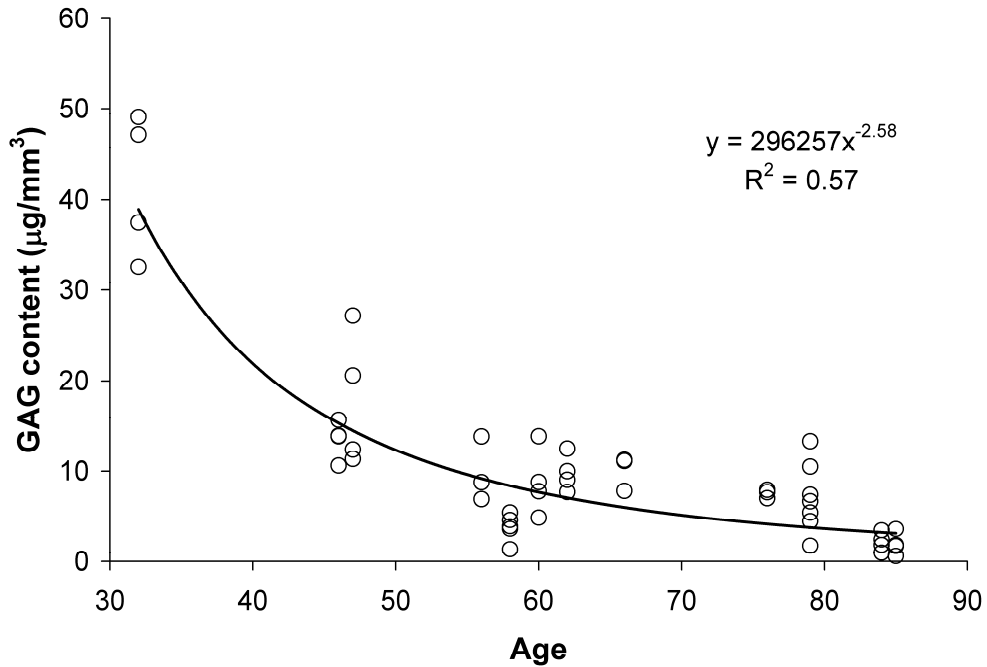


Figure 3.12 The variation of GAG content with age. Data fitted with a power fit equation $\text{GAG} = 296257 \cdot \text{age}^{-2.58}$ ($R^2 = 0.57$, $p < 0.0001$).

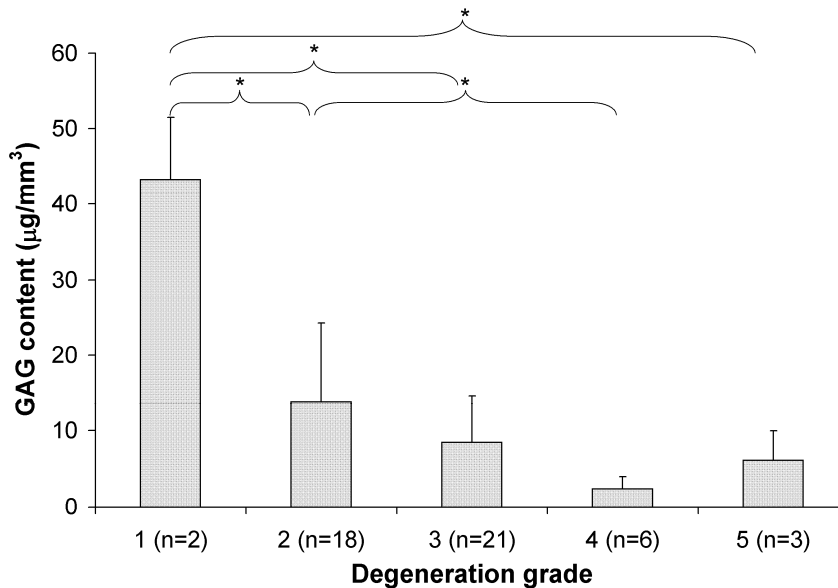


Figure 3.13 The distribution of GAG content with degeneration is shown ($R^2 = 0.52$, $p < 0.0001$). (Significance using post-hoc Tukey test, $*p < 0.05$).

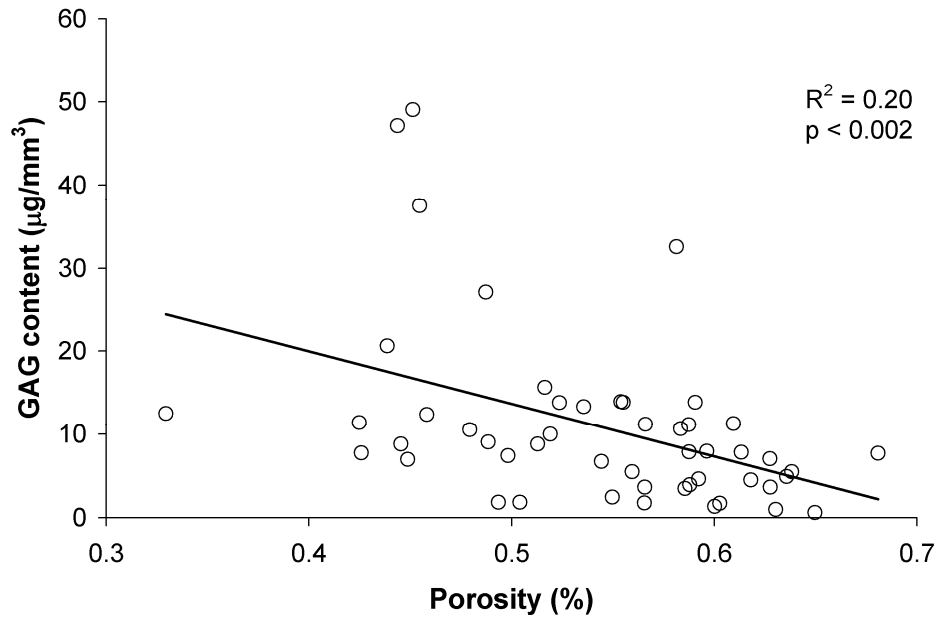


Figure 3.14 Endplate porosity decreased as GAG content increased ($R^2=0.20$, $p<0.002$).

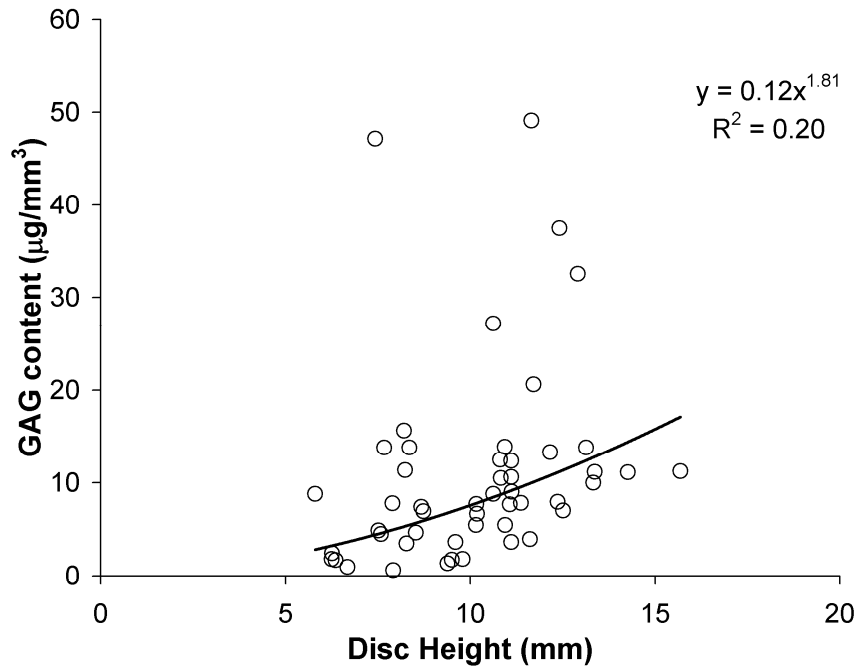


Figure 3.15 The variation of GAG content with disc height. Data fitted with power fit equation $GAG = 0.12 \cdot \text{disc height}^{1.81}$ ($R^2 = 0.20$, $p < 0.001$).

GAGs/cell

GAG content was normalized by cell density as an indirect measure of cell function. Average GAGs/cell decreased with degeneration, with statistically significant differences between grades 1-3 and grade 4-5 ($R^2=0.24$; $p<0.001$; Figure 3.16). GAGs/cell were also weakly correlated with disc height ($R^2=0.29$, $p<0.01$) and age ($R^2=0.23$, $p<0.01$) respectively; Figure 3.17 and Figure 3.18). There was no relationship with hydraulic permeability ($p>0.4$), or porosity ($p>0.07$). When modeled together, disc height and age explained 25% of the variation of GAGs/cell ($p=0.001$).

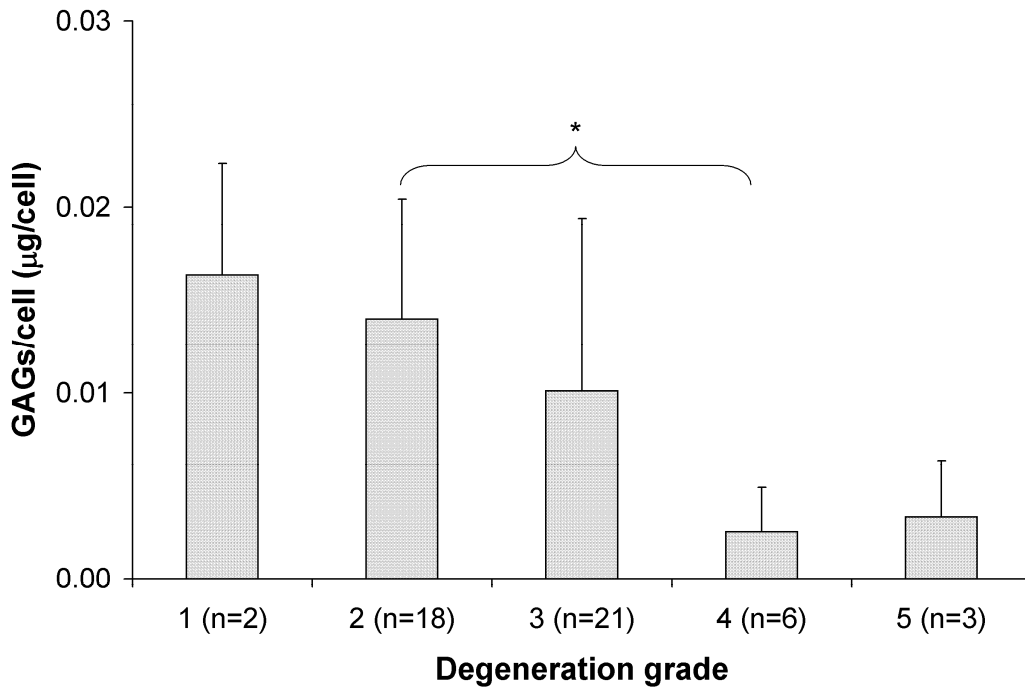


Figure 3.16 The variation of cell function (GAGs/cell) was compared to Pfirrmann degeneration grading ($R^2=0.24$; $p<0.001$). Results are shown for mean and standard deviations. (Significance using post-hoc Tukey test, $*p<0.05$).

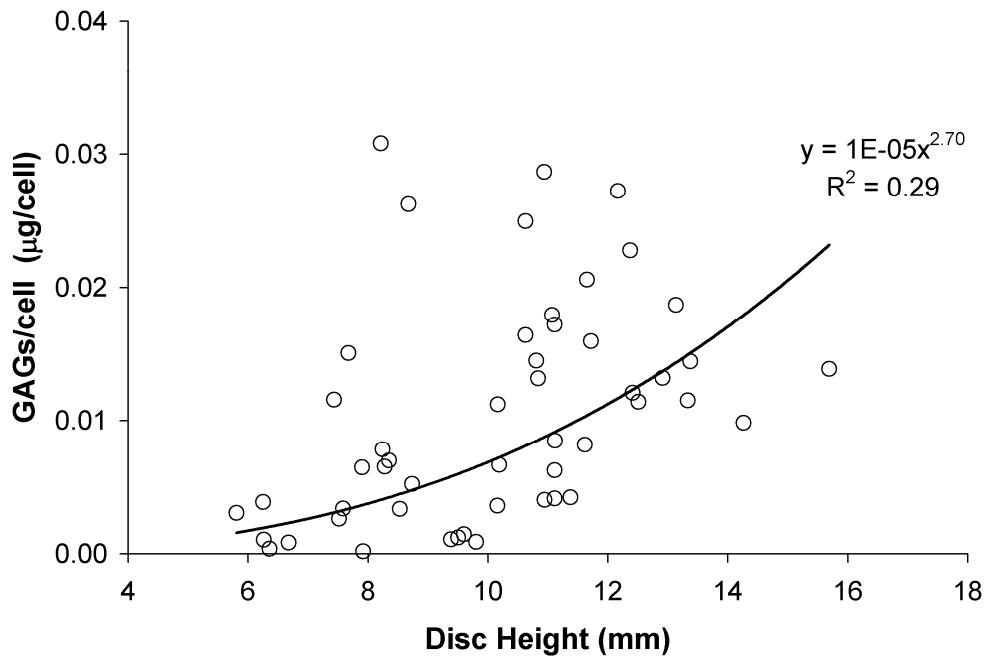


Figure 3.17 GAGs/cell were compared to disc height where $GAGs/cell = 1 \times 10^{-5} * \text{disc height}^{2.70}$ ($R^2 = 0.29$, $p < 0.01$)

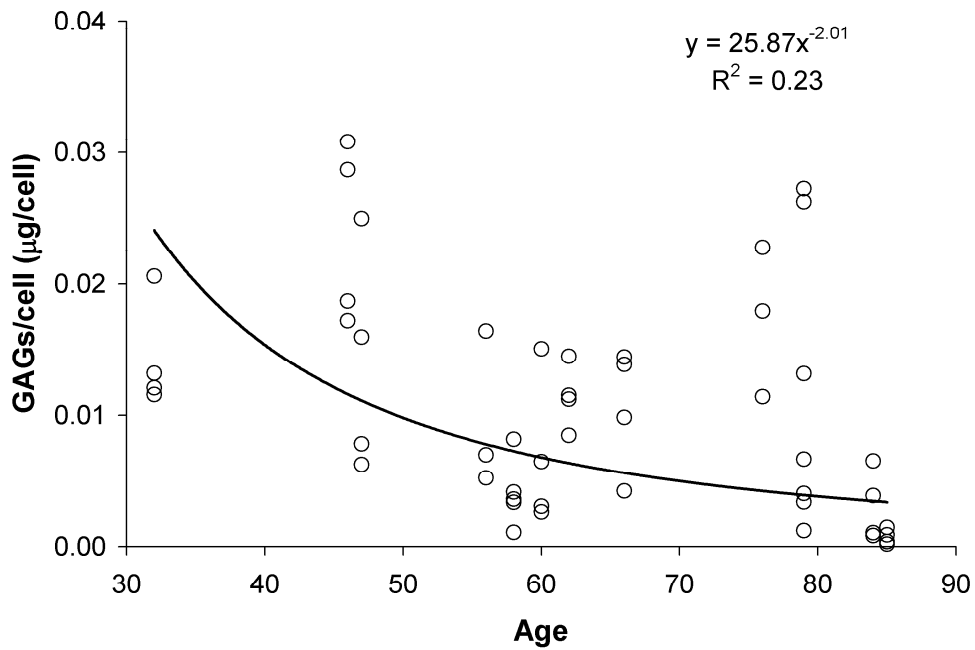


Figure 3.18 The GAGs/cell had a power fit variation with age. $GAGs/cell = 25.87 * \text{age}^{-2.01}$ ($R^2 = 0.23$, $p < 0.01$).

Degeneration

Pfarrmann grade increased with age ($R^2=0.31$, $p=0.002$), with grades 1, 3 & 4 being statistically different (Figure 3.19). Disc height declined with degeneration beyond grade 2 (Figure 3.20). With increasing degeneration, subchondral bone porosity increased ($R^2=0.22$; $p<0.0004$) and disc height decreased: the height of grade 3 discs was less than grade 2, and grade 4 and 5 discs were less than grades 2 and 3 ($R^2=0.57$, $p<0.001$, Figure 3.21).

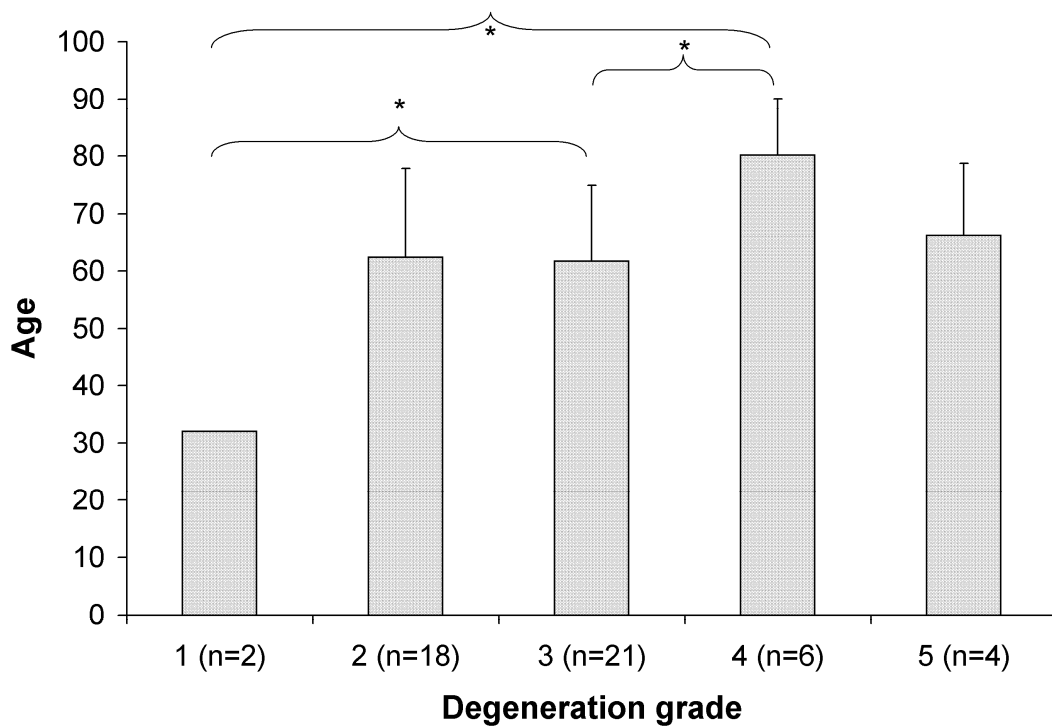


Figure 3.19 Pfirrmann grade increased with age ($R^2=0.31$, $p=0.002$), with grades 1, 3 & 4 being statistically different (Significance using post-hoc Tukey test, $*p<0.05$)

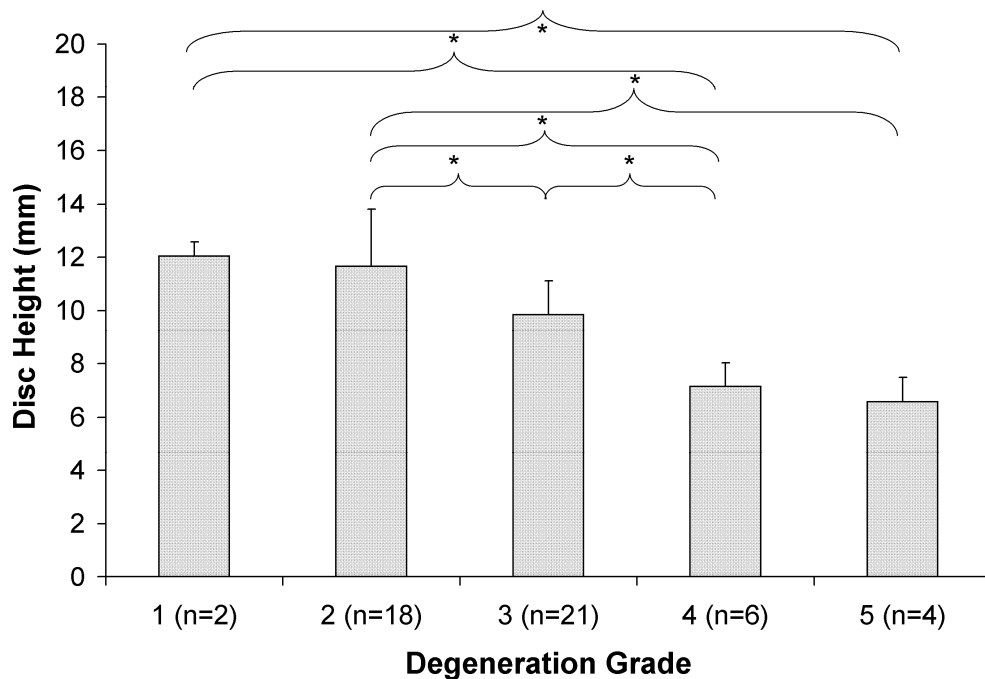


Figure 3.20 The distribution of disc height with degeneration is shown ($R^2=0.57$, $p<0.0001$)

3.4 Discussion

Our goal was to investigate how disc endplate features correlate with disc cellularity and degeneration within the context of our broader objective to learn whether transport limitations can impede disc tissue engineering. We observed that disc cellularity was inversely correlated with disc height, increased with progressive degeneration beyond grade 2, and was unrelated to cartilage endplate permeability or subchondral bone porosity. Although cell density increased with degeneration, cell function indicated by GAGs/cell decreased. Importantly, we noted that total endplate permeability and porosity increase with age and degeneration. Taken together, these results imply that cell dysfunction, rather than physical barriers to transport, accelerates disc disease.

There was also an interesting interplay between age, endplate bone porosity, and GAG content. We observed that endplate porosity increased with age while GAG content

decreased. These opposing trends in porosity and GAG content conflict with reports by Nachemson who made qualitative observations on a smaller sample of endplates and noted a porosity decreased with age and degeneration [7]. More recently, Benneker and coworkers quantified endplate pores in 2 mm thick endplate samples and also reported a decrease in the density of holes (20 to 50 μm range) with increasing degeneration and GAG content, and a variable relationship with age [46]. The discrepancy with our results may be due to their focus on a narrow range of hole sizes, as they noted that overall hole density did not correlate with degeneration because of the presence of large openings that were more apparent with grade 4 and 5 discs. Other authors have reported that increasing GAG content is associated with increased endplate thickness, stiffness, and presumably decreased porosity, and that this may be due to vertebral remodeling to balance increased nuclear osmotic swelling [96-98]. While it is well recognized that GAG content decreases with degeneration [99], these results collectively support our finding that endplate porosity increases with age, and that this may be an adaptive response to a reduction of nuclear swelling pressure.

Permeability has been reported for endplates from several species. Baboon cartilage endplate permeability was measured using confined compression and reported to be $14.3 \times 10^{-14} \text{ m}^4/\text{N}\cdot\text{s}$ cartilage [57]. Accadbled and colleagues measured the hydraulic permeability of intact endplates from growing lambs and pigs that ranged from $1.32 \times 10^{-14} \text{ m}^4/\text{N}\cdot\text{s}$ (lamb) to $3.69 \times 10^{-14} \text{ m}^4/\text{N}\cdot\text{s}$ (pig) [58, 90]. Our total permeability ($3.26 \times 10^{-10} \text{ m}^4/\text{N}\cdot\text{s}$) and cartilage permeability ($1.19 \times 10^{-10} \text{ m}^4/\text{N}\cdot\text{s}$) values were significantly higher, likely due to inhomogeneities and focal cartilage lesions common in degenerated human samples. Conversely, our endplate bone permeability values ($2.21 \pm$

$1.37 \times 10^{-9} \text{ m}^4/\text{N-s}$) are lower than those reported by others for human bone removed from the vertebral centrum ($3.52 \times 10^{-6} \text{ m}^4/\text{N-s}$);[56], This likely is due to the fact that our samples included the bony endplate. Also, based on the comparison results between permeability and vertebral level, we speculate that an increase in permeability from L1 to L5 could be related to an increase in load carried by the lower vertebral levels.

Cell density was inversely related to disc height. This observation is consistent with the well-established concept that diffusive transport (and consequently diffusion distance) is a crucial factor for disc cell viability [27, 100]. Stairmand and coworkers (1991) present an inverse power relationship ($19124 \cdot h^{-0.68}$) between cell density and half-disc height across several species and a large range of disc sizes [76]. Assuming an exponential relationship between cell density and disc height [76] gives Equation 3.3:

$$CD = 16324 \times h^{-1.02} \quad \text{Equation 3.3}$$

where CD is cell density (cells per mm^3), and h is the disc height (mm; $R^2=0.15$, $p=0.005$) (Figure 3.21). Over our narrower range (5.8-15.7 mm), cell density was nearly proportional to height, yet the weak association ($R^2=0.15$) suggests other factors play an important role, such as age that explains another 10% of the variance. Yet, historical reports linking cell density to age have been mixed. Maroudas et al showed that cell density increased with age in the three samples investigated, while Liebscher et al did not find a strong correlation between cell density and age for donors older than 16 years of age [39, 101]. Our results demonstrate that the strong influence of disc height needs to be considered in statistical analyses; otherwise, the strength of other associations may be missed. Discrepancies with historical data may also be differences in cell density analysis

techniques: our average nucleus cell density was approximately 1700 cells/mm³, while others report this to be closer to 4000 cells/mm³ [39, 102]. We estimated cell density by quantification of DNA, while others typically rely on histological methods and extrapolation from two-dimensional images to volumetric estimates.

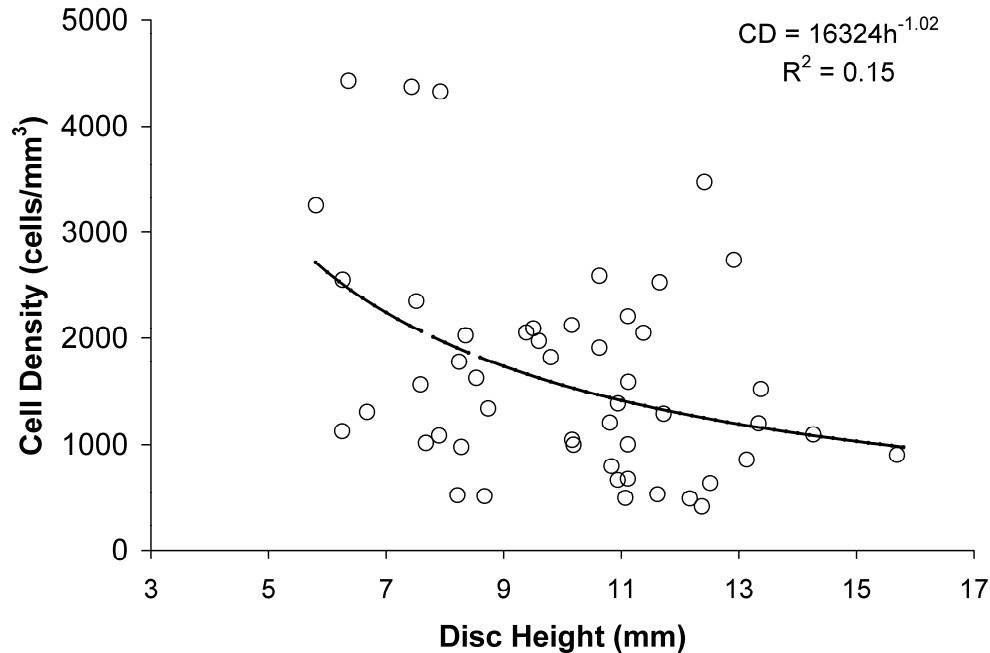


Figure 3.21 The variation of cell density (cells/mm³) with disc height (mm). Data fitted with a non-linear fit equation of the relationship between the two parameters cell density (CD) and disc height (h); $CD = 16324 \times h^{-1.02}$ ($R^2 = 0.15$, $p = 0.005$).

Our report of increasing endplate porosity with degeneration is at odds with a common clinical view that degenerate discs have more sclerotic endplates. For example, subchondral bone sclerosis (and presumably decreased endplate porosity) has been identified as a characteristic of spine osteoarthritis [103], and given the tenuous nature of disc cell nutrition, this sclerosis would negatively impact disc health [18]. Yet, while radiographic evidence of moderate sclerosis is evident in some low back pain patients, no dose-response relationship is apparent [50]. Conversely, some have argued that moderate

osteoporosis would be protective against disc degeneration [47]. However, the clinical data relating osteoporosis to degeneration are mixed [104], with no clear evidence that osteoporosis either protects against or predisposes to degeneration. In a more direct assessment of endplate structure and disc degeneration, Grant and colleagues measured the strength of 77 human endplates using an indentation protocol. They report that endplate strength was correlated with vertebral BMD, and that increasing disc degeneration was associated with an overall loss of endplate strength. Consistent findings were reported by Keller and coworkers [98], who observed a significant negative correlation between endplate stiffness and increasing disc degeneration. Consequently, while vertebral rim density is consistently increased with disc degeneration (i.e. osteophytes), our observations are supported by biomechanical data and indicate that the central endplate becomes more porous with disc degeneration.

Our study is limited because measurements were made on cadaveric tissues and cause-and-effect cannot be directly established. As such, we can only report trends or associations between variables and hypotheses regarding mechanisms are not testable. Equally important, vertebral capillary density was not calculated and therefore the role of nutrition on disc cell density or degeneration cannot be fully clarified. It is well established that many factors, such as smoking, diabetes, atherosclerosis, or steroid use, can decrease vertebral blood flow that, in turn, can impair cell function and accelerate disc degeneration [105-108]. Because these co-morbidities are common in the general population, it is likely that vertebral capillary density varies significantly between individuals and needs to be analyzed in future studies. In this regard, studies using imageable tracers may be particularly valuable [109].

Another protocol limitation was measurement of mobility in the flow-out direction only. Because the cartilage endplate is supported by subchondral bone on one side, the resistance to fluid flow is direction dependent [36, 85]. Here, the flow-out direction was chosen so that test fluid pressure would compact the cartilage endplate analogous to the in vivo situation. Ultimately, disc nutrition is mainly facilitated by movement of small molecules (e.g. glucose) along a concentration gradient (diffusion) rather than fluid flow along a pressure gradient (convection) [18, 110]. Nonetheless, the mobility that characterizes the resistance to solvent flow during convection and the filtration coefficient that quantifies resistance to solute flow during diffusion co-vary since they are both related to tissue pore size[111]. Accordingly, in these experiments it was more important to compact the cartilage endplate so that the tissue pore size corresponded to in vivo conditions rather than quantify direction-dependent mobility.

Successful intervertebral disc tissue engineering requires a stable physicochemical environment [112]. Given this diffusion-limited system, nucleus oxygen is very sensitive to cell density and cell metabolism [76]. Diminished oxygen, in turn, is known to adversely influence disc cell function [113]. Our data suggest that changes in endplate permeability or porosity are not sealing off the disc from vertebral capillaries since permeability and porosity increase with age and degeneration and our mean porosity (54.6%) is far from the theoretical value of 20% suggested by others to provoke disc cell dysfunction [114]. Alternatively, age-related decreases in GAG content and GAGs/cell indicate cellular dysfunction that may be due to senescence [37], or as mentioned above, a poor capillary nutritional source rather than endplate pathology. The majority of current tissue engineering strategies focus on stimulating disc cell matrix synthesis using

growth factors [115], or augmenting the nucleus with rejuvenated cells [116, 117]. Conceptually, these therapies will stress homeostasis and place increased demands on available nutrition routes. For these approaches to be successful therefore, the system needs to have excess capacity to achieve a new steady-state that will sustain increased cell metabolism. This may be the case as transplantation of disc cells and growth factors has begun and shows some clinical benefit in canine models [118, 119].

In summary, our results solidify well-established concepts that disc degeneration is associated with age-related decreases in GAG content and cell activity. The strong influence of disc height on cell density suggests a compensatory mechanism that may help maintain disc cellularity as degeneration progresses. Unexpectedly, endplate hydraulic permeability and porosity were found to increase with age and degeneration. These observations are important both for better understanding degeneration mechanisms but also for evaluating potential risks for regenerative therapies. The preservation of permeability and porosity indicates the disc may not be a ‘coffin’ [120], and implicates other factors as more important for contributing to the degeneration cascade, such as cell senescence or loss of vertebral blood supply.

R ² P value	Average GAGs content (µg/mm ³)	Average GAGs/cell (µg/cell)	Pfirrmann Deg. Scale	Disc Height (mm)	Age	Total Hydraulic Permeability (m ⁴ /N-s)	Bone permeability	Cartilage Permeability	Porosity	Cartilage thickness (mm)
Average cell density (cells/mm ³)	0.10* p<0.02	0.19** p<0.002	0.24* p<0.014	0.13* p<0.02	0.03 p=0.20	0.01 p=0.44	0.06 p=0.1	0.012 p=0.45	0.01 p=0.54	0.01 p=0.52
Average GAGs content (µg/mm ³)		0.22*** p<0.001	0.52*** p<0.0001	0.20*** p<0.001	0.83*** p<0.001	0.05 p=0.16	0.12* p=0.02	0.046 p=0.15	0.20** p<0.002	0.07 p=0.07
Average GAGs/cell (µg/cell)			0.25** p<0.01	0.29** p<0.01	0.14** p<0.01	0.012 p=0.49	0.00 p=0.84	0.05 p=0.31	0.05 P=0.04	0.05 p=0.12
Pfirrmann Deg Scale				0.57*** p<0.001	0.31** p<0.002	0.04 p=0.80	0.066 p=0.53	0.03 p=0.90	0.19* p=0.04	0.01 p=0.38
Disc Height (mm)					0.06 p=0.08	0.00 p=0.90	0.003 P=0.71	0.008 p=0.54	0.01 p=0.65	0.04 p=0.15
Age						0.16** p<0.01	0.10* p=0.03	0.06 p=0.09	0.13** P<0.01	0.08* p=0.03
Total Hydraulic Permeability (m ⁴ /N-s)							0.08 p=0.06	0.96** p<0.0001	0.09* p=0.05	0.05 p=0.129
Bone Permeability								0.05 p=0.13	0.23*** p<0.001	0.014 p=0.41
Cartilage Permeability									0.09* p=0.04	0.007 p=0.58
Porosity										0.05 p=0.13

Significance of correlation *p<0.05, **p<0.01, ***p<0.001

Table 3.2 Correlation coefficients between variables

Chapter 4 Morphology of the vertebral endplate

4.1 Introduction

Previous research has demonstrated age-related macrostructural changes causing endplate thickening [38, 121]. However, subtle changes in bone microstructure may have profound effects on diffusion beyond thickness alone [122, 123]. Important morphological features include bone porosity, trabecular thickness, pore thickness, and pore number [49, 122, 124-126]. Quantitative analysis of these features may provide new insights into the endplate's role in promoting disc degeneration.

Typically, disc degenerative change is quantified using morphological criteria based on clinical images (Pfirrmann grading) or direct visualization of cadaveric samples (Thompson grading). To complement these visual methods, changes in disc cell density and glycosaminoglycan (GAG) content have been used as indicators of pathomechanisms [127]. With age and degeneration, it is well known that proteoglycans degrade [9], while cell density fluctuates [37, 128]. Therefore, disc GAG content and cell density are quantitative indices with which to investigate the potential degenerative influence of endplate bony morphology.

In the previous chapter, we studied the relative roles of cartilage endplate and vertebral endplate permeability in disc degeneration. The results indicated that bone permeability at the surface had a statistically significant relationship with porosity at the surface. Also, bone porosity increased with disc degeneration. These associations indicate that additional relationships between permeability and bone morphology may be present. By exploring the relationships between the permeabilities obtained in the previous

chapter and the bone characteristics investigated in this chapter, we would add to our understanding of bone morphology and disc degeneration.

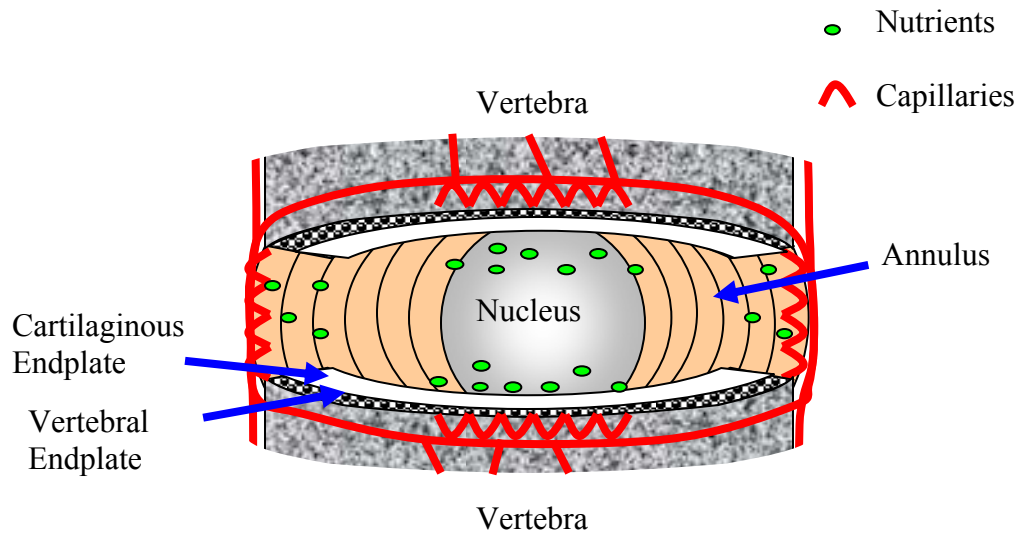


Figure 4.1 Diagram of a motion segment, comprised of an inferior vertebra, an adjacent disc and a superior vertebra. The endplate structure is composed of the vertebral endplate and the cartilaginous endplate. Capillaries are located in the center of the vertebra and on the periphery. Nutrients travel from the capillaries through the endplate structure to the nucleus pulposus.

We hypothesized that changes in endplate microstructure alter nutrient diffusion, and thereby contribute to disc degeneration. To test this, we examined the relationship between several measures of bone microstructure (bone porosity, trabecular thickness, pore thickness, and pore number) and three disc degeneration indices: Pfirrmann grade, cell density and GAG content. The effect of age on VEP morphology was also examined. Finally, we studied the relationship between the VEP regional morphology and permeability.

4.2 Materials and Methods

Fourteen cadaveric lumbar spines L1-L4 (4) or L1-L5 (10) were obtained from donor banks (4 female and 10 male donors; mean age 64 ± 16 yrs, age range 35-85). The spines were scanned in a 3T MRI Scanner (GE Healthcare, Milwaukee, WI), and graded (1-5) by 3 trained radiologists using the Pfirrmann degeneration scale [55]. Next, the surrounding soft tissue and posterior elements were removed from the spines using a bone saw (Exakt Model, Band Saw, Norderstedt, Germany). Fifty-one motion segments were then cut transversely using a bone saw to obtain specimens consisting of half vertebra/disc/half vertebra. While frozen to preserve nuclear tissue, cores were obtained from the center of the motion segments by using an 8.25 mm diamond coring tool (Starlite Industries, Rosemont, PA) (Figure 4.2). Each motion segment core was composed of the inferior vertebral endplate cranial to the disc, the intervertebral disc nuclear tissue and the superior vertebral endplate caudal to the disc, producing a total number of 102 vertebral cores after the nuclear tissue was removed as detailed in Chapter 3.

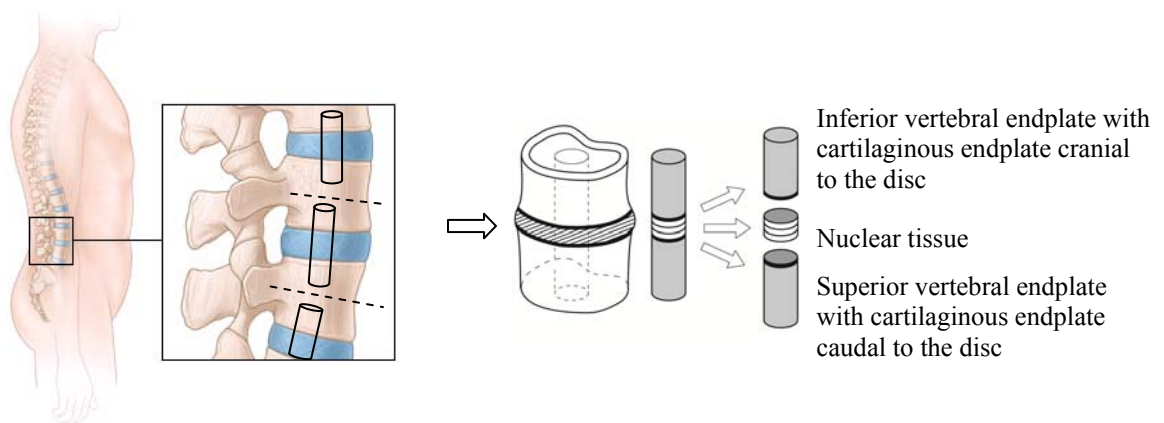


Figure 4.2 Diagram of a motion segment dissection. Each motion segment core was composed of the inferior vertebral endplate cranial to the disc, the intervertebral nuclear tissue and the superior vertebral endplate caudal to the disc.

Imaging

The vertebral bone cores were thawed and imaged in a commercial micro-computed tomography system (μ CT 40, Scanco Medical, Brüttisellen, Switzerland) with an X-ray tube voltage of 70 kV and 180° acquisition. Each core was placed in a cylindrical sample holder in a bath of protease inhibitors diluted 1:10 with distilled water (P2714 Protease inhibitor cocktail, Sigma-Aldrich, St Louis MO) to keep the cartilage in the specimens from degrading [57]. A spatial resolution with an isotropic voxel size of 8 μ m (matrix 2048 x 2048, 1000 projections/180°, FOV 16.4 mm) was chosen. Specimens were scanned along the length of each core, encompassing the vertebral endplate surface and 3 mm of bone underneath it. Image cross sections were restored to a 3D structure using the manufacturers' cone beam reconstruction algorithm [60] and then each 3D structure was transformed into 1000-1100 serial 8 μ m thick sliced images in a sagittal orientation. Next, a light Gaussian filter (to remove high frequency noise) followed by a fixed threshold (to binarize the images into a bone and pore phase) was applied to each sagittal slice [64]. The irregular vertebral endplate surface was then identified using a custom-made algorithm developed using MATLAB software. The semiautomatic technique is fully described elsewhere [87].

Four bone microstructural indices, pore fraction, PF ($1-BV/TV[\%]$, where BV is bone volume and TV is tissue volume), trabecular thickness (TbTh [mm]), pore diameter (PoD [mm]) and pore number (PoN [1/mm]) were calculated using a 2D distance transformation method [129](Figure 4.3). The distance transformation method calculates the distance of every bone/voxel (object) to the nearest bone/air (background) surface. The distances were visualized as the radius of a sphere with a center in the voxel that fits

inside each bone structure. Then, the redundant spheres were removed and the largest spheres confined the smaller spheres. This resulted in the mid axes of the maximal spheres filling the structure completely [129]. To calculate pore fraction (porosity), data from the binarized images mentioned above was used to calculate the fraction of pore volume per tissue volume or $(1-BV/TV)$. Next, to calculate TbTh, each trabecula attained the value of the radius of the maximal sphere contained in the trabecular bone. Then, the mean value of the diameter (twice the radius) was assigned as the TbTh. The calculation of PoD followed the same procedure except each voxel in the background (air) was fitted with a maximal sphere instead of the bone. Then, the distance between the spheres' mid axes was calculated and the inverse was taken to provide the number of pores per mm, PoN.

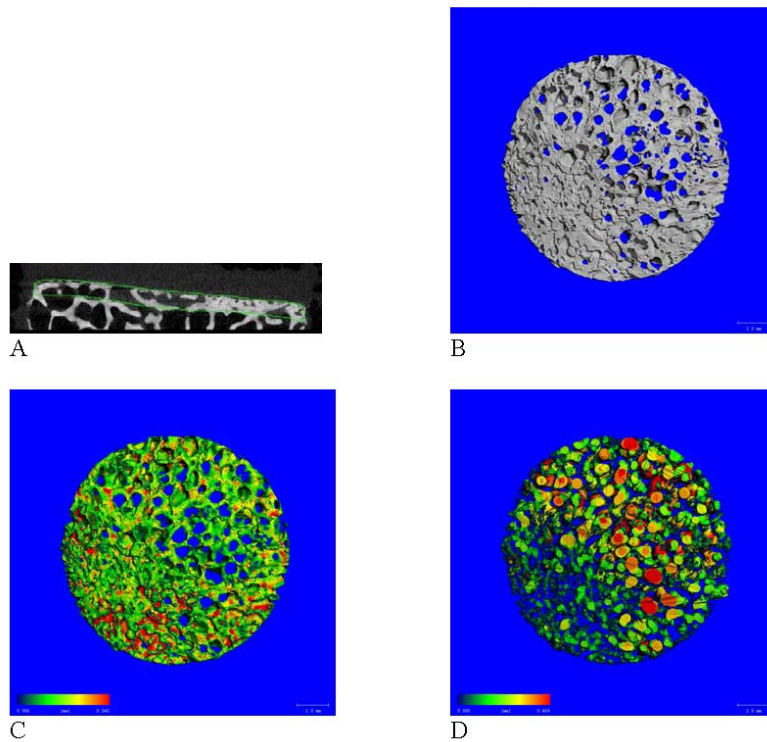


Figure 4.3 (A) MicroCT sagittal view of VEP thickness region on one slice. 2D view from top for (B) Porosity – The gray color highlights the bone and blue background highlights the open pores (C) Trabecular thickness – The red areas highlight the thickest trabeculae. (D) Pore Diameter – The red areas highlight the largest pores.

In order to compare morphological changes in different regions of the vertebral endplate, four specific regions of interest (ROIs) were selected for morphological analysis. A diagram of the vertebral core highlighting the location of the VEP region can be seen in Figure 4.4 along with a plot of the average bone volume fraction variation in a 2 mm depth region (Figure 4.4). The definition of the four ROIs is as follows (Figure 4.5). First, for each sagittal μ CT image, the surface endplate was identified as an ROI selecting the subchondral endplate contour that included a 16 μ m (two pixels) thick region. The next region highlighted the maximum bone density and it was identified as the most-dense region within the 2 mm region with a two pixels thick delineation. The third region selected encompassed the full endplate thickness of each individual slice,

which was defined as the distance from the surface contour to the point of maximum bone density for each individual slice within each 2 mm ROI. This region was identified as the vertebral endplate thickness (VEP Th). Lastly, in order to select the full vertebral endplate encompassing donors from varying ages, a 2 mm thickness region was selected. The surface contour was shifted in the axial direction to a 2 mm depth away from the surface, generating a 2 mm ROI. This thickness was also used in previous studies [130].

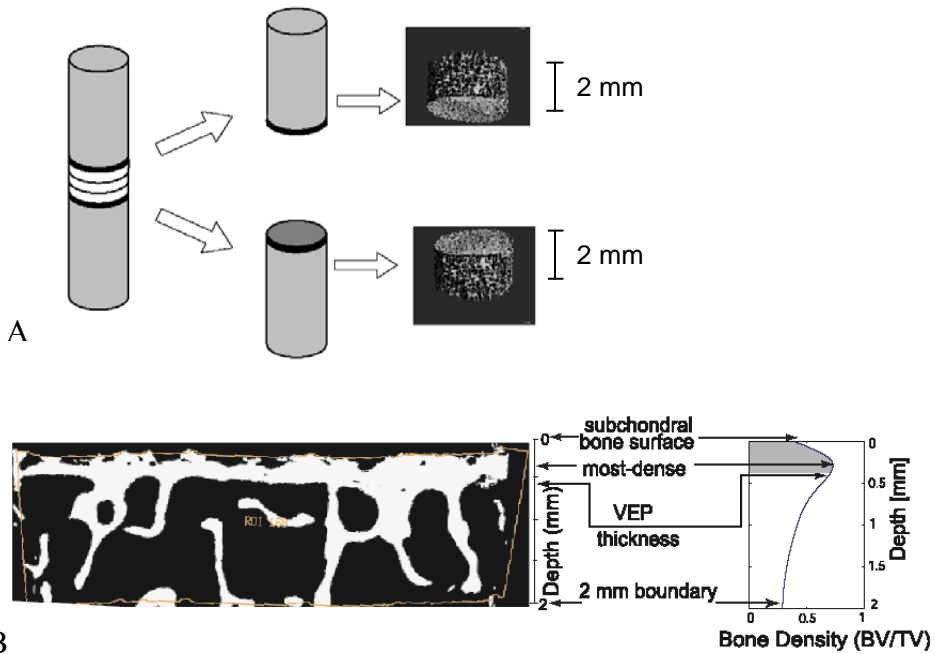


Figure 4.4 A. (From left to right). The diagram shows the cylindrical core obtained from the vertebral motion segment. It is followed by a 3D MicroCT image of the two individual vertebral cores highlighting the location of the 2 mm regions. From the surface, a 2 mm thick region was selected. B. A sagittal binarized image of a subchondral bone section with a 2 mm ROI was selected (bottom left). A plot of the bone volume fraction (BV/TV) variation through the 2 mm depth is shown on the right. The location of the four ROIs analyzed was matched visually with the sagittal image on the left (bottom right).

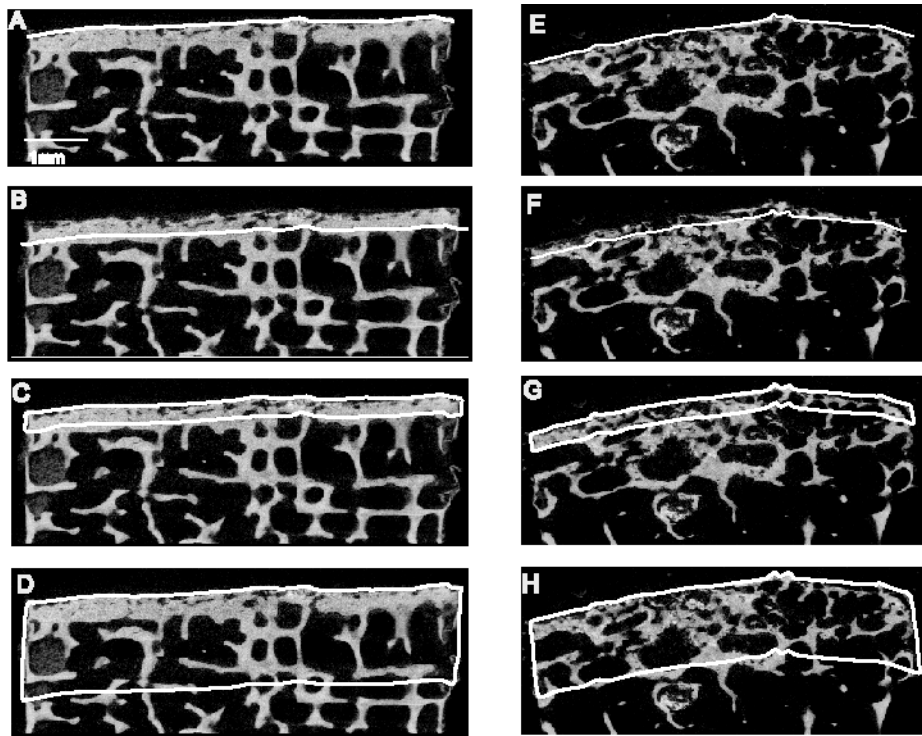


Figure 4.5 MicroCT binarized sagittal sections from two specimens. The left column shows ROIs for a vertebral core next to a healthy disc and the right shows a vertebral core next to degenerated disc. A & E highlight the ‘surface’ region; B & F highlight the ‘most dense’ region. C & G highlight the ‘VEP thickness’ region and D & H highlight the ‘2 mm’ region.

Total, bone and cartilage permeability measurements of the bone cores were obtained. The methods to acquire and calculate permeability were described in Chapter 3. The thickness of the cartilage endplate removed was measured using a contact micrometer.

The biochemical analyses for the nuclear tissue included cell density and GAG content. As detailed in the previous chapter, the nuclear tissue was separated in three parts to determine the difference in cell density within the disc. Since it was found that no statistically significant difference was present between the three parts of the nuclear tissue (Chapter 3), the average cell density was used.

Finally, each sample was inspected for the presence of a double layer endplate (Figure 4.12). A subset from the main dataset indicating the double layer feature was used to further analyze the samples. This subset of specimens was used to correlate the bone indices with degeneration grade, age, cell density, GAG content and the 3 types of permeability.

Statistical analyses were performed using a commercial statistical software package (JMP v5.0, SAS Institute, Inc., Cary, NC). Analysis of variance (ANOVA) procedures were used to calculate group means and to test for differences in the microstructural indices between bone regions. When indicated, a *post-hoc* Tukey was performed. Regression analyses were also performed to estimate the effects of the structural bone indices at each of the four ROIs on degeneration grade, age, cell density, GAG content, total permeability, bone permeability and cartilage permeability. Also, an ANOVA was used to compare vertebral endplate thickness with degeneration grade. The differences in vertebral endplate thickness were compared for the inferior and superior cores using a student t-test.

4.3 Results

Six cores were excluded from the main dataset due to severe, degeneration-related inhomogeneities at the surface that could not be analyzed in a semiautomatic fashion. The 2 mm region had the highest porosity (69%) followed by the surface (54%), the most-dense region (43%) and the VEP Th (43%) (Table 4.1). PoN was highest at the surface and lowest at the 2 mm region.

Structural Bone Indices	Regions	Mean	Standard Deviation
PF	Surface	54%	8
	Most Dense	43%	16
	VEP Th	44%	14
	2 mm	69%	9
TbTh	Surface	0.10 mm	0.02
	Most Dense	0.21 mm	0.06
	VEP Th	0.18 mm	0.05
	2 mm	0.17 mm	0.04
PoD	Surface	0.19 mm	0.09
	Most Dense	0.33 mm	0.08
	VEP Th	0.24 mm	0.08
	2 mm	0.53 mm	0.12
PoN	Surface	6.24/mm	1.12
	Most Dense	4.36/mm	1.46
	VEP Th	4.27/mm	0.69
	2 mm	2.88/mm	0.52

Table 4.1 The mean and standard deviations for each structural index in all four regions.

Porosity variation with degeneration (Figure 4.6A, Figure 4.7)

The 2 mm region was more porous than the other three regions when the comparison was performed for only grade 1 (Figure 4.6A). The same comparison performed for only grade 5 at the surface region showed this porosity trend disappeared and the four regions had similar porosity (Figure 4.6A). Porosity increased with degeneration at three out of the four regions (Figure 4.7).

Trabecular thickness variation with degeneration (Figure 4.6B, Figure 4.8)

Trabecular thickness had statistically significant differences with degeneration at the most dense and the VEP thickness regions ($p < 0.05$; Figure 4.8). The surface region had the thinnest trabeculae, and thinning increased with degeneration at the most dense and the VEP Th regions. The most dense region contained the thickest trabeculae for

grade 1 samples (Figure 4.6B). The trabecular thickness at the most dense and VEP thickness region for grade 1 was approximately twice as thick as the trabeculae at the surface. This large difference decreased in the grade 5 samples.

Pore diameter variation with degeneration (Figure 4.6C, Figure 4.9)

All the regions except for the 2 mm region had some statistically significant differences with degeneration grade (Figure 4.9). At grade 1, the smallest pore diameter was located at the vertebral surface region, but at grade 5, the differences in pore diameter were not discernable (Figure 4.6C).

Pore number variation with degeneration (Figure 4.6D, Figure 4.10)

Overall, the surface region and the most dense region had statistically significant differences with degeneration grade (Figure 4.10). The first four degeneration grades showed statistically significant differences between the regions (Figure 4.6D). These differences in pore number were not observed in the four regions at grade 5.

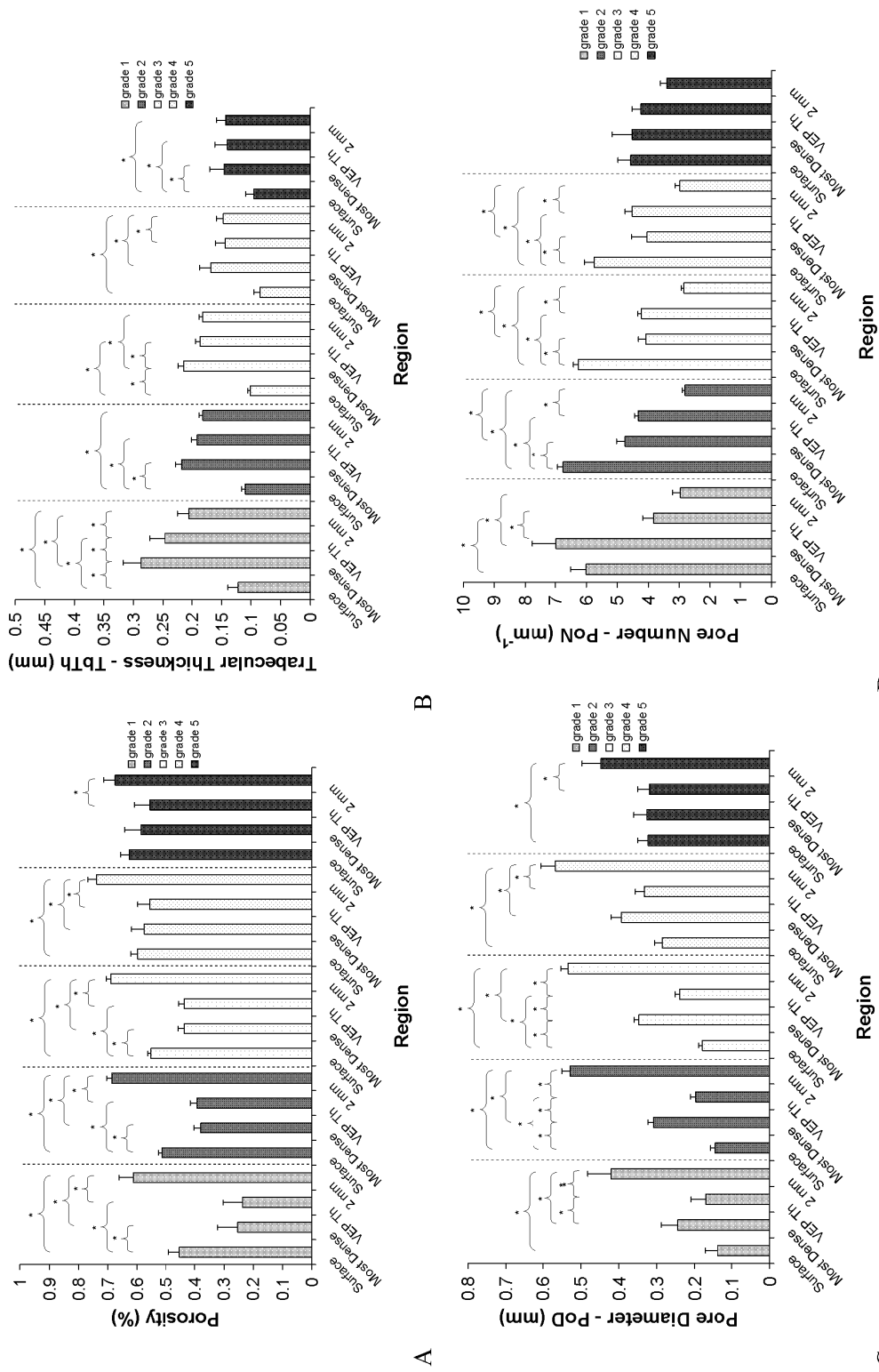


Figure 4.6 ANOVAs comparing changes in each bone index with the four regions within each degeneration grade. Porosity (A), trabecular thickness (B), Pore diameter (C) and Pore number (D). * = statistically significant difference (p<0.05)

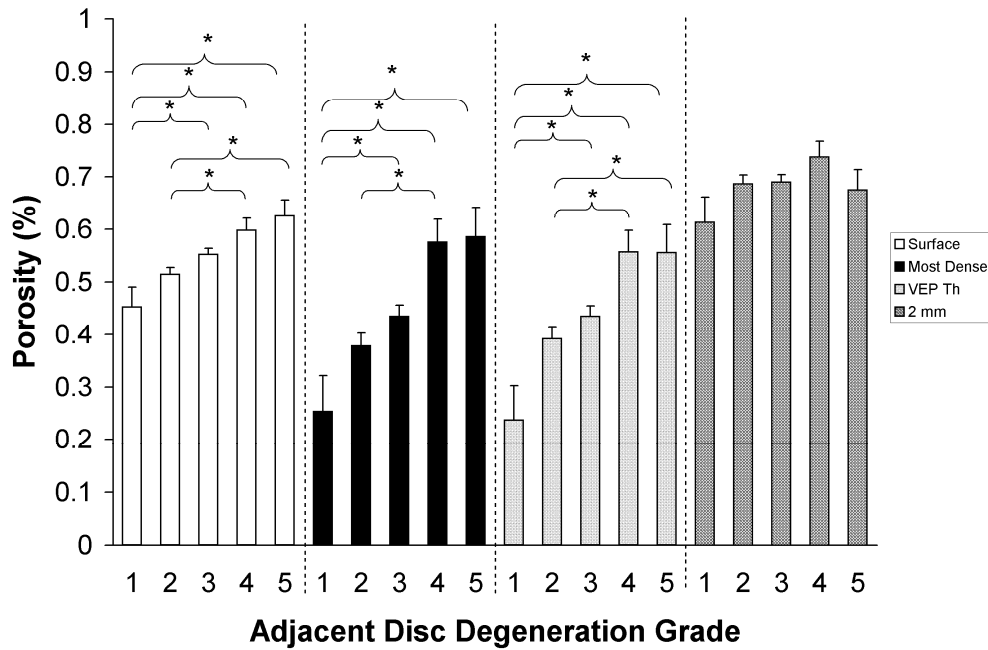


Figure 4.7 Porosity variations with degeneration over the four regions. * = statistically significant difference ($p < 0.05$).

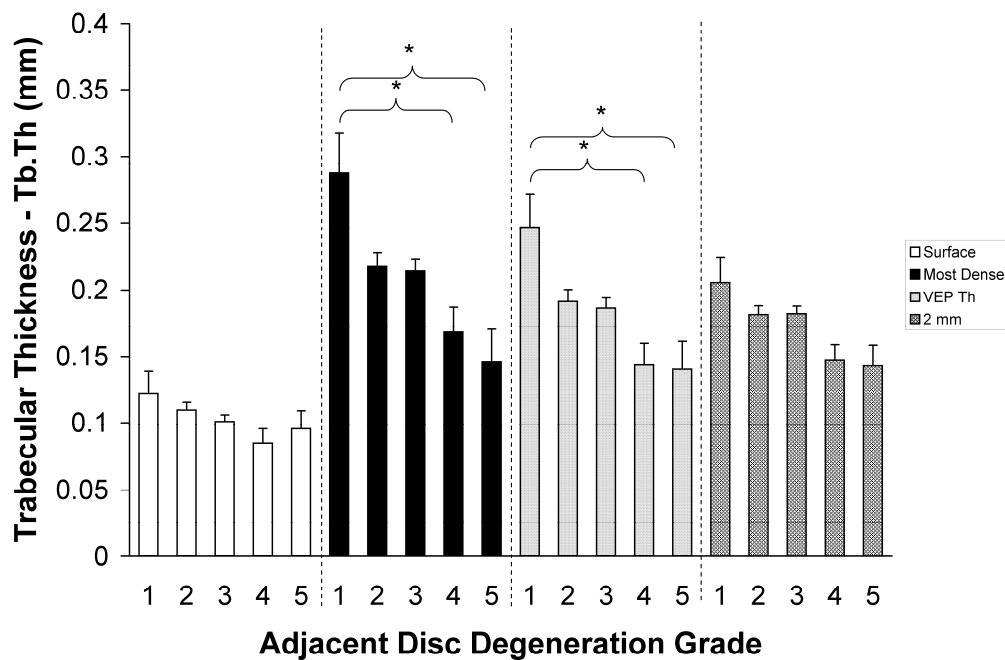


Figure 4.8 Trabecular thickness variations with degeneration over the 4 regions. * = statistically significant difference ($p < 0.05$).

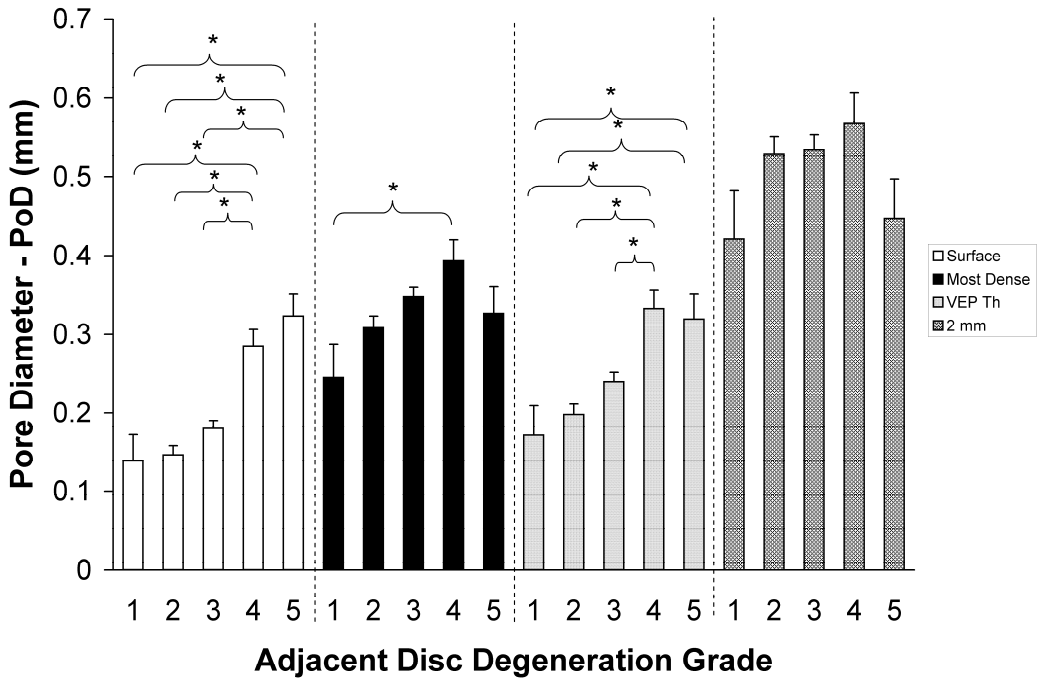


Figure 4.9 Pore diameter variations with degeneration over the 4 regions. * = statistically significant difference ($p < 0.05$).

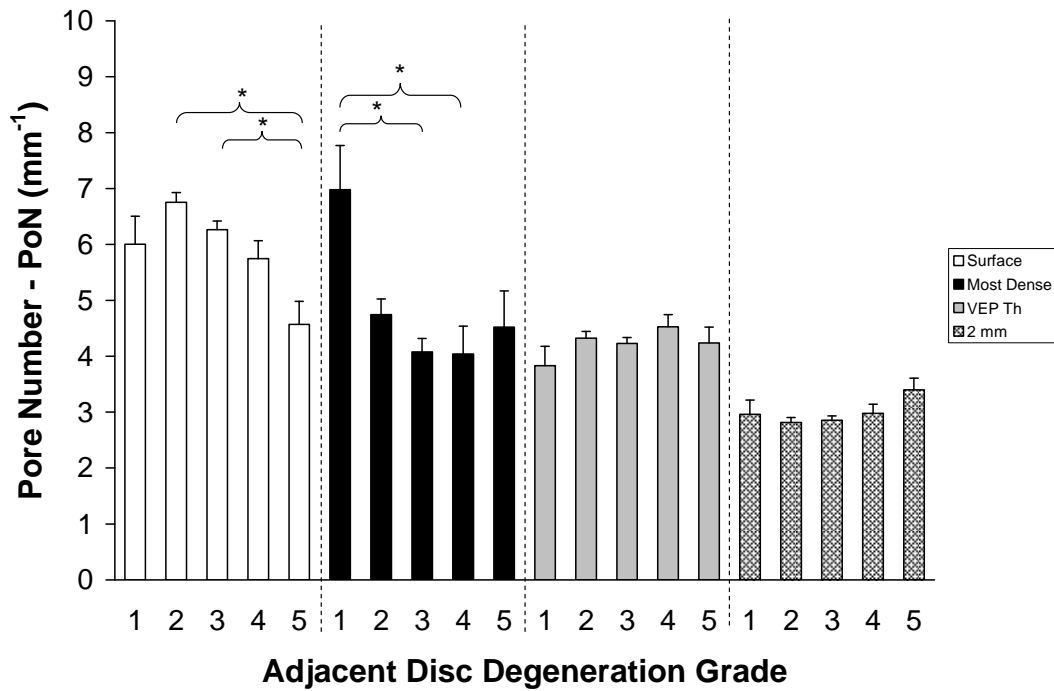


Figure 4.10 Pore number variations with degeneration over the 4 regions. * = statistically significant difference ($p < 0.05$).

Structural bone indices variation with age, GAGs and cell density (Table 4.2)

GAG content decreased as age increased, while pore fraction and pore diameter increased (Table 4.2). In addition, as age increased, trabecular thickness and pore number decreased. No statistically significant differences in the bone indices with cell density were present, except for pore number at the surface and the most dense regions. Overall, the structural bone indices followed consistent trends in all 4 regions, except for PoN.

Structural Bone Index	Regions	Trend	Age		Trend	GAG		Trend	Cell Density	
			R ²	*		R ²	*		R ²	*
PF	Surface	↑	0.14	*	↓	0.16	*	↓	0.02	
	Most Dense	↑	0.18	*	↓	0.23	*	↓	0.02	
	VEP Th	↑	0.28	*	↓	0.28	*	↓	0.03	
	2 mm	↑	0.39	*	↓	0.23	*	↓	0.03	
TbTh	Surface	↓	0.11	*	↑	0.14	*	↑	0.04	
	Most Dense	↓	0.21	*	↑	0.22	*	↑	0.03	
	VEP Th	↓	0.22	*	↑	0.23	*	↑	0.03	
	2 mm	↓	0.20	*	↑	0.14	*	↑	0.03	
PoD	Surface	↑	0.07	*	↓	0.08	*	↑	0.03	
	Most Dense	↑	0.16	*	↓	0.19	*	→	0.00	
	VEP Th	↑	0.15	*	↓	0.16	*	→	0.00	
	2 mm	↑	0.35	*	↓	0.20	*	↑	0.02	
PoN	Surface	→	0.00		→	0.00		↓	0.13	*
	Most Dense	↓	0.20	*	↑	0.25	*	↑	0.08	*
	VEP Th	↑	0.06	*	↑	0.04		↓	0.07	
	2 mm	↓	0.07	*	↑	0.05		→	0.00	

Table 4.2 Correlations of structural bone indices with age, GAGs and cell density for each of the four regions. * = statistically significant difference (p<0.05). (↑) increasing trend, (↓) decreasing trend and (→) no relationship. The arrows indicate the trend that age, GAGs or cell density (dependent variables) follow with bone index (independent variable).

Permeability

The total, cartilage and bone permeability tended to increase with an increase in porosity and with a decrease in trabecular thickness in the four regions (Table 4.3). Consistent trends were not observed between the three permeabilities and pore diameter and pore number at the four regions. With an increase pore diameter, bone permeability increased, for two of the four bone indices. There were statistically significant trends with total and cartilage permeability in at least one region for all indices, except for PoD.

Structural Bone Index	Regions	Trend	Total Permeability		Trend	Bone Permeability		Trend	Cartilage Permeability
			R ²	*		R ²	*		R ²
PF	Surface	↑	0.08	*	↑	0.19	*	↑	0.04
	Most Dense	↑	0.10	*	↑	0.17	*	↑	0.03
	VEP Th	↑	0.08		↑	0.27	*	↑	0.02
	2 mm	↑	0.04		↑	0.15	*	↑	0.02
TbTh	Surface	↓	0.17	*	↓	0.06		↓	0.14 *
	Most Dense	↓	0.12	*	↓	0.17	*	↓	0.06
	VEP Th	↓	0.15	*	↓	0.15	*	↓	0.09
	2 mm	↓	0.19	*	↓	0.10	*	↓	0.11 *
PoD	Surface	→	0.00		↑	0.13	*	→	0.00
	Most Dense	→	0.01		↑	0.02		→	0.00
	VEP Th	→	0.01		↑	0.20	*	→	0.00
	2 mm	→	0.00		↑	0.06		→	0.00
PoN	Surface	↑	0.03		↓	0.05		↑	0.05
	Most Dense	↓	0.02		↓	0.07		↓	0.02
	VEP Th	↑	0.15	*	→	0.01		↑	0.13 *
	2 mm	↑	0.03		↓	0.02		↑	0.02

Table 4.3 Correlations of structural bone indices with total permeability, bone permeability and cartilage permeability for each of the four regions. * = statistically significant difference (p<0.05). (↑) increasing trend, (↓) decreasing trend and (→) no relationship. The arrows indicate the trend that total, bone or cartilage permeability (dependent variables) follows with bone index (independent variable).

Additional Observations

Figure 4.11 The vertebral endplate thickness decreased with degeneration beyond degeneration grade 2, but the differences were not statistically significant (Figure 4.11). The average VEP thickness was 0.45 ± 0.32 mm and the range of VEP thickness varied from 0.05-1.84 mm. In addition, the difference between the inferior and superior vertebral endplate thickness was not statistically significant, ($p=0.34$). The VEP thickness variation was compared with vertebral level and no statistically significant differences were found, ($p=0.09$).

The majority of the observed double layers were located adjacent to degenerated discs grade 2 or 3. Twenty-two vertebral cores out of the main dataset showed this feature. The majority of the double layer vertebral endplate specimens were observed from three donors in both superior and inferior vertebral bodies of the L1-L5 levels including 13 IVDs, 16 vertebral cores out of 27 possible vertebral cores showed this feature (Figure 4.12). These three donors were males in the 49-84 years age range. The rest of the specimens came from different donors. Few statistically significant correlations between bone indices were observed for double-layer endplates (Table 4.4). For example with an increase in age, porosity increased and trabecular thickness decreased for some of the regions. Also, cell density increased with an increase in porosity at the VEP thickness and the 2 mm region. GAG content decreased as porosity and pore diameter increased. The correlations with permeability were inconsistent, the majority of the correlations occurred at the 2 mm regions for total permeability. Two correlations were present with bone permeability and one with cartilage permeability.

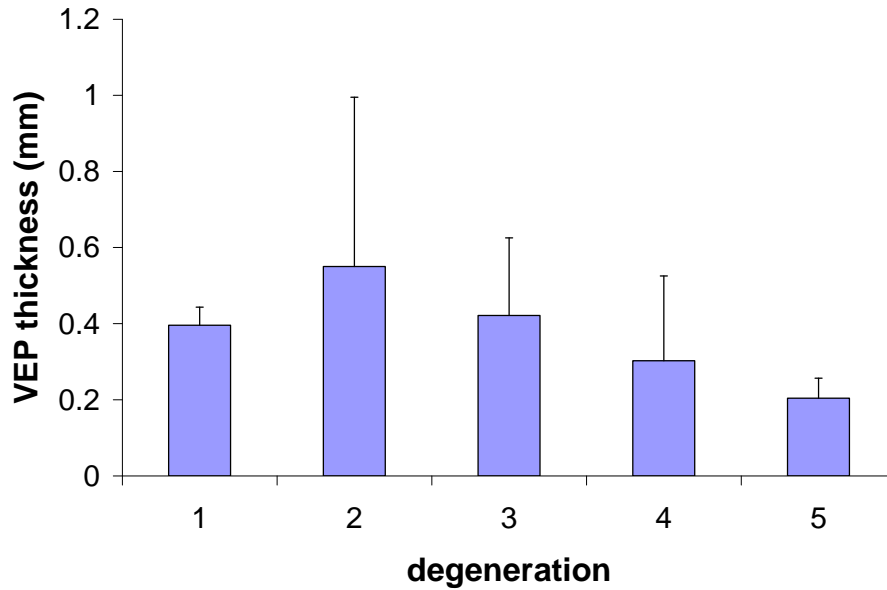


Figure 4.11 The results for the VEP thickness with degeneration for the complete dataset including the double layer samples are shown. No statistical significance was observed in vertebral thickness with degeneration grades.

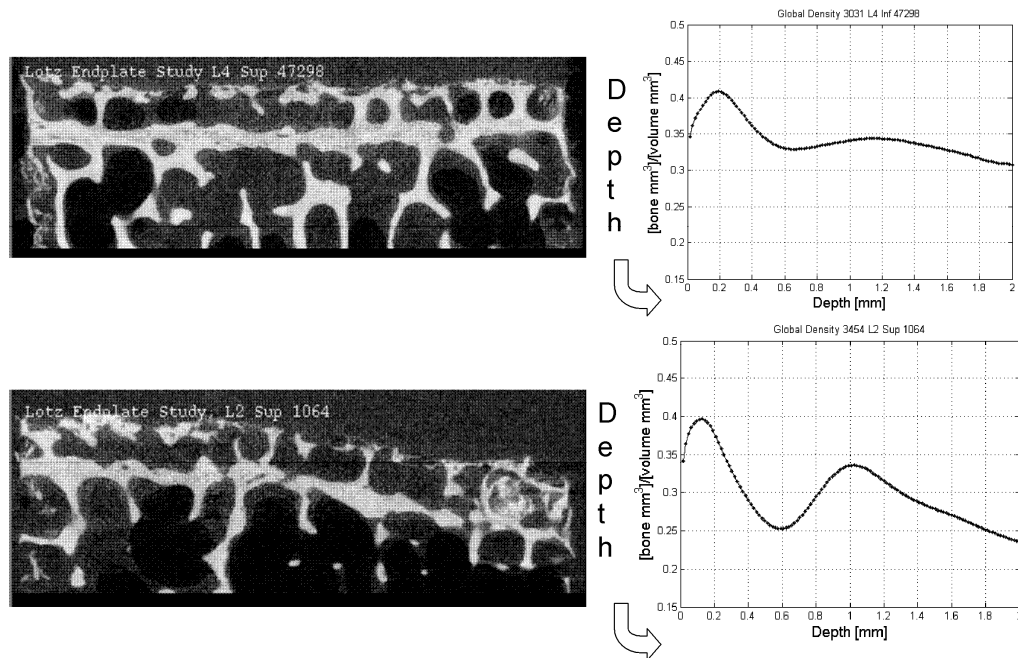


Figure 4.12 Sagittal slices of two samples that showed a double layer vertebral endplate (left). The matching bone fraction distribution per depth is presented (right). On the top left, level L4 superior vertebral endplate is shown and on the bottom left, level L2 superior vertebral endplate is shown. Each sample's distribution of bone fraction vs. depth plot is shown on the right. The double layer endplate can be seen in the plots on the right as showing two separate peaks.

Structural Bone Index	Regions	Trend	Age	Trend	Cell Density	Trend	GAG	Trend	Total Permeability	Trend	Bone Permeability	Trend	Cartilage Permeability
			R ²		R ²		R ²		R ²		R ²		R ²
PF	Surface	↑	0.20 *	↑	0.18	↓	0.00	→	0.07	↑	0.02	↓	0.19
	Most Dense	↑	0.04	↑	0.04	↓	0.00	→	0.00	→	0.00	↓	0.21
	VEP Th	↑	0.38 *	↑	0.20 *	↓	0.01	↓	0.40	→	0.00	↓	0.65 *
	2 mm	↑	0.22 *	↑	0.29 *	↓	0.34 *	↓	0.79 *	↑	0.15	↓	0.18
TbTh	Surface	↓	0.27 *	↓	0.03	↓	0.16	↓	0.01	↑	0.57 *	→	0.01
	Most Dense	↓	0.20 *	↓	0.20 *	↑	0.03	↑	0.15	↑	0.12	↑	0.14
	VEP Th	↓	0.13	↓	0.21 *	↑	0.07	↑	0.12	↑	0.26	↑	0.06
	2 mm	↓	0.11	↓	0.19	↑	0.09	↑	0.57 *	↑	0.13	→	0.00
PoD	Surface	↑	0.14	↑	0.15	↓	0.28 *	↓	0.40	↑	0.07	↓	0.33
	Most Dense	↑	0.01	↑	0.01	↑	0.04	→	0.04	↑	0.07	↓	0.12
	VEP Th	↑	0.13	↑	0.01	→	0.02	→	0.02	↑	0.06	↓	0.40
	2 mm	↑	0.07	↑	0.21	↓	0.49 *	↓	0.50 *	↑	0.53 *	↓	0.25
PoN	Surface	↓	0.03	↓	0.08	↑	0.48 *	↑	0.31	↓	0.16	↑	0.30
	Most Dense	–	0.03	↓	0.02	↓	0.08	↓	0.02	↓	0.23	↓	0.00
	VEP Th	–	0.00	–	0.00	↑	0.02	→	0.00	↓	0.24	↑	0.11
	2 mm	–	0.00	↓	0.11	↑	0.60 *	↑	0.33	↓	0.35	↑	0.11

Table 4.4 Double layer specimens-correlations of structural bone indices with age, cell density, GAG content, total permeability, bone permeability and cartilage permeability for each of the four regions. * = statistically significant difference (p<0.05). (↑) increasing trend, (↓) decreasing trend and (→) no relationship. The arrow indicate the trend that age, GAGs, cell density total, bone or cartilage permeability (dependent variables) follow with bone index (independent variable).

4.4 Discussion

We hypothesized that changes in endplate microstructure would correlate with disc degeneration. Our data demonstrate significant depth-dependent changes in bone morphology, with the peak density occurring at approximately 0.29 ± 0.20 mm below the endplate surface. However, this heterogeneity decreased with increasing disc degeneration. Morphological features correlated with two of the three adjacent disc degeneration indicators (Pfirrmann grade and GAG content) as well as with age and

permeability. In general, the endplate became thinner and more porous with age and degeneration.

The VEP changes from a heterogeneous structure to a homogeneous structure as the adjacent disc degenerates. This indicates that while bone loss occurs throughout the VEP with an increased age, density is lost predominantly in the most-dense region. Adjacent to grade 1 discs, porosity, trabecular thickness and pore diameter were lowest in the surface region. This difference disappeared for endplates adjacent to grade 5 discs. Therefore, changes occurring to the denser regions are more pronounced, manifested as a higher rate, than the surface and the 2 mm regions (Figure 4.13). The loss of endplate heterogeneity is consistent with prior reports that vertebral bone structure is more heterogeneous in young human lumbar vertebrae than in older ones [126]. Overall, bone loss lead to an increased surface porosity indicating that sclerosis does not block the surface adjacent to endplate cartilage leading to an increase in degeneration as others had hypothesized [37, 131]. Also, it was previously believed that sclerosis blocked disc nutrition to the intervertebral disc, but based on this study results we can see that this does not occur in the central region. It has been reported that sclerosis has a higher likelihood to appear in the periphery of the vertebra [48], but the periphery does not interfere with the main nutrient diffusion path at the central endplate.

With increasing age, GAG content decreased and Pfirrmann grade increased as expected, but unexpectedly VEP porosity increased. This increasing porosity with age is at odds with prior reports [41], and suggests that endplate sclerosis is not a dominant factor in accelerating degenerative change via reduced nutrient transport [37, 41, 131].

This perspective is more consistent with recent data for the central endplate region [52, 132].

Nucleus cell density was not correlated with any of the endplate morphological indices. This observation further refutes the notion that endplates become more sclerotic with age, compromised disc cell nutrition, and thereby promote degenerative change. We have previously demonstrated that disc cell density is more strongly correlated with disc height, and tends to increase with the later stages of degeneration when discs collapse due to GAG loss. Yet, though disc cell density tends to increase, these cells become less synthetically active which may be due to senescence or other factors such as changes in the osmotic environment or the presence of inflammatory factors [128].

Though we did not observe a correlation between endplate sclerosis and degeneration, a lack of nutrient availability may still be an important degenerative factor. Previous studies noted that vascularity decreases with age [7, 8, 133] and another study reported a lack of vascularization beyond the fourth year of life (Boos, Weissbach et al. 2002). Further investigation of cell function and the capillaries content in the vertebral endplate could provide useful information about their relationship to disc degeneration.

Another mechanism that might exacerbate the disc degeneration cascade was suggested by supporting work by Roughley. Roughley speculated that proteoglycans degrade and break down into smaller molecules with an increase in age and a decrease in nutrients. Since porosity increases with disc degeneration, GAGs might be escaping the VEP with more ease. This decline in GAG content observed with an increase in porosity was supported by our previous results where GAG content decreased and porosity increased with age and degeneration (see chapter 3 and Rodriguez, 2010). The degraded

proteoglycans (GAGs) contribute to disc swelling pressure and function as long as they remain entrapped within the center of the disc by an intact outer annulus fibrosus and endplate structure [9]. Therefore, if the VEP is disrupted with bone loss, an increase in porosity could provide an open door for GAGs to migrate out as the disc degenerates and ages.

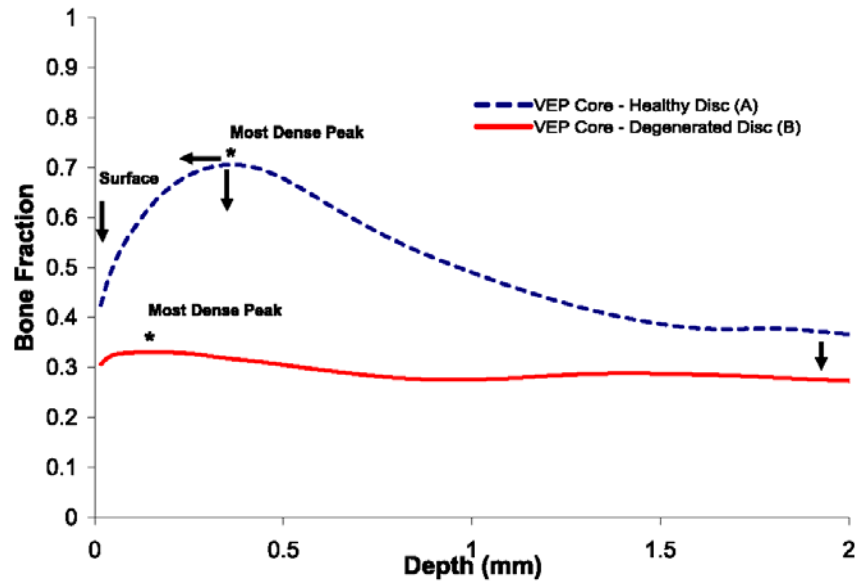


Figure 4.13 Degeneration changes from two representative vertebral cores: (A) adjacent to a healthy disc and (B) adjacent to a degenerative disc, are illustrated showing a bone fraction variation in 2 mm depth. As the disc adjacent to a vertebral endplate became more degenerated (sample B). The most dense peak moved closer to the surface and the bone fraction decreased with degeneration. The quantity of trabeculae below the transitional zone (most dense peak) also decreased as the disc became more degenerated.

In accordance with previous studies, we observed a decrease in endplate thickness with degeneration [38, 96]. A double endplate structure, noted by others, was also detected in a subset of our samples [121]. This feature was observed only on vertebral cores adjacent to Pfirrmann grade 2 and 3 discs, which might suggest that this is a transient feature that is lost as the endplate surface subsides with degeneration. Interestingly, the majority of the double layer features were observed in male donors, supporting the suggestion of different bone distributions occurring in males and females

[134]. When double-layered samples were analyzed separately, disc cell density increased with an increase in porosity and it decreased as trabecular thickness increased. These two trends are opposite to the trends observed in the full dataset, and suggest that the double layer increase in bone density might represent a sclerotic change. This relationship could be further explored in future studies with a larger amount of samples.

The majority of studies characterizing vertebral bone density focus on osteoporotic fracture risk as opposed to adjacent disc health [48]. The current study is one of few that compares the morphological changes of the vertebral endplate with adjacent disc degeneration in the central region [96]. We used a high spatial resolution MicroCT to study the morphology at the level of individual trabeculae within the vertebra. The semiautomatic selection method chose predetermined regions in a systematic fashion. The focus on the microscale provides more details about the changes occurring in the VEP with degeneration. A study limitation is the focus on the central endplate and consequently, the results may not be applicable to the vertebral rim. Another limitation is the nature of cadaveric studies that preclude conclusions regarding cause-and-effect. As a result, we can only speculate about the potential mechanisms driving the bone morphology changes and adjacent disc degeneration.

Our results suggest that measures of endplate morphology may add value to current regimens that rate degenerative status. Currently, pain level and disc degeneration grades are used for assessment of appropriate interventions which may require surgery [135]. Additional degeneration information based on the VEP morphology could potentially increase the accuracy of the degeneration assessment. While MicroCT is

inappropriate for human use because of the high radiation dose, the results may be translated to clinical devices such as DXA and MRIs using registration techniques [65].

Overall, this study provides new information regarding endplate morphology, its changes with age, and its potential role in disc degeneration. The increase in bone porosity in the vertebral endplate with Pfirrmann grade, GAG content, and age suggests that nutrient diffusion is not interrupted by endplate sclerosis. Rather it suggests that the potential barriers to disc nutrition could be driven by changes in either cell function or capillary density. Future studies may explore whether a reduction in capillary density at the VEP reduces the vertebral blood supply of nutrients available to the disc leading to disc degeneration.

Chapter 5 Conclusions and Future Directions

5.1 Research Summary

The goal of this dissertation was to advance the understanding of disc degeneration by studying the relationship between endplate permeability, vertebral endplate morphological changes and disc degeneration parameters. The findings established that bone permeability, VEP porosity (a sclerosis indicator) and cell density increased and GAG content decreased with disc degeneration. An additional observation was the change in VEP morphology from a heterogeneous to a homogenous structure with advanced disc degeneration. Contrary to previous studies[45, 50], our results found that the VEP becomes more porous with advanced disc degeneration. These results imply that disc degeneration might arise from changes in either the cell's ability to absorb the nutrients, the number of available capillaries or the functioning of the capillaries. The combination of these results in the disc and the bone leads us to conclude that physical barriers do not inhibit the transport of nutrients.

Chapter 2 presented the design, construction and validation of a permeameter device. The permeability of the device was validated using porous metal discs within the expected range of bone and cartilage tissue (10^{-9} to 10^{-11} m²/Pa-s). After obtaining undesired results on the first generation permeameter device, the device was successfully modified and then validated. To our knowledge, no study has measured the permeabilities of both bone and cartilage with the same permeameter device.

The permeameter described in chapter 2 was used to measure the permeability of human cadaveric endplate samples in chapter 3. This study focused on the central human vertebral endplate region, specifically on the permeabilities of the CEP, the VEP and the

combined CEP and VEP structure. No one has previously examined all three structures from the same specimen, nor have correlations between the permeabilities and degeneration been reported. The disc degeneration parameters measured were disc degeneration grade, disc height, GAG content, cell density and subchondral bone porosity. A statistically significant inverse relationship between GAG content and cartilage permeability was observed, but no relationship was found with cartilage permeability. We observed a decrease in disc height, which explained the cell density increase with disc degeneration. Since no significant correlations were observed between cartilage permeability and disc degeneration, and since porosity was linearly correlated to permeability at the VEP surface, we concluded that cell dysfunction and/or a reduction of capillaries providing nutrients to the disc might be driving disc degeneration.

In chapter 3, we focused most of our attention on the intervertebral disc. Since nutrition in the disc is driven by changes in both the disc and the vertebra, chapter 4 focused more on the vertebra by exploring the microstructural changes occurring in the vertebral endplate with degeneration. In this study, a semiautomatic algorithm was developed to measure the microstructure of the vertebral endplate. Previous studies selected regions of interest using manual methods based on histology images, which were prone to errors and difficult to replicate. This study offered an easily reproducible selection method, which was therefore more robust. A major finding of this chapter was the morphological change in the VEP from a heterogenous to a homogenous structure as disc degeneration advanced. The results indicated that the VEP became more porous with degeneration, while GAG content decreased with disc degeneration. We concluded that

GAG content is dependent on vertebral physical changes and that sclerosis at the endplate may not be blocking the disc as was previously hypothesized[41, 46].

5.2 Future Directions

Our results indicated that nutrients were not blocked by sclerosis at the endplate. Since there is no sclerosis at the endplate in advanced disc degeneration, molecules might be escaping the disc. However, there is no current information regarding the relationship between pore size and the ability of molecules of different sizes to diffuse through the endplate. A future study could focus on nutrient diffusion of individual molecules crossing the endplate to the disc. Human cadaveric endplate samples similar to our specimens could be used to determine how different size molecules could diffuse in and out of the disc. For example, molecules of different sizes could be forced through the endplate at physiologic pressures and the concentration quantified before and after they cross the disc. The purpose of this study would be to advance knowledge of the role that the cartilage endplate plays in sieving different molecules as disc degeneration increases.

This dissertation did not correlate bone mineral density (BMD) from our samples at the microstructural level with disc degeneration. We inferred osteoporosis in our specimens by comparing our specimens' bone structural indices at the microscopic level to osteoporotic characteristics, such as high bone porosity and bone thinning at the macroscopic level. Typically, osteoporosis and osteopenia (a precursor to osteoporosis) are diagnosed clinically by using DXA, which quantifies BMD at the macrostructural level. A previous study investigating the relationship between osteoporosis and disc degeneration concluded that clinically obtained BMD values from the vertebra do not directly correlate with disc degeneration[52]. Further studies assessing the BMD at the

microstructural level could elucidate information about the relationship between BMD and bone structural parameters at the microscopic level with disc degeneration. A study could be performed on human cadaveric vertebrae that have either osteoporosis or osteopenia, where the BMD would be obtained at the macrostructural level using DXA. Then, measurements of BMD and bone structural indices, such as porosity and bone thickness, from the central region of the vertebrae, where the most disc nutrition to the disc diffuses, would be obtained at the microstructural level using MicroCT. These values would be compared to disc degeneration parameters. Overall, this study would clarify the role of BMD and bone structural indices with disc degeneration at the microstructural level and give some insights about disc degeneration not provided by the macroscopic level clinical BMD values.

Our results also established a linear relationship between disc degeneration and bone porosity and bone permeability. In this study, a one-dimensional Darcy's law equation was used to quantify permeability. This simple equation was used to obtain fundamental information about the relationship between permeability and disc degeneration. However this simple equation did not take into account the complex bone structure, which might explain the difference in values in our bone permeability compared to past studies [36, 57]. A future study using a higher order Darcy's law equation could potentially improve accuracy by incorporating a complex factor such as tortuosity. The tortuosity factor would measure the movement of liquid through the bone's tortuous path. By incorporating this factor, this equation could provide more accurate permeability values.

Our observations also provided a good foundation for future, time controlled studies. The results in chapter 3 and 4 indicated that vertebral sclerosis was not present. This indicates that other factors might be affecting disc degeneration. One of these factors could be capillary reduction in the VEP. In order to investigate the role of capillaries in disc degeneration, a study could be performed on an animal model in which nutrition would be blocked to create disc degeneration. This study would focus on *in vivo* imaging of the flow of nutrients through the capillaries to the endplate and into the disc. The animal disc would be analyzed under two conditions: first on a normal disc, and then on a disc in whose adjacent capillaries are blocked to create a nutrient deficit on the disc. This study would determine the relationship of nutrient reduction to disc health.

Based on our results we concluded that another factor that could affect disc degeneration is cell dysfunction. The symptoms of cell dysfunction could range from a reduction in the maintenance of the ECM to an increase in apoptosis or senescence. An *in vitro* study, using animal cells from a young and old population, relative to the animal's age, could be exposed to a harsh environment, similar to the one experienced in degenerated discs. Then, the cells' function would be analyzed by using a DMMB assay to measure proteoglycan production and a viability assay to assess the cell's health. If a reduction in ECM is observed, indicated by low DMMB values, this would identify a need to stimulate cell matrix synthesis. This could be performed by adding growth factors, which could be introduced in a subsequent study followed by an analysis of the changes assessed with the same assays mentioned above. On the other hand, if the results indicate mostly cell death, then the cell matrix could be regenerated by inserting young cells into the disc, as has been done before in animal studies [116, 117]. The changes

would then be analyzed with the same assays mentioned above to look for differences in disc health. These studies would provide basic information supporting tissue-engineering techniques aiming to regenerate degenerated human discs in the near future.

Overall, the information obtained in this proposed studies would be useful to further advance disc degeneration knowledge.

References

- [1] G. B. Andersson, "Epidemiology of low back pain," *Acta Orthop Scand Suppl*, vol. 281, pp. 28-31, 1998.
- [2] B. I. Martin, R. A. Deyo, S. K. Mirza, J. A. Turner, B. A. Comstock, W. Hollingworth, and S. D. Sullivan, "Expenditures and health status among adults with back and neck problems," *Jama*, vol. 299, pp. 656-64, 2008.
- [3] A. J. Freemont, A. Watkins, C. Le Maitre, M. Jeziorska, and J. A. Hoyland, "Current understanding of cellular and molecular events in intervertebral disc degeneration: implications for therapy," *J Pathol*, vol. 196, pp. 374-9, 2002.
- [4] J. A. Buckwalter, "Spine Update: Aging and degeneration of the Human Intervertebral Disc," *Spine*, vol. 20, pp. 1307-1314, 1995.
- [5] A. G. Nerlich, E. D. Schleicher, and N. Boos, "1997 Volvo Award winner in basic science studies. Immunohistologic markers for age-related changes of human lumbar intervertebral discs," *Spine*, vol. 22, pp. 2781-95, 1997.
- [6] T. Videman and M. C. Battie, "The influence of occupation on lumbar degeneration," *Spine (Phila Pa 1976)*, vol. 24, pp. 1164-8, 1999.
- [7] A. Nachemson, T. Lewin, A. Maroudas, and M. A. Freeman, "In vitro diffusion of dye through the end-plates and the annulus fibrosus of human lumbar intervertebral discs," *Acta Orthop Scand*, vol. 41, pp. 589-607, 1970.
- [8] N. Boos, S. Weissbach, H. Rohrbach, C. Weiler, K. F. Spratt, and A. G. Nerlich, "Classification of age-related changes in lumbar intervertebral discs: 2002 Volvo Award in basic science," *Spine*, vol. 27, pp. 2631-44, 2002.

- [9] P. J. Roughley, "Biology of intervertebral disc aging and degeneration: involvement of the extracellular matrix," *Spine (Phila Pa 1976)*, vol. 29, pp. 2691-9, 2004.
- [10] B. Vernon-Roberts and C. J. Pirie, "Degenerative changes in the intervertebral discs of the lumbar spine and their sequelae," *Rheumatol Rehabil*, vol. 16, pp. 13-21, 1977.
- [11] S. Roberts, "Disc morphology in health and disease," *Biochem Soc Trans*, vol. 30, pp. 864-9, 2002.
- [12] S. R. Bibby, D. A. Jones, R. B. Lee, J. Yu, and J. P. G. Urban, "The pathophysiology of the intervertebral disc," *Joint Bone Spine*, vol. 68, pp. 537-42, 2001.
- [13] S. Roberts, J. Menage, and J. P. Urban, "Biochemical and structural properties of the cartilage end-plate and its relation to the intervertebral disc," *Spine*, vol. 14, pp. 166-74, 1989.
- [14] K. B. Broberg, "On the mechanical behaviour of intervertebral discs," *Spine (Phila Pa 1976)*, vol. 8, pp. 151-65, 1983.
- [15] T. Aigner, S. Soder, P. M. Gebhard, A. McAlinden, and J. Haag, "Mechanisms of disease: role of chondrocytes in the pathogenesis of osteoarthritis--structure, chaos and senescence," *Nat Clin Pract Rheumatol*, vol. 3, pp. 391-9, 2007.
- [16] M. A. Adams and P. J. Roughley, "What is intervertebral disc degeneration, and what causes it?," *Spine*, vol. 31, pp. 2151-61, 2006.
- [17] R. J. Moore, "The vertebral endplate: disc degeneration, disc regeneration," *Eur Spine J*, vol. 15 Suppl 3, pp. S333-7, 2006.

- [18] J. P. Urban, S. Smith, and J. C. Fairbank, "Nutrition of the intervertebral disc," *Spine*, vol. 29, pp. 2700-9, 2004.
- [19] S. K. Eswaran, A. Gupta, M. F. Adams, and T. M. Keaveny, "Cortical and trabecular load sharing in the human vertebral body," *J Bone Miner Res*, vol. 21, pp. 307-14, 2006.
- [20] Prakash, L. V. Prabhu, V. V. Saralaya, M. M. Pai, A. V. Ranade, G. Singh, and S. Madhyastha, "Vertebral body integrity: a review of various anatomical factors involved in the lumbar region," *Osteoporos Int*, vol. 18, pp. 891-903, 2007.
- [21] B. Clarke, "Normal bone anatomy and physiology," *Clin J Am Soc Nephrol*, vol. 3 Suppl 3, pp. S131-9, 2008.
- [22] T. Hildebrand and P. Ruegsegger, "Quantification of Bone Microarchitecture with the Structure Model Index," *Comput Methods Biomech Biomed Engin*, vol. 1, pp. 15-23, 1997.
- [23] J. DeLisa and W. C. Stolov, "Handbook of Severe Disability," in *Significant Body Systems*, W. C. Stolov and M. R. Clowers, Eds.: Department of Education, Rehabilitation Services Administration, 1981, pp. 30-36.
- [24] D. Lajeunesse, F. Massicotte, J.-P. Pelletier, and J. Martel-Pelletier, "Subchondral bone sclerosis in osteoarthritis: not just an innocent bystander," *Modern Rheumatology*, 2003.
- [25] N. M. Grosland and V. K. Goel, "Vertebral endplate morphology follows bone remodeling principles," *Spine*, vol. 32, pp. E667-73, 2007.
- [26] H. V. Crock and H. Yoshizawa, "The blood supply of the lumbar vertebral column," *Clin Orthop Relat Res*, pp. 6-21, 1976.

- [27] H. A. Horner and J. P. Urban, "2001 Volvo Award Winner in Basic Science Studies: Effect of nutrient supply on the viability of cells from the nucleus pulposus of the intervertebral disc," *Spine*, vol. 26, pp. 2543-9, 2001.
- [28] H. V. Crock, M. Goldwasser, and H. Yoshizawa, "Vascular anatomy related to the intervertebral disc," in *The Biology of the intervertebral disc*, vol. 2, P. Ghosh, Ed. Boca Raton, FL: CRC Press, 1988, pp. 109-133.
- [29] J. F. Ratcliffe, "Arterial changes in the human vertebral body associated with aging. The ratios of peripheral to central arteries and arterial coiling," *Spine (Phila Pa 1976)*, vol. 11, pp. 235-40, 1986.
- [30] J. P. Urban, S. Holm, and A. Maroudas, "Diffusion of small solutes into the intervertebral disc: as in vivo study," *Biorheology*, vol. 15, pp. 203-21, 1978.
- [31] M. D. Martin, C. M. Boxell, and D. G. Malone, "Pathophysiology of lumbar disc degeneration: a review of the literature," *Neurosurg Focus*, vol. 13, pp. E1, 2002.
- [32] D. Eyre, B. Caterson, and P. Benya, "The intervertebral disc," in *New Perspectives on Low Back Pain.*, S. Gordon and J. Frymoyer, Eds. Philadelphia, PA: American Institute of Orthopaedic Surgeons, 1991, pp. 147-209.
- [33] S. Roberts, J. P. Urban, H. Evans, and S. M. Eisenstein, "Transport properties of the human cartilage endplate in relation to its composition and calcification," *Spine*, vol. 21, pp. 415-20, 1996.
- [34] A. Maroudas, "Transport of solutes through cartilage: permeability to large molecules," *J Anat*, vol. 122, pp. 335-47, 1976.

- [35] H. J. Wilke, P. Neef, M. Caimi, T. Hoogland, and L. E. Claes, "New in vivo measurements of pressures in the intervertebral disc in daily life," *Spine*, vol. 24, pp. 755-62, 1999.
- [36] D. C. Ayotte, K. Ito, and S. Tepic, "Direction-dependent resistance to flow in the endplate of the intervertebral disc: an ex vivo study," *J Orthop Res*, vol. 19, pp. 1073-7, 2001.
- [37] S. Roberts, H. Evans, J. Trivedi, and J. Menage, "Histology and pathology of the human intervertebral disc," *J Bone Joint Surg Am*, vol. 88 Suppl 2, pp. 10-4, 2006.
- [38] S. Bernick and R. Cailliet, "Vertebral end-plate changes with aging of human vertebrae," *Spine*, vol. 7, pp. 97-102, 1982.
- [39] A. Maroudas, R. A. Stockwell, A. Nachemson, and J. Urban, "Factors involved in the nutrition of the human lumbar intervertebral disc: cellularity and diffusion of glucose in vitro," *J Anat*, vol. 120, pp. 113-30, 1975.
- [40] J. W. Kimball, "Blood," vol. 2010, 2010.
- [41] S. Roberts, J. Menage, and S. M. Eisenstein, "The cartilage end-plate and intervertebral disc in scoliosis: calcification and other sequelae," *J Orthop Res*, vol. 11, pp. 747-57, 1993.
- [42] H. Ishihara, K. Warensjo, S. Roberts, and J. P. Urban, "Proteoglycan synthesis in the intervertebral disk nucleus: the role of extracellular osmolality," *Am J Physiol*, vol. 272, pp. C1499-506, 1997.

- [43] D. Hukins, "Properties of spinal materials," in *The Lumbar Spine and Back Pain*, MIVJayson, Ed., 3rd Ed ed. Edinburgh: Churchill Livingstone, 1987, pp. 138-160.
- [44] N. Ventura, R. Huguet, A. Salvador, L. Terricabras, and A. M. Cabrera, "Intervertebral disc calcification in childhood," *Int Orthop*, vol. 19, pp. 291-4, 1995.
- [45] L. M. Benneker, P. F. Heini, S. E. Anderson, M. Alini, and K. Ito, "Correlation of radiographic and MRI parameters to morphological and biochemical assessment of intervertebral disc degeneration," *Eur Spine J*, vol. 14, pp. 27-35, 2005.
- [46] L. M. Benneker, P. F. Heini, M. Alini, S. E. Anderson, and K. Ito, "2004 Young Investigator Award Winner: vertebral endplate marrow contact channel occlusions and intervertebral disc degeneration," *Spine*, vol. 30, pp. 167-73, 2005.
- [47] J. Y. Margulies, A. Payzer, M. Nyska, M. G. Neuwirth, Y. Floman, and G. C. Robin, "The relationship between degenerative changes and osteoporosis in the lumbar spine," *Clin Orthop Relat Res*, pp. 145-52, 1996.
- [48] A. Harada, H. Okuizumi, N. Miyagi, and E. Genda, "Correlation between bone mineral density and intervertebral disc degeneration," *Spine (Phila Pa 1976)*, vol. 23, pp. 857-61; discussion 862, 1998.
- [49] L. D. Hordon, M. Raisi, J. E. Aaron, S. K. Paxton, M. Beneton, and J. A. Kanis, "Trabecular architecture in women and men of similar bone mass with and without vertebral fracture: I. Two-dimensional histology," *Bone*, vol. 27, pp. 271-6, 2000.

- [50] S. R. Pye, D. M. Reid, J. E. Adams, A. J. Silman, and T. W. O'Neill, "Radiographic features of lumbar disc degeneration and bone mineral density in men and women," *Ann Rheum Dis*, vol. 65, pp. 234-8, 2006.
- [51] E. K. Simpson, I. H. Parkinson, B. Manthey, and N. L. Fazzalari, "Intervertebral disc disorganization is related to trabecular bone architecture in the lumbar spine," *J Bone Miner Res*, vol. 16, pp. 681-7, 2001.
- [52] Z. Yang, J. F. Griffith, P. C. Leung, and R. Lee, "Effect of osteoporosis on morphology and mobility of the lumbar spine," *Spine*, vol. 34, pp. E115-21, 2009.
- [53] K. Singh, K. Masuda, E. J. Thonar, H. S. An, and G. Cs-Szabo, "Age-related changes in the extracellular matrix of nucleus pulposus and anulus fibrosus of human intervertebral disc," *Spine (Phila Pa 1976)*, vol. 34, pp. 10-6, 2009.
- [54] J. P. Urban and S. Roberts, "Degeneration of the intervertebral disc," *Arthritis Res Ther*, vol. 5, pp. 120-30, 2003.
- [55] C. W. Pfirrmann, A. Metzdorf, M. Zanetti, J. Hodler, and N. Boos, "Magnetic resonance classification of lumbar intervertebral disc degeneration," *Spine*, vol. 26, pp. 1873-8, 2001.
- [56] E. A. Nauman, K. E. Fong, and T. M. Keaveny, "Dependence of intertrabecular permeability on flow direction and anatomic site," *Ann Biomed Eng*, vol. 27, pp. 517-24, 1999.
- [57] L. A. Setton, W. Zhu, M. Weidenbaum, A. Ratcliffe, and V. C. Mow, "Compressive properties of the cartilaginous end-plate of the baboon lumbar spine," *J Orthop Res*, vol. 11, pp. 228-39, 1993.

- [58] F. Accadbled, D. Ambard, J. S. de Gauzy, and P. Swider, "A measurement technique to evaluate the macroscopic permeability of the vertebral end-plate," *Med Eng Phys*, vol. 30, pp. 116-22, 2008.
- [59] D. S. Perie, J. J. Maclean, J. P. Owen, and J. C. Iatridis, "Correlating material properties with tissue composition in enzymatically digested bovine annulus fibrosus and nucleus pulposus tissue," *Ann Biomed Eng*, vol. 34, pp. 769-77, 2006.
- [60] A. Nazarian, B. D. Snyder, D. Zurakowski, and R. Muller, "Quantitative micro-computed tomography: a non-invasive method to assess equivalent bone mineral density," *Bone*, vol. 43, pp. 302-11, 2008.
- [61] A. A. Postnov, A. V. Vinogradov, D. Van Dyck, S. V. Saveliev, and N. M. De Clerck, "Quantitative analysis of bone mineral content by x-ray microtomography," *Physiol Meas*, vol. 24, pp. 165-78, 2003.
- [62] G. J. Kazakia, A. J. Burghardt, S. Cheung, and S. Majumdar, "Assessment of bone tissue mineralization by conventional x-ray microcomputed tomography: comparison with synchrotron radiation microcomputed tomography and ash measurements," *Med Phys*, vol. 35, pp. 3170-9, 2008.
- [63] J. S. Thomsen, A. Laib, B. Koller, S. Prohaska, L. Mosekilde, and W. Gowin, "Stereological measures of trabecular bone structure: comparison of 3D micro computed tomography with 2D histological sections in human proximal tibial bone biopsies," *J Microsc*, vol. 218, pp. 171-9, 2005.

- [64] A. J. Burghardt, G. J. Kazakia, and S. Majumdar, "A local adaptive threshold strategy for high resolution peripheral quantitative computed tomography of trabecular bone," *Ann Biomed Eng*, vol. 35, pp. 1678-86, 2007.
- [65] J. A. MacNeil and S. K. Boyd, "Accuracy of high-resolution peripheral quantitative computed tomography for measurement of bone quality," *Med Eng Phys*, vol. 29, pp. 1096-105, 2007.
- [66] B. Borah, T. Dufresne, J. Nurre, R. Phipps, P. Chmielewski, L. Wagner, M. Lundy, M. Bouxsein, R. Zebaze, and E. Seeman, "Risedronate reduces intracortical porosity in women with osteoporosis," *J Bone Miner Res*, vol. 25, pp. 41-7, 2009.
- [67] E. Martin-Badosa, D. Amblard, S. Nuzzo, A. Elmoutaouakkil, L. Vico, and F. Peyrin, "Excised bone structures in mice: imaging at three-dimensional synchrotron radiation micro CT," *Radiology*, vol. 229, pp. 921-8, 2003.
- [68] A. Maroudas, "Biophysical chemistry of cartilaginous tissues with special reference to solute and fluid transport," *Biorheology*, vol. 12, pp. 233-48, 1975.
- [69] S. Cowin, *Bone mechanics handbook*, 2nd Ed ed: CRC Press, 2001.
- [70] A. A. Al-Munajjed, M. Hien, R. Kujat, J. P. Gleeson, and J. Hammer, "Influence of pore size on tensile strength, permeability and porosity of hyaluronan-collagen scaffolds," *J Mater Sci Mater Med*, vol. 19, pp. 2859-64, 2008.
- [71] C. Ayan, N. Colley, G. Cowan, E. Ezekwe, M. Wannell, P. Goode, F. Halford, J. Joseph, A. Mongini, G. Obondoko, and J. Pop, "Measuring Permeability Anisotropy - the Latest Approach," *Oilfield Review*, vol. 6, pp. 24-35, 1994.

- [72] F. J. O'Brien, B. A. Harley, M. A. Waller, I. V. Yannas, L. J. Gibson, and P. J. Prendergast, "The effect of pore size on permeability and cell attachment in collagen scaffolds for tissue engineering," *Technol Health Care*, vol. 15, pp. 3-17, 2007.
- [73] G. Ford, Chrysler, in *Measurement System Analysis Reference Manual* Detroit, Michigan: Automotive Industry Action Group, AIAG, 1995.
- [74] H. V. Crock, M. Goldwasser, and H. Yoshizawa, "Vascular anatomy related to the intervertebral disc.," in *Biology of the Intervertebral Disc*, P. Ghosh, Ed.: CRC Press, 1988, pp. 109–133.
- [75] N. Boos, A. Wallin, T. Schmucker, M. Aebi, and C. Boesch, "Quantitative MR imaging of lumbar intervertebral disc and vertebral bodies: methodology, reproducibility, and preliminary results," *Magn Reson Imaging*, vol. 12, pp. 577-87, 1994.
- [76] J. W. Stairmand, S. Holm, and J. P. Urban, "Factors influencing oxygen concentration gradients in the intervertebral disc. A theoretical analysis," *Spine*, vol. 16, pp. 444-9, 1991.
- [77] S. Holm, A. Maroudas, J. P. Urban, G. Selstam, and A. Nachemson, "Nutrition of the intervertebral disc: solute transport and metabolism," *Connect Tissue Res*, vol. 8, pp. 101-19, 1981.
- [78] K. Ogata and L. A. Whiteside, "1980 Volvo award winner in basic science. Nutritional pathways of the intervertebral disc. An experimental study using hydrogen washout technique," *Spine*, vol. 6, pp. 211-6, 1981.

- [79] S. R. Bibby, D. A. Jones, R. M. Ripley, and J. P. Urban, "Metabolism of the intervertebral disc: effects of low levels of oxygen, glucose, and pH on rates of energy metabolism of bovine nucleus pulposus cells," *Spine*, vol. 30, pp. 487-96, 2005.
- [80] S. R. Bibby, A. Meir, J. C. Fairbank, and J. P. Urban, "Cell viability and the physical environment in the scoliotic intervertebral disc," *Stud Health Technol Inform*, vol. 91, pp. 419-21, 2002.
- [81] D. M. Soukane, A. Shirazi-Adl, and J. P. Urban, "Computation of coupled diffusion of oxygen, glucose and lactic acid in an intervertebral disc," *J Biomech*, vol. 40, pp. 2645-54, 2007.
- [82] J. Antoniou, N. M. Goudsouzian, T. F. Heathfield, N. Winterbottom, T. Steffen, A. R. Poole, M. Aebi, and M. Alini, "The human lumbar endplate. Evidence of changes in biosynthesis and denaturation of the extracellular matrix with growth, maturation, aging, and degeneration," *Spine*, vol. 21, pp. 1153-61, 1996.
- [83] J. Duval, C. Dewey, R. Roberts, and D. Aron, "Spinal cord swelling as a myelographic indicator of prognosis: a retrospective study in dogs with intervertebral disc disease and loss of deep pain perception," *Vet Surg*, vol. 25, pp. 6-12, 1996.
- [84] W. Y. Gu, X. G. Mao, R. J. Foster, M. Weidenbaum, V. C. Mow, and B. A. Rawlins, "The anisotropic hydraulic permeability of human lumbar annulus fibrosus. Influence of age, degeneration, direction, and water content," *Spine*, vol. 24, pp. 2449-55, 1999.

- [85] P. E. Riches, N. Dhillon, J. Lotz, A. W. Woods, and D. S. McNally, "The internal mechanics of the intervertebral disc under cyclic loading," *J Biomech*, vol. 35, pp. 1263-71, 2002.
- [86] D. C. Ayotte, K. Ito, S. M. Perren, and S. Tepic, "Direction-dependent constriction flow in a poroelastic solid: the intervertebral disc valve," *J Biomech Eng*, vol. 122, pp. 587-93, 2000.
- [87] A. E. Rodríguez-Soto, A. G. Rodríguez, A. Burghardt, S. Majumdar, and J. C. Lotz, "Automatic Segmentation of the Vertebral Endplate VOI from Micro-CT Images," *Manuscript in progress*, 2010.
- [88] A. G. Rodriguez, D. S. Schultz, and J. C. Lotz, "Permeameter Device Validation " in *Manuscript in progress*, 2010.
- [89] N. Dhillon, E. C. Bass, and J. C. Lotz, "Effect of frozen storage on the creep behavior of human intervertebral discs," *Spine*, vol. 26, pp. 883-8, 2001.
- [90] F. Accadbled, J. M. Laffosse, D. Ambard, A. Gomez-Brouchet, J. S. de Gauzy, and P. Swider, "Influence of location, fluid flow direction, and tissue maturity on the macroscopic permeability of vertebral end plates," *Spine*, vol. 33, pp. 612-9, 2008.
- [91] L. A. Setton and J. Chen, "Cell mechanics and mechanobiology in the intervertebral disc," *Spine*, vol. 29, pp. 2710-23, 2004.
- [92] A. Nachemson, "The load on lumbar disks in different positions of the body," *Clin Orthop Relat Res*, vol. 45, pp. 107-22, 1966.

- [93] D. R. Wagner and J. C. Lotz, "Theoretical model and experimental results for the nonlinear elastic behavior of human annulus fibrosus," *J Orthop Res*, vol. 22, pp. 901-9, 2004.
- [94] S. R. Kim YJ, Doong JY, Grodzinsky AJ., "Fluorometric assay of DNA in cartilage explants using Hoechst 33258," *Anal Biochem*, vol. 174, pp. 168-76, 1988.
- [95] R. W. Farndale, D. J. Buttle, and A. J. Barrett, "Improved quantitation and discrimination of sulphated glycosaminoglycans by use of dimethylmethylene blue," *Biochim Biophys Acta*, vol. 883, pp. 173-7, 1986.
- [96] S. Roberts, I. W. McCall, J. Menage, M. J. Haddaway, and S. M. Eisenstein, "Does the thickness of the vertebral subchondral bone reflect the composition of the intervertebral disc?," *Eur Spine J*, vol. 6, pp. 385-9, 1997.
- [97] D. Resnick and G. Niwayama, *Degenerative disease of the spine*. Saunders, Philadelphia, 1981.
- [98] T. S. Keller, I. Ziv, E. Moeljanto, and D. M. Spengler, "Interdependence of lumbar disc and subdiscal bone properties: a report of the normal and degenerated spine," *J Spinal Disord*, vol. 6, pp. 106-13, 1993.
- [99] J. P. Urban and J. F. McMullin, "Swelling pressure of the lumbar intervertebral discs: influence of age, spinal level, composition, and degeneration," *Spine*, vol. 13, pp. 179-87, 1988.
- [100] J. P. Urban, "The role of the physicochemical environment in determining disc cell behaviour," *Biochem Soc Trans*, vol. 30, pp. 858-64, 2002.

- [101] T. Liebscher, K. Wuertz, M. Haefeli, A. Nerlich, and N. Boos, "Age-Associated changes in the cell number of the human lumbar intervertebral disc," in *Orthopaedic Research Society, In: Transactions of the 55th Annual Meeting of the Orthopaedic Research Society*. Las Vegas, NV. U.S.A. 2009, 2009.
- [102] D. Hastreiter, R. M. Ozuna, and M. Spector, "Regional variations in certain cellular characteristics in human lumbar intervertebral discs, including the presence of alpha-smooth muscle actin," *J Orthop Res*, vol. 19, pp. 597-604, 2001.
- [103] J. A. Jacobson, G. Girish, Y. Jiang, and B. J. Sabb, "Radiographic evaluation of arthritis: degenerative joint disease and variations," *Radiology*, vol. 248, pp. 737-47, 2008.
- [104] J. Aoki, I. Yamamoto, N. Kitamura, T. Sone, H. Itoh, K. Torizuka, and K. Takasu, "End plate of the discovertebral joint: degenerative change in the elderly adult," *Radiology*, vol. 164, pp. 411-4, 1987.
- [105] S. Holm and A. Nachemson, "Nutrition of the intervertebral disc: acute effects of cigarette smoking. An experimental animal study," *Ups J Med Sci*, vol. 93, pp. 91-9, 1988.
- [106] M. Iwahashi, H. Matsuzaki, Y. Tokuhashi, K. Wakabayashi, and Y. Uematsu, "Mechanism of intervertebral disc degeneration caused by nicotine in rabbits to explicate intervertebral disc disorders caused by smoking," *Spine (Phila Pa 1976)*, vol. 27, pp. 1396-401, 2002.

- [107] B. S. Jhavar, C. S. Fuchs, G. A. Colditz, and M. J. Stampfer, "Cardiovascular risk factors for physician-diagnosed lumbar disc herniation," *Spine J*, vol. 6, pp. 684-91, 2006.
- [108] H. Oda, H. Matsuzaki, Y. Tokuhashi, K. Wakabayashi, Y. Uematsu, and M. Iwahashi, "Degeneration of intervertebral discs due to smoking: experimental assessment in a rat-smoking model," *J Orthop Sci*, vol. 9, pp. 135-41, 2004.
- [109] S. Rajasekaran, J. N. Babu, R. Arun, B. R. Armstrong, A. P. Shetty, and S. Murugan, "ISSLS prize winner: A study of diffusion in human lumbar discs: a serial magnetic resonance imaging study documenting the influence of the endplate on diffusion in normal and degenerate discs," *Spine*, vol. 29, pp. 2654-67, 2004.
- [110] M. M. Katz, A. R. Hargens, and S. R. Garfin, "Intervertebral disc nutrition. Diffusion versus convection," *Clin Orthop Relat Res*, pp. 243-5, 1986.
- [111] F. M. H. Villars and G. B. Benedek, "Diffusion and transport processes," in *Physics with illustrative examples from medicine and biology*. Reading, Mass: Addison-Wesley, 1974.
- [112] K. Takeno, S. Kobayashi, K. Negoro, K. Uchida, T. Miyazaki, T. Yayama, S. Shimada, and H. Baba, "Physical limitations to tissue engineering of intervertebral disc cells: effect of extracellular osmotic change on glycosaminoglycan production and cell metabolism. Laboratory investigation," *J Neurosurg Spine*, vol. 7, pp. 637-44, 2007.

- [113] H. Ishihara and J. P. Urban, "Effects of low oxygen concentrations and metabolic inhibitors on proteoglycan and protein synthesis rates in the intervertebral disc," *J Orthop Res*, vol. 17, pp. 829-35, 1999.
- [114] T. Grunhagen, G. Wilde, D. M. Soukane, S. A. Shirazi-Adl, and J. P. Urban, "Nutrient supply and intervertebral disc metabolism," *J Bone Joint Surg Am*, vol. 88 Suppl 2, pp. 30-5, 2006.
- [115] K. Masuda, "Biological repair of the degenerated intervertebral disc by the injection of growth factors," *Eur Spine J*, vol. 17 Suppl 4, pp. 441-51, 2008.
- [116] R. Kandel, S. Roberts, and J. P. Urban, "Tissue engineering and the intervertebral disc: the challenges," *Eur Spine J*, vol. 17 Suppl 4, pp. 480-91, 2008.
- [117] S. Sobajima, G. Vadala, A. Shimer, J. S. Kim, L. G. Gilbertson, and J. D. Kang, "Feasibility of a stem cell therapy for intervertebral disc degeneration," *Spine J*, vol. 8, pp. 888-96, 2008.
- [118] H. J. Meisel, V. Siodla, T. Ganey, Y. Minkus, W. C. Hutton, and O. J. Alasevic, "Clinical experience in cell-based therapeutics: disc chondrocyte transplantation A treatment for degenerated or damaged intervertebral disc," *Biomol Eng*, vol. 24, pp. 5-21, 2007.
- [119] C. Hohaus, T. M. Ganey, Y. Minkus, and H. J. Meisel, "Cell transplantation in lumbar spine disc degeneration disease," *Eur Spine J*, vol. 17 Suppl 4, pp. 492-503, 2008.
- [120] W. E. Johnson and S. Roberts, "'Rumours of my death may have been greatly exaggerated': a brief review of cell death in human intervertebral disc disease and

- implications for cell transplantation therapy," *Biochem Soc Trans*, vol. 35, pp. 680-2, 2007.
- [121] W. T. Edwards, Y. Zheng, L. A. Ferrara, and H. A. Yuan, "Structural features and thickness of the vertebral cortex in the thoracolumbar spine," *Spine*, vol. 26, pp. 218-25, 2001.
- [122] X. Banse, J. P. Devogelaer, E. Munting, C. Delloye, O. Cornu, and M. Grynepas, "Inhomogeneity of human vertebral cancellous bone: systematic density and structure patterns inside the vertebral body," *Bone*, vol. 28, pp. 563-71, 2001.
- [123] A. K. Simpson, D. Biswas, J. W. Emerson, B. D. Lawrence, and J. N. Grauer, "Quantifying the effects of age, gender, degeneration, and adjacent level degeneration on cervical spine range of motion using multivariate analyses," *Spine*, vol. 33, pp. 183-6, 2008.
- [124] H. Gong, M. Zhang, L. Qin, K. K. Lee, X. Guo, and S. Q. Shi, "Regional variations in microstructural properties of vertebral trabeculae with structural groups," *Spine (Phila Pa 1976)*, vol. 31, pp. 24-32, 2006.
- [125] P. A. Hulme, S. K. Boyd, and S. J. Ferguson, "Regional variation in vertebral bone morphology and its contribution to vertebral fracture strength," *Bone*, vol. 41, pp. 946-57, 2007.
- [126] J. S. Thomsen, E. N. Ebbesen, and L. Mosekilde, "Zone-dependent changes in human vertebral trabecular bone: clinical implications," *Bone*, vol. 30, pp. 664-9, 2002.

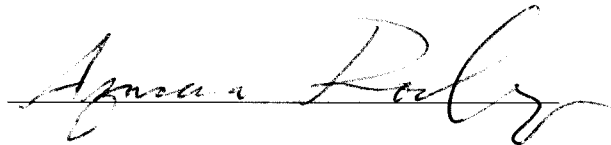
- [127] P. J. Roughley, M. Alini, and J. Antoniou, "The role of proteoglycans in aging, degeneration and repair of the intervertebral disc," *Biochem Soc Trans*, vol. 30, pp. 869-74, 2002.
- [128] C. L. Le Maitre, A. Pockert, D. J. Buttle, A. J. Freemont, and J. A. Hoyland, "Matrix synthesis and degradation in human intervertebral disc degeneration," *Biochem Soc Trans*, vol. 35, pp. 652-5, 2007.
- [129] T. Hildebrand and P. Ruegsegger, "A new method for the model-independent assessment of thickness in three-dimensional images," *Journal of Microscopy*, vol. 185, pp. 67-75, 1997.
- [130] P. L. Sylvestre, I. Villemure, and C. E. Aubin, "Finite element modeling of the growth plate in a detailed spine model," *Med Biol Eng Comput*, vol. 45, pp. 977-88, 2007.
- [131] S. M. Kokkonen, M. Kurunlahti, O. Tervonen, E. Ilkko, and H. Vanharanta, "Endplate degeneration observed on magnetic resonance imaging of the lumbar spine: correlation with pain provocation and disc changes observed on computed tomography diskography," *Spine*, vol. 27, pp. 2274-8, 2002.
- [132] H. Chen, S. Shoumura, S. Emura, and Y. Bunai, "Regional variations of vertebral trabecular bone microstructure with age and gender," *Osteoporos Int*, 2008.
- [133] J. P. Urban and C. P. Winlove, "Pathophysiology of the intervertebral disc and the challenges for MRI," *J Magn Reson Imaging*, vol. 25, pp. 419-32, 2007.
- [134] W. Limthongkul, E. E. Karaikovic, J. W. Savage, and A. Markovic, "Volumetric analysis of thoracic and lumbar vertebral bodies," *Spine J*, vol. 10, pp. 153-8.

- [135] A. S. Don and E. Carragee, "A brief overview of evidence-informed management of chronic low back pain with surgery," *Spine J*, vol. 8, pp. 258-65, 2008.


Publishing Agreement

It is the policy of the University to encourage the distribution of all theses and dissertations. Copies of all UCSF theses and dissertations will be routed to the library via the Graduate Division. The library will make all theses and dissertations accessible to the public and will preserve these to the best of their abilities, in perpetuity.

I hereby grant permission to the Graduate Division of the University of California, San Francisco to release copies of my thesis or dissertation to the Campus Library to provide access and preservation, in whole or in part, in perpetuity.



Author Signature



Date